

UNIVERSITY OF CALIFORNIA,
IRVINE

Search for the Diffuse Supernova Neutrino Background
at Super-Kamiokande

DISSERTATION

submitted in partial satisfaction of the requirements
for the degree of

DOCTOR OF PHILOSOPHY

in Physics

by

Kirk Ryan Bays

Dissertation Committee:
Professor Henry W. Sobel, Chair
Professor Jonas Schultz
Professor Guarang Yodh

2012

TABLE OF CONTENTS

	Page
LIST OF FIGURES	v
LIST OF TABLES	viii
ACKNOWLEDGMENTS	ix
CURRICULUM VITAE	x
ABSTRACT OF THE DISSERTATION	xiii
1 Introduction	1
1.1 Neutrinos	1
1.2 Supernovae	2
1.3 SN1987A	8
1.4 The DSNB	9
1.5 The First SK Study	12
1.6 Other searches for the DSNB	13
2 The Super-Kamiokande Detector	14
2.1 Introduction to the Detector	14
2.1.1 Detector Overview	14
2.1.2 Timeline of the Detector	16
2.1.3 Detector Details	17
2.2 Physics in the Detector	19
2.3 The Water System	23
2.4 Radon Free Air System	25
2.5 The DAQ	26
2.5.1 ID DAQ	26
2.5.2 OD DAQ	29
2.5.3 Triggers	30
3 Detector Calibration	32
3.1 LINAC	32
3.2 DT Generator	34
3.3 PMT Calibration	35

3.4	Water Transparency	38
3.4.1	Laser Measurements	38
3.4.2	Decay Electrons	39
4	Software Tools	43
4.1	Vertex Reconstruction	43
4.2	Energy Reconstruction	44
4.3	Direction Reconstruction	46
4.4	Muon Fitting	47
4.5	Multiple Coulomb Scattering Estimation	51
4.6	Cherenkov Angle Reconstruction	51
4.7	dE/dx reconstruction	52
4.8	Alternate Muon Fitting	54
5	Modeling	57
5.1	The Monte Carlo	57
5.2	Atmospheric Neutrino Backgrounds	58
5.3	DSNB Modeling	62
6	Analysis: Event Reduction	64
6.1	First Reduction	64
	OD triggered events	65
	Charge cut	65
	Fiducial volume	66
	50 μ s cut	67
	Calibration events	67
	Noise cut	67
6.2	2-peak cut	68
6.3	Incoming Event Cut	70
6.4	Solar Cut	72
6.5	Spallation Cut	76
	6.5.1 Spallation Likelihood Variables	77
	6.5.2 Method of Determining Spallation	80
	6.5.3 Multiple Muons	82
	6.5.4 Spallation Summary	84
6.6	Pion Cut	85
6.7	Multi Ring Cut	85
6.8	OD-Related Cut	86
6.9	‘Sub-event Cut’	87
6.10	Cherenkov Angle Distribution	88
6.11	Reduction Efficiency Summary	89

7	Analysis: Limit Extraction	92
7.1	Cherenkov Angle Regions	92
7.2	Extended Maximum Likelihood Fit	94
7.3	Inclusion of Systematic Errors	96
7.3.1	Energy Scale and Resolution Uncertainty	96
7.3.2	Atmospheric ν Background Systematic Errors	97
7.3.3	Energy Independent Efficiency Systematic Error	100
8	Results	102
8.1	Basic Results	102
8.2	Comparison to 2003 Result	106
9	Limit on SN Emission Spectrum	108
9.1	Making a General Relic Model	108
9.2	Method	109
10	Conclusion and Future	114
	Bibliography	116
	Appendices	120
A	Appendix A - Spallation	120
A.1	Spallation: SK-I/III Combined Likelihoods	122
A.2	SK-II likelihoods	131
A.3	Spallation: Algorithm	140
B	Appendix B - spectral PDFs	144
B.1	SRN PDFs	144
B.2	SK-I remaining background fits	151
B.3	SK-II remaining background fits	155
B.4	SK-III remaining background fits	159
C	Appendix C - NC	163
D	Appendix D - Expanded fit results	168

LIST OF FIGURES

	Page
1.1	Expected events from galactic SN 10
1.2	Examples of theoretical DSNB spectra 11
1.3	2003 final data sample 13
2.1	A schematic of the SK detector. 16
2.2	Schematic of the Hamamatsu R3600 PMT 18
2.3	Quantum efficiency of the Hamamatsu R3600 PMT 19
2.4	Event rate predictions for different SRN interaction modes 21
2.5	Interaction cross sections 22
2.6	Example event display 23
2.7	Schematic of the SK Water Purification System. 24
2.8	Schematic of the radon free air system. 25
2.9	Schematic of the SK ID DAQ. 28
2.10	Schematic of the SK OD DAQ. 29
3.1	LINAC information 34
3.2	Typical TQ map 37
3.3	Light intensity vs. distance distribution 40
3.4	SK-III water transparency 41
3.5	N_{eff} vs water transparency 42
4.1	Example distribution of 3-hit combinations 52
4.2	Example dE/dx distribution for a typical muon. 54
5.1	Spectra of the four remaining backgrounds. 62
6.1	Distribution of deposited charge 66
6.2	2-peak event 68
6.3	Max number of hits outside main timing peak 69
6.4	SK-I d_{eff} vs energy 71
6.5	d_{eff} of final sample 72
6.6	$\cos(\theta_{sun})$ distribution 73
6.7	SK-I solar cut background fit 75
6.8	Spallation half-life vs energy 77
6.9	Schematic showing spallation distance variables. 78
6.10	SK-I/III L_{TRANS} 81

6.11	SK-I/III L_{LONG}	81
6.12	Multiple ring event display	86
6.13	SN relic Cherenkov angle distribution	89
6.14	Signal efficiency now compared to 2003	90
7.1	Final data Cherenkov angle distribution showing backgrounds	94
7.2	Asymmetric Gaussian normalization	99
8.1	SK-I LMA fit	103
8.2	SK-II LMA fit	103
8.3	SK-III LMA fit	104
8.4	LMA fit likelihoods	105
9.1	Positron spectra in SK from MC	110
9.2	Limit contour event rate vs ν temperature	111
9.3	Limit contour luminosity vs ν temperature	112
A.1	Single muon SK-I/III spallation likelihoods	122
A.2	Stopping muon SK-I/III spallation likelihoods	123
A.3	Multiple muon (type 1) SK-I/III spallation likelihoods	124
A.4	Multiple muon (type 2) SK-I/III spallation likelihoods	125
A.5	Single muon SK-I/III random likelihoods	126
A.6	Stopping muon SK-I/III random likelihoods	127
A.7	Multiple muon (type 1) SK-I/III random likelihoods	128
A.8	Multiple muon (type 2) SK-I/III random likelihoods	129
A.9	Multiple track SK-I/III likelihoods	130
A.10	Single muon SK-II spallation likelihoods	131
A.11	Stopping muon SK-II spallation likelihoods	132
A.12	Multiple muon (type 1) SK-II spallation likelihoods	133
A.13	Multiple muon (type 2) SK-II spallation likelihoods	134
A.14	Single muon SK-II random likelihoods	135
A.15	Stopping muon SK-II random likelihoods	136
A.16	Multiple muon (type 1) SK-II random likelihoods	137
A.17	Multiple muon (type 2) SK-II random likelihoods	138
A.18	Multiple track SK-II likelihoods	139
B.19	SK-I SRN PDFs	145
B.20	SK-II SRN PDFs	146
B.21	SK-III SRN PDFs	147
B.22	SK-I SRN PDFs II	148
B.23	SK-II SRN PDFs II	149
B.24	SK-III SRN PDFs II	150
B.25	SK-I ν_μ CC fit	151
B.26	SK-I ν_e CC fit	152
B.27	SK-I NC elastic fit	153
B.28	SK-I μ/π CC fit	154
B.29	SK-II ν_μ CC fit	155

B.30 SK-II ν_e CC fit	156
B.31 SK-II NC elastic fit	157
B.32 SK-II μ/π CC fit	158
B.33 SK-III ν_μ CC fit	159
B.34 SK-III ν_e CC fit	160
B.35 SK-III NC elastic fit	161
B.36 SK-III μ/π fit	162
C.37 NC MC background 1	164
C.38 NC MC background 2	166
C.39 NC MC background 3	167

LIST OF TABLES

	Page
2.1 Trigger summary	31
4.1 Alternate muon fitter entry position thresholds	56
6.1 SK-I/III solar cut inefficiency summary	76
6.2 Spallation Cut Signal Efficiencies	84
6.3 Cut Signal Efficiency (Systematic Error) Summary	91
7.1 Total Efficiency Systematic Error	100
8.1 90% CL flux limit ($\bar{\nu}_e \text{ cm}^{-2} \text{ s}^{-1}$), $E_\nu > 17.3 \text{ MeV}$	102
9.1 Summary of limit values.	113
A.1 Spallation products	121
D.2 SK-I complete fit results	169
D.3 SK-II complete fit results	169
D.4 SK-III complete fit results	170

ACKNOWLEDGMENTS

I would like to thank Michael Smy for his kind and unfailing mentorship. He was always available, always helpful, and always had my best interests in mind. I learned more from him than anyone else in my academic career, and without him, I would have accomplished much less.

I would like to thank Hank Sobel for his friendly advisorship. He was always there when I needed him, always kind, and opened all the doors to allow me to participate in world class science and enter the scientific community.

I would like to thank Masayuki Nakahata for his friendly genius, overseeing my work in the low energy group, and always being willing to take some time out of his incredibly busy schedule to answer a question or examine my progress.

I would like to acknowledge the rest of the UCI group - Mark Vagins, Bill Kropp, Jeff Griskevich - for their friendliness and helpfulness. Thanks for making work a good place to be.

To my colleagues in the low energy group and Super-K: it's been a pleasure doing science with you.

Thanks to my thesis committee and professors, for their work at helping me be a better scientist.

And to my fellow graduate students who I've known for all or part of the last seven years - it was a good time; best of luck and hope to see you out there!

CURRICULUM VITAE

Kirk Ryan Bays

Research Interests:

Particle physics, especially neutrinos and cosmic rays. Participating in new experimental techniques and discoveries.

Education:

University of California, Irvine

Ph.D., Physics, 2012

- Thesis Topic: *Search for the Diffuse Supernova Neutrino Background at Super-Kamiokande*
- Adviser: Professor Henry W. Sobel
- Area of Study: Experimental Neutrino Physics

Oregon State University

B.S., Physics and Computational Physics, June 2004

- Minor in Mathematics

Publications:

K. Abe *et al.* (Super-Kamiokande Collaboration). Solar neutrino results in Super-Kamiokande-III. *Phys. Rev. D* **83**, 052010 (2011).
doi:10.1103/PhysRevD.83.052010

R. Wendell *et al.* (The Super-Kamiokande Collaboration). Atmospheric neutrino oscillation analysis with subleading effects in Super-Kamiokande I, II, and III. *Phys. Rev. D* **81**, 092004 (2010).
doi:10.1103/PhysRevD.81.092004

E. Thrane *et al.* (The Super-Kamiokande Collaboration). Search for astrophysical neutrino point sources at Super-Kamiokande. *ApJ* **704** 503 (2009).
doi:10.1088/0004-637X/704/1/503

E. Thrane *et al.* (The Super-Kamiokande Collaboration). Search for neutrinos from GRB 080319B at Super-Kamiokande. *ApJ* **697** 730 (2009).
doi:10.1088/0004-637X/697/1/730

M. Fechner *et al.* (The Super-Kamiokande Collaboration). Kinematic reconstruction of atmospheric neutrino events in a large water Cherenkov detector with proton identification. *Phys. Rev. D* **79** 112010 (2009).
doi:10.1103/PhysRevD.79.112010

H. Nishino *et al.* (The Super-Kamiokande Collaboration). Search for Proton Decay via $p \rightarrow e^+ \pi^0$ and $p \rightarrow \mu^+ \pi^0$ in a Large Water Cherenkov Detector. *Phys. Rev. Lett.* **102**, 141801 (2009).
doi:10.1103/PhysRevLett.102.141801

H. Watanabe *et al.* (The Super-Kamiokande Collaboration). First study of neutron tagging with a water Cherenkov detector. *Astroparticle Physics* **31** 4 (2009).
doi:10.1016/j.astropartphys.2009.03.002

Conference Proceedings:

K. Bays and T. Iida for the Super-Kamiokande Collaboration. Supernova Relic Neutrino Studies at Super-Kamiokande. ICRC 2009, Lodz, Poland (presentation)

K. Bays for the Super-Kamiokande collaboration. Search for Supernova Relic Neutrinos at Super-Kamiokande. Neutrino 2010, Athens, Greece (poster)

Teaching Experience:

University of California, Irvine

Teaching Assistant

September 2005 to August 2007

- TA for multiple classes. Helped develop TA curricula for other TA's. Private tutoring in physics tutoring center.

Oregon State University

Teaching Assistant

September 2002 to January 2004

- TA for multiple classes.

Special Student Assistant

2003 to 2004

- Special student assistant to a blind physics undergraduate. Acted as lab partner in electronics lab. Three classes total.

Professional Experience:

Super-Kamiokande

Graduate Student Researcher

2006-2011

- Responsible for water transparency calibration via decay electrons for low energy group (2006-2007)
- Participated in many on-site calibrations, using both a linear accelerator and a custom deuterium-tritium generator
- Carried out reactor neutrino feasibility study, including coding and creating custom MC (2007-2008)
- Processed and implemented ^{16}N cut for official SK-III solar analysis (2008-2009)
- Major improvements to supernova relic neutrino analysis (thesis work), including new techniques for determining cosmic ray spallation
- PRD paper submitted Nov. 2011, preprint: <http://arxiv.org/abs/1111.5031>

Indiana University Cyclotron Facility

Research Experience for Undergraduates

Summer 2002

- Worked on the final physics experiment at the IUCF
doi:10.1103/PhysRevLett.91.142302.
- Responsible for measuring the exact geometry of a lead glass detector array for entry into GEANT.

Hardware and Software Skills:

- Experience with water Cherenkov techniques, machine shop tools, a magnet steered linear accelerator, computers and electronics
- Familiarity with Fortran, C, PAW, Root, ZBS, UNIX, shell scripts, GNU make, Mathematica, GEANT, NQS, and more

ABSTRACT OF THE DISSERTATION

Search for the Diffuse Supernova Neutrino Background
at Super-Kamiokande

By

Kirk Ryan Bays

Doctor of Philosophy in Physics

University of California, Irvine, 2012

Professor Henry W. Sobel, Chair

A search for the SN relic neutrino signal (also known as the diffuse supernova neutrino background) was carried out at Super-Kamiokande (SK), using SK-I, II, and III data (176 kton-years total data, over 2853 live days). The search improved over the previous SK search by a multitude of improvements to the cuts, improving average efficiency from 52% to about 75%, further reducing backgrounds in the final sample, and lowering the analysis energy threshold from 18 MeV (total positron energy) to 16 MeV (except for SK-II). The spallation cut was especially improved, by means of a new longitudinal tracking technique, better tuning, and a better muon fitter that allows muon categorization. The study also utilizes a new unbinned likelihood fit, with two new remaining backgrounds considered, and many new systematic errors. These improvements make this study the most sensitive search for SN relic neutrinos to date. No signal was found, although a positive indication of a relic component in the SK-II and SK-III data set is interesting, if not significant. New limits were placed on many models, and a limit as a function of emitted neutrino spectrum is presented.

Chapter 1

Introduction

1.1 Neutrinos

In 1930, Pauli theorized a new particle in order to conserve momentum in beta decay reactions. Termed the neutrino, its existence wasn't experimentally verified until 1956 by Reines and Cowan (for which Reines received the Nobel prize in 1995). Originally believed to be massless, we know now that neutrinos indeed have mass, and that they come in three flavors, each associated with a lepton, and that the neutrino can undergo flavor change ('oscillation'), as the mass eigenstates differ from the flavor eigenstates.

In the standard model of physics, the neutrino is considered a fundamental particle. Since we know it has mass, it interacts gravitationally, but the mass is so small that this effect is negligible. As it is electromagnetically neutral, and does not interact via the strong force, this leaves the weak nuclear force as the only real means the neutrino has of interacting with the rest of reality. Because of this, it is virtually ghostlike, traveling through large quantities of matter as if it didn't exist, and is very difficult to study experimentally, typically requiring very large detectors and sophisticated detection techniques.

Neutrinos are generated by nuclear reactions, such as fusion in the sun, fission in the Earth's crust and mantle, and man made nuclear reactors. Neutrinos are created when cosmic rays interact with nuclei in the Earth's atmosphere, creating showers of often unstable particles, whose decays produce neutrinos (termed atmospheric neutrinos). Man made neutrino beams now exist. A large amount of neutrinos remain from the big bang as well, termed big bang relic neutrinos, not to be confused with supernova relic neutrinos. Many experiments exist that attempt to study neutrinos from the various sources.

One use of neutrinos still in its infancy is the field of neutrino astronomy. Many astrophysical phenomena should produce copious amounts of neutrinos, which can be useful and distinct from studies of extraterrestrial objects through electromagnetic radiation. Not only do neutrinos sometimes carry information not contained in electromagnetic radiation, but neutrinos are not blocked, scattered, or otherwise affected by matter that may be encountered on the trip to Earth.

As of the time of this writing, the only extraterrestrial neutrinos definitively seen on Earth are from the sun and from supernova SN1987A. As our understanding of the properties of the neutrino advance along with the sophistication of our neutrino detectors, it is expected that more sources will be detected, allowing us to learn new and important things about the universe around us.

This thesis is the result of a search for a never before seen extraterrestrial neutrino signal.

1.2 Supernovae

The universe is full of stars, and they live interesting and varied lives. Stars heavier than about eight solar masses tend to end their lives in an incredible explosion of energy we call a core collapse supernova, where for a brief time the star releases so

much electromagnetic radiation, it often outshines the entire rest of the galaxy it lives in. Although there are other types of supernovae, core collapse supernovae are what we are most interested in for the purpose of this thesis, and I will now attempt to summarize our current understanding of them.

When a collection of matter in space (a nebula, for instance) becomes sufficiently dense, it gathers all the matter in a region tightly in on itself, forming a star. This matter is all pulled towards the center of mass of the system. The temperature of the matter increases with the density; once the temperature becomes high enough, fusion commences, and a star is born.

Most stars begin life comprised of mostly hydrogen, and spend the majority of their life fusing that hydrogen into helium. The heat produced by this reaction radiates out, creating an outwards pressure that counters the gravitational forces seeking to pull the star towards its own center. The size of the star is determined by the equilibrium of these forces.

When a star runs out of hydrogen to burn in its core, there is not a sufficient force left to counter gravity, and the star collapses upon itself. If the star's mass is small (like our sun), electron degeneracy pressure will slow the collapse of the core, but the contracting outer layers of the star will heat up and begin fusing remaining hydrogen. Since the outer layer is less confined than the core, the star will expand in size and become a red giant, and then eventually a white dwarf.

For stars with greater than about eight solar masses, however, the electron degeneracy pressure is not sufficient to slow the collapse of the star completely, and the core's density continues to increase. Just as with the star's original birth, the temperature increases with density and pressure, until it is hot enough for helium fusion to occur. As some hydrogen still exists in the outer portions of the star, hydrogen to helium fusion can still take place there, but in the core helium to carbon fusion dominates, and the star becomes layered. When the core's helium is exhausted, the

star collapses again, until the core temperature and pressure becomes high enough for the next most massive nuclei to fuse; again, a helium burning layer still exists, as does a hydrogen burning layer.

As the core moves on to increasingly dense elements to burn, the star becomes layered like an onion. Each phase of burning takes successively less time to finish, and the star quickly cycles towards its inevitable demise. Silicon burning in the core signals the final stage before complete collapse; once silicon starts to fuse into nickel-56, the star's life is measured in days [1].

Once the silicon in the core is exhausted, the star begins to collapse again, but this time no further fusion processes exist to stop it. Some of the nickel in the core will decay to iron, and the core at this stage will be a combination of nickel and iron. For stars that begin with more than around eight solar masses, the remaining core at this point will be heavier than the Chandrasekhar limit, and electron degeneracy pressure will be overcome. In this case, the matter in the star accelerates towards the center, achieving velocities of up to $.2 c$, and the density increases rapidly, causing the temperature to climb as well.

The high temperature in the core makes electron capture processes favorable, and electrons and protons are quickly converted into neutrinos and neutrons. As electrons disappear, the electron degeneracy pressure becomes smaller, which causes the collapse to occur more quickly, causing higher temperatures, which makes the electron capture processes occur even more quickly. This positive feedback effect increases the rate of supernova collapse, and also turns many of the electrons into electron neutrinos, and many of the protons into neutrons, such that the mass becomes comprised mostly of neutrons. Many heavy elements remain however, especially in the outer layers of the star, and it is believed that most of the heavy elements in the universe are created in core collapse supernovae, and spread into the universe by the resulting explosion, where they can collect and mix with other matter, and eventually

form galaxies and solar systems like ours. The quick transformation of most of the protons to neutrons is called a neutronization burst (or deleptonization burst). The neutrinos created in this burst are inside the core, which is reaching densities large enough to slow or even trap the neutrinos from escaping; generally the neutronization burst neutrinos escape the star in a ~ 10 ms window.

At some point in the collapse, the density in the core will reach a point where neutrinos are largely trapped; the boundary of the mass from which neutrinos cannot easily escape is called the neutrinosphere. Neutrinos created in the core will diffuse outwards and finally escape from the surface of the neutrinosphere; inside it is so dense that neutrino-neutrino interactions become very important and cannot be neglected.

The collapse continues until nuclear densities are achieved, where neutron degeneracy pressure and neutron-neutron interactions form the final barrier to continued collapse. For stars starting with less than about 20 solar masses this barrier will not be overcome, and the rapidly collapsing matter hits it like the proverbial brick wall. So abruptly is it reached, in fact, that the collapsing matter rebounds, and what was a collapse becomes an explosion, as the energy of the collapse is transformed into an expanding shock wave.

The expanding super-sonic shock wave will interact with the still infalling matter, where it can break heavy nuclei into radioactive elements, which decay and emit light. It can also free protons, which are quickly neutronized via electron capture, producing neutrinos.

As the supersonic shock wave expands, the super-heated neutron core (around 100 billion K) releases neutrinos in pairs of neutrinos and anti-neutrinos of all flavors. This neutrino ‘thermal burst’ releases almost a hundred times as many neutrinos as were created by the neutronization burst. This thermal burst releases $\sim 10^{46}$ J of energy, and cools the core to more stable levels. The thermal neutrinos diffuse out of the neutrinosphere as the core expands; it takes ~ 10 seconds for all of the

thermal neutrinos to escape. Thus, the energy of a supernova comes originally from gravitational potential; is converted to heat; then finally released mostly as neutrinos ($\sim 99\%$), kinetic energy of the accelerated particles ($\sim 1\%$) and light ($\sim 0.1\%$). As the neutronization burst neutrinos are created earlier and not trapped, and the thermal neutrinos are created later and are trapped in the expanding neutrinosphere, the two should be separated in time when reaching Earth.

Those who model supernovae often find that the rebound shock is not sufficient to explain the full supernova explosion, and that on its own, the shock wave would likely stall, losing all its energy to interactions with infalling matter. It is generally supposed that the thermal neutrinos provide the rest of the energy necessary to explain the explosion; calculations indicate that if the thermal neutrinos can transfer as much as 1% of their energy to the infalling matter, the explosion can be well explained [2]. There is still some confusion as to how exactly this energy transfer occurs, however.

Neutrinos and anti-neutrinos of all flavors are created in roughly equal proportions during the thermal burst, though there are slightly more electron type neutrinos created overall if we include those from the neutronization burst. However, the neutrinos do not all interact in the same way. As time passes, neutrinos are created in the thermal burst, and the shock wave causes the star to expand, all of which rapidly causes cooling. The tau and muon flavor neutrinos will only interact with the matter via neutral current interactions, as they are not energetic enough to create muons or taus via charged current interactions, and thus find themselves the least restricted. They are able to escape the neutrinosphere most easily, and can escape from deeper in the core, where the temperature is still much hotter than the surface. On the other hand, electron neutrinos can interact on neutrons, and electron anti-neutrinos on protons in charge current reactions. Since there are more neutrons than protons in the core, electron neutrinos will be most restricted, can only escape from the most

shallow depths, and will thus on average be cooler. In general, $\langle E_{\nu_e} \rangle < \langle E_{\bar{\nu}_e} \rangle < \langle E_{\nu_\mu, \bar{\nu}_\mu} \rangle \approx \langle E_{\nu_\tau, \bar{\nu}_\tau} \rangle$.

Neutrinos stuck inside of or passing through the dense matter in the neutrinosphere will undergo oscillation via the MSW effect [3]. This can have a variety of important effects on the spectrum shape of the emitted neutrinos and must be taken into account for proper modeling. Oscillation and neutrino-neutrino interaction effects also may help explain how the neutrino burst transfers energy to the infalling matter.

After the explosion, which blows off most of the light elements and outer layers of the star and leaves only the dense neutron core, stars beginning with mass less than around 20 solar masses are left as neutron stars. For stars beginning with between about 20 to 50 solar masses, it is believed that the star's core collapse will produce a supernova explosion, but not all the mass will escape, and a black hole will be produced. For stars above around 50 solar masses, it is thought that the collapse will lead directly to black hole formation, with no supernova explosion.

Supernovae are classified by their spectral properties. If the supernova spectrum contains a hydrogen line (Balmer series) is it classified as Type II; if not, it is Type I. These are further subdivided. However, most classifications are simply different types of core collapse supernovae. An exception is Type Ia supernovae, which generally occurs when a white dwarf in a binary star system accretes matter until it reaches the Chandrasekhar limit of around 1.38 solar masses. There are some theories that the explosion occurs due to carbon fusion before a collapse is initiated; regardless of the cause, Type Ia supernovae are unique in that they all share an almost identical light profile, as they all come from the same physical process finally reaching the same threshold. This feature of a shared light profile - that is both readily identifiable and nearly identical to all Type Ia supernovae - makes Type Ia's particularly useful to the astronomical community as a so called 'standard candle', allowing nearby objects to

be calibrated in comparison.

Thus in general, all supernovae can be classified as either Type Ia, or core collapse; a main difference being the light profile, which is less transparent for the more compact Type Ia supernovae. For Type Ia's, most of the light ultimately comes from the decay of radionuclides, especially Ni-56 and Co-56, as opposed to the light from a core collapse supernova, which produces most of its light from energy originating from the collapse shock wave. Type Ia supernovae are less common, produce less neutrinos, and are generally not considered in the scope of this thesis.

1.3 SN1987A

On February 23, 1987, the light from a core collapse supernova in the Large Magellanic Cloud, a nearby galaxy that is considered a satellite galaxy to our own, was seen on Earth. The supernova is thought to have occurred approximately 51.4 kiloparsecs away [4], and is the first nearby supernova seen by modern astronomy apparatus.

A small burst of neutrinos was detected approximately 3 hours prior to the arrival of the first light by three terrestrial detectors. The first two detectors, IMB and KamiokaNDE (the predecessor to the current Super-Kamiokande), were water Cherenkov detectors designed to study proton decay. KamiokaNDE detected 11 neutrino events, and IMB 8 neutrino events, coincident within seconds [5, 6]. Baksan, a neutrino observatory in Russia, saw 5 events. These events were highly significant compared to background, and constituted the first ever certain detection of neutrinos from farther away than our sun.

The 1987A supernova neutrino burst verified the fundamental model of core collapse, and generated a tremendous amount of interest and excitement in the scientific community. Literally thousands of scientific papers have been written about the 24 neutrinos events detected, studying them in every manner imaginable. It can

be argued that the scientific excitement of this event begat what we now know of as modern neutrino astronomy.

1.4 The DSNB

With supernovae releasing on the order of 10^{46} J of energy, 99% as neutrinos, the neutrino flux from each supernova event is enormous. In a galaxy such as the Milky Way, it is estimated a supernova will occur around 2 or 3 times a century [7]. Current terrestrial neutrino detectors are patiently waiting for another galactic supernova, which would give us invaluable scientific data, and next generation detectors are being built with the hopes that a galactic supernova will occur soon. SK is currently the world's premiere detector for SN neutrino burst detection, and would see on the order of thousands of events (see Fig. 1.1), allowing a precision measurement of the spectrum shape.

However, the wait could be decades, and there is an alternative to patience. Although we would not see a significant neutrino burst from a supernova farther away than our galaxy and its satellites, all of the supernovae that have exploded throughout the history of the universe have released neutrinos, most of which have never interacted and are still in existence. In fact, it is theorized that a background of supernova neutrinos exists everywhere, from supernovae throughout all of time. This signal is called the Diffuse Supernova Neutrino Background (DSNB), or also frequently referred to as the Supernova Relic Neutrino background. Although still often called 'relics', this terminology is disfavored due to confusion with big bang relic neutrinos. For convenience, I may refer to them as relics or SN relics during the course of this thesis, however.

Many cosmologists have considered the DSNB signal, constructing models that predict both the flux and the spectrum. The first models were crafted even before

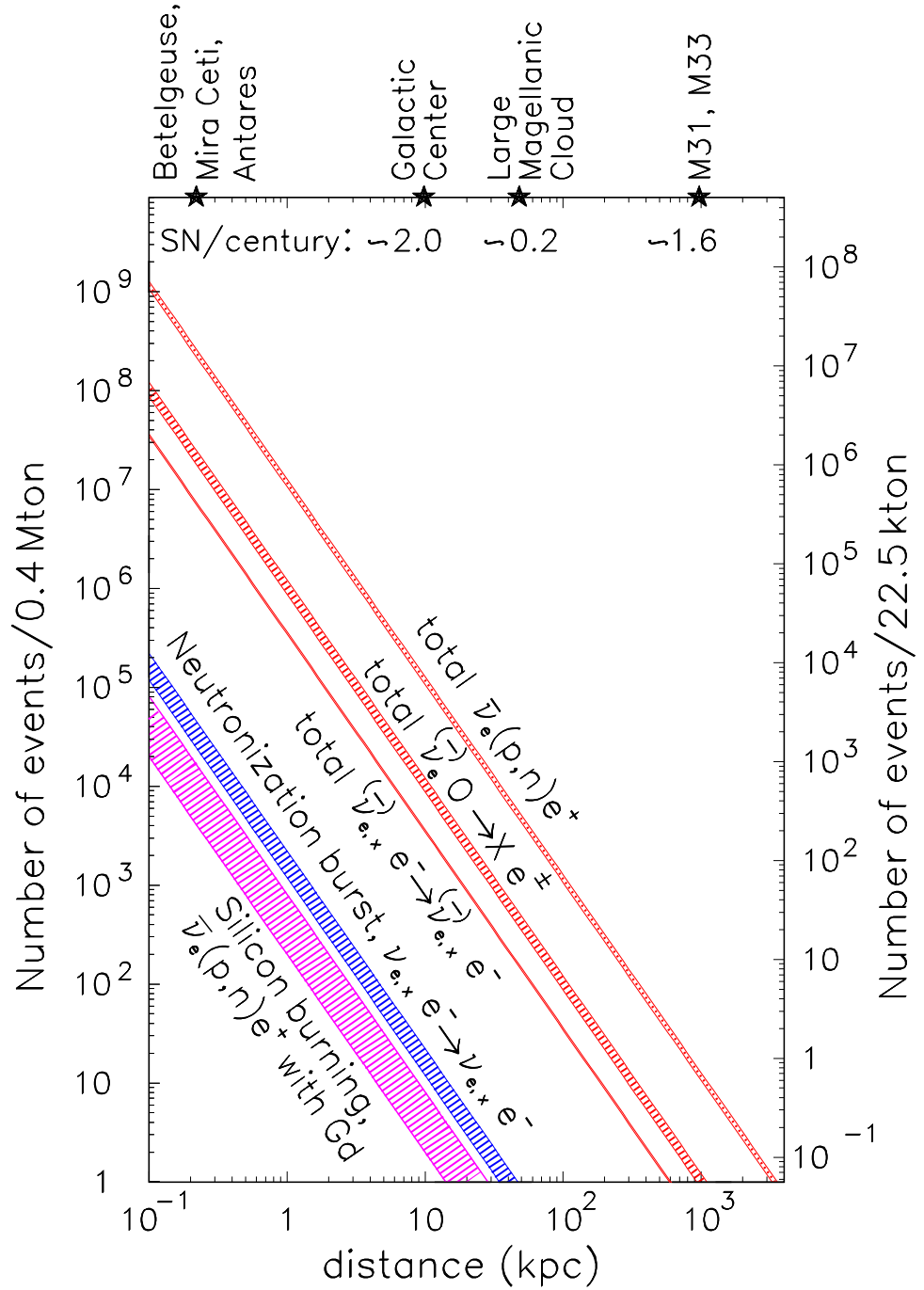


Figure 1.1: Expected number of events in SK (right axis) as a function of supernova distance, for different interaction modes, from [8].

SN1987A [9, 10, 11], then after SN1987A with increasing interest and sophistication [12, 13, 14, 15, 16, 17, 18]. Some examples of theoretical spectra are shown in Fig. 1.2.

The models shown are those considered in our analysis: Malaney’s cosmic gas infall

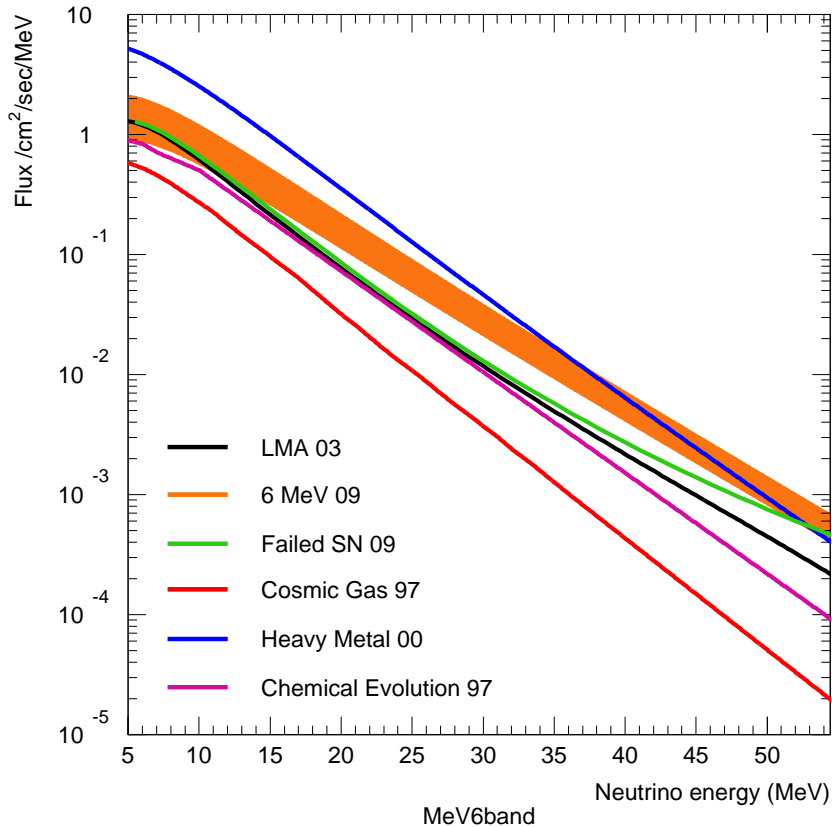


Figure 1.2: Examples of theoretical DSNB spectra. The 6 MeV (from [19]) is shown as a band, as the authors estimated exact total errors on their calculation. The year of each model’s publication is also listed.

model [14]; Woosley and Hartmann’s chemical evolution model [13]; Kaplinghat *et al.*’s heavy metal abundance model [16]; Ando *et al.*’s LMA model [17]¹; Lunardini’s failed supernova model [15]²; and the variable neutrino temperature formulation of Horiuchi *et al.* (6 MeV considered) [19]. Although the normalizations vary, the general shape and slope of the predicted spectra are relatively constant, which simplifies the experimental analysis.

The DSNB has never been seen. The current world limit on DSNB flux is from

¹The flux of the LMA model is increased by a factor of 2.56 from the paper, a revision introduced at NNN05

²Assumed parameters are: Failed SN rate = 22%, EoS = Lattimer-Swesty, and survival probability = 68%

a previous SK analysis (see next section). Even without accurate measurements of the spectra, placing limits on the flux (or seeing a signal) helps modelers constrain theories, and can reveal important information about related quantities, such as supernova rates of stars, or star formation rates in galaxies, which go into the DSNB models. As scientific models of supernovae themselves have advanced, cosmologists have been able to more accurately understand the details of the neutrino oscillations that occur inside a supernova, which should lead to more accurate DSNB predictions.

Recent models predict a DSNB flux that is on the cusp of discovery [18]. They suggest that a slightly improved sensitivity over the published SK analysis could result in discovery of a signal, and have helped motivate the research that led to this thesis.

1.5 The First SK Study

A paper was published in 2003 detailing the first search for the DSNB at SK [20]. This paper was the culmination of the thesis research of a student [21]. Although a DSNB signal was not seen, a flux limit was established that was ~ 100 times more stringent than the previous limit [22].

The basic method was to eliminate all conceivable backgrounds, then attempt to model the spectrum of the remaining backgrounds. A χ^2 fit was performed on the energy spectrum of the data sample, with two background components and one signal component. This method is benefited by how most DSNB models have very similar spectrum shapes. From this fit (Fig. 1.3), a final limit was extracted of $1.2 \bar{\nu} \text{ cm}^{-2} \text{ s}^{-1}$ for $E_{\bar{\nu}} > 17.3 \text{ MeV}$, which has remained the most stringent limit on DSNB flux until the research reported in this thesis.

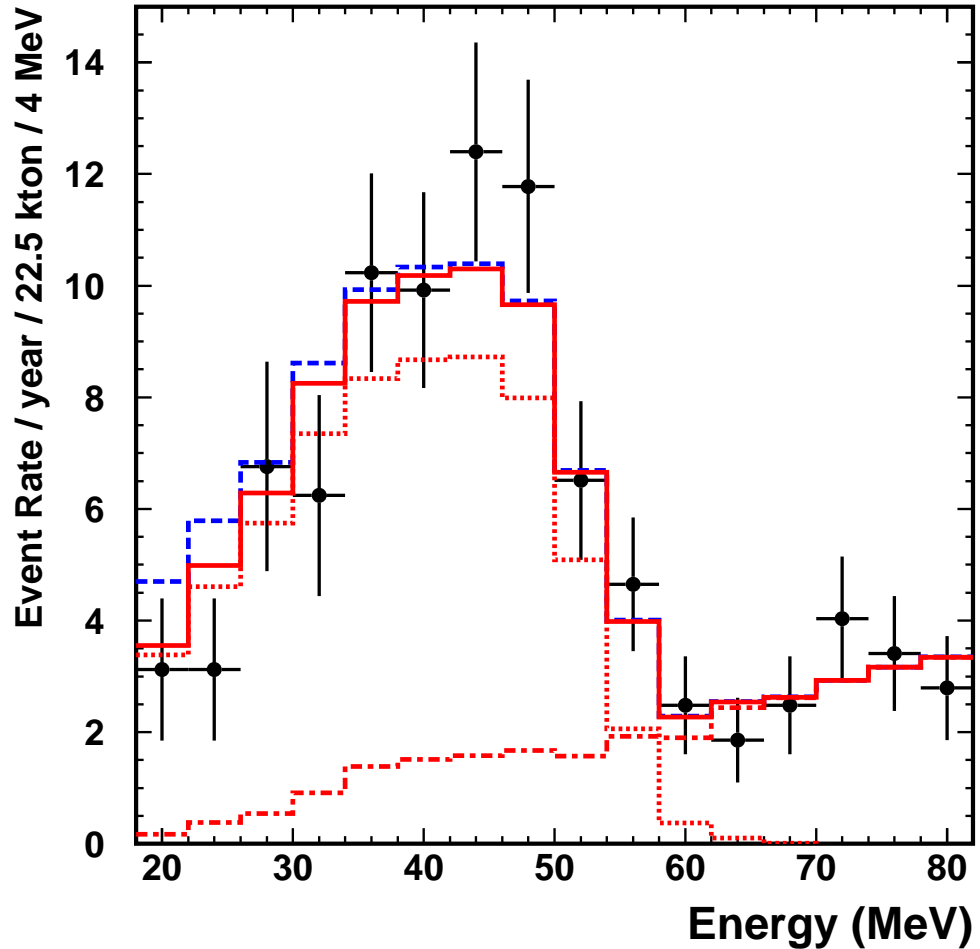


Figure 1.3: χ^2 fit of final data sample in published 2003 analysis. Overlaid on the black real data are dotted and dot-dashed red lines indicating the best fit ν_e and ν_μ charged current modeled backgrounds. Solid red is the sum of the two backgrounds, and dashed blue is with the DSNB 90% CL flux limit added.

1.6 Other searches for the DSNB

Although SK currently has the best sensitivity for seeing the DSNB signal in the world, other collaborations have performed searches that deserve to be recognized. A non-comprehensive list includes Kamiokande (1991, [23]), Mont Blanc (1992, [24]), SNO (2006, [25]), and KamLAND (2011, [26]).

Chapter 2

The Super-Kamiokande Detector

2.1 Introduction to the Detector

2.1.1 Detector Overview

After the success of the IMB and Kamiokande experiments, scientists were eager to build the next generation of detector. Although previously competitors, Americans joined forces with Japanese scientists on their new detector, and a new international collaboration was formed.

Originally KamiokaNDE meant Kamioka Nucleon Decay Experiment, as it was designed as a proton decay experiment. However, due to the exciting advances in neutrino physics, the primary focus of the new detector was changed, and the Kamiokande part of the new name, Super-Kamiokande, was chosen to be Kamioka Neutrino Detection Experiment.

The site of the detector is the same mine as that of the old Kamiokande experiment, the Kamioka mine in Japan. The mine, located precisely at Lat. $36^{\circ}25'32.5862$ N., Long. $137^{\circ}18'37.1241$ E., was once one of the world's largest Zinc mines, but now is used exclusively for physics experiments. The detector has an average of a 1 km rock overburden (2700 m.w.e.), which largely shields the detector from cosmic rays.

Cosmic ray muons of energy less than ~ 1.3 TeV cannot penetrate to the detector.

Super-Kamiokande (SK) is a giant 50 kton water Cherenkov detector in a stainless steel tank. The tank is a right cylinder 41.6 m high and 39.3 m in diameter. The detector is divided into two sections, the inner detector (ID) and outer detector (OD). The inner surface of the ID (32.5 kton) is lined with many (11146 for SK-I) inward facing 20 inch Hamamatsu R3600 Photo-Multiplier Tubes (PMTs). The PMTs give $\sim 40\%$ cathode coverage (except for SK-II). The rest of the ID surface is covered in opaque black sheet, which is a dense polyethylene telephthalate fabric. This reduces photon reflection and optically separates the ID and OD.

The surface of the OD is lined with 1885 outward facing 8 inch PMTs, allowing the OD to operate as a veto for events entering from the outside. The rest of the OD surface is covered in white Tyvek, to maximize photon reflection and improve the OD light sensitivity.

As of the time of this writing (2011), SK is the largest water Cherenkov detector tank ever built. The water within is kept ultra pure by continuous recirculation through an extensive water purification system (section 2.3). Due to the size of SK, it takes as long as two months to fill the tank with water when empty.

Above the tank is a research dome, which houses the control room, 5 electronics huts (which hold the DAQ [section 2.5]), the LINAC (a linear accelerator used for detector calibration [section 3.1]), and various instrumentation and storage.

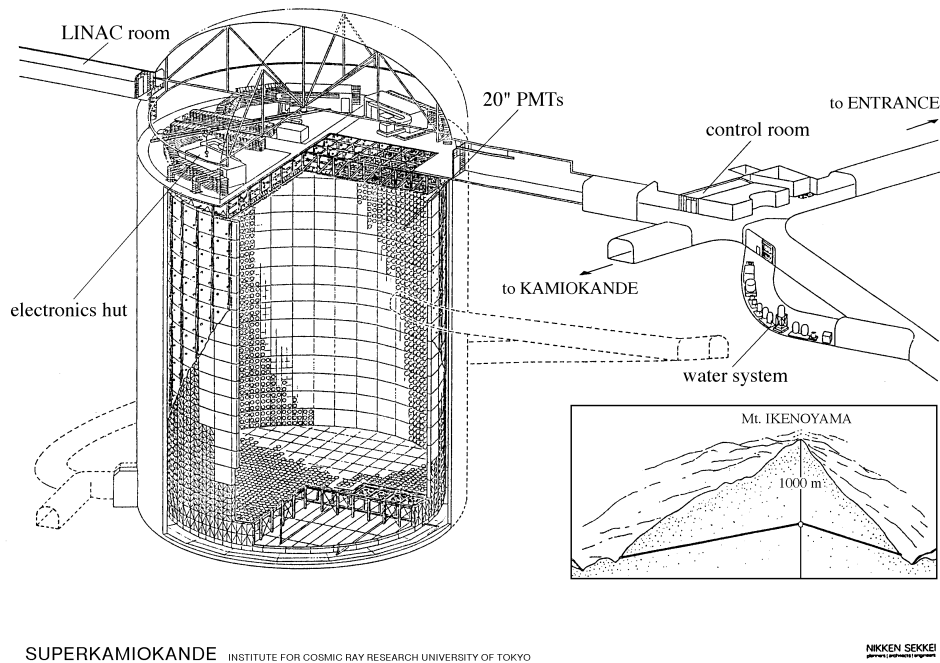


Figure 2.1: A schematic of the SK detector.

2.1.2 Timeline of the Detector

SK began operating in April 1996 with 40% ID cathode coverage and 11146 ID PMTs. In July, 2001, it was shut down for routine maintenance and upgrades. The period from April 1996 to July 2001 is referred to as the SK-I period. During this period, in 1998, the SK collaboration released the first highly significant experimental evidence for neutrino oscillations [27], and also confirmed the solar deficit [28].

On November 12, 2001, after the maintenance was completed and the tank was being refilled with water, a catastrophic accident occurred. One of the PMTs imploded when the tank was $\sim 75\%$ full, causing a chain reaction resulting in the implosion of almost all the underwater PMTs [29]. The chain reaction was violent enough that it registered as a seismological event to a seismological recorder 8.8 km distant.

6665 out of 11146 ID tubes were found to be destroyed. The water was drained again, and the broken glass cleaned. Unfortunately remaking so many PMTs is a

time consuming process, and it was decided to run the detector in the meantime. The surviving tubes were redistributed throughout the detector, after being fitted with new acrylic coverings (tube front) and ‘FRPs’ (fiberglass reinforced plastic, tube back), to prevent the shock wave of any future tube implosions from causing another chain reaction. The detector was turned back on with 19% cathode coverage (47% that of SK-I), and ran until the new PMTs were ready in July 2005. This period of data is referred to as SK-II.

In 2002, due to the success of the experiment, the head of the KamiokaNDE experiment, and SK collaborator, Masatoshi Koshiba, was awarded the Nobel Prize in physics (25%), along with Ray Davis Jr. (25%), “*for pioneering contributions to astrophysics, in particular for the detection of cosmic neutrinos*”.

The refitting of the PMTs took almost a year, and the detector was operational again in June 2006. In August 2008, the SK electronics system was completely overhauled and a new upgraded system was put in place. The data period from June 2006 to August 2008 is called SK-III. Since September 2008, after the electronics upgrade was completed, data taking has continued, and this period is referred to as SK-IV.

2.1.3 Detector Details

The SK tank is surrounded by 26 sets of vertical and horizontal Helmholtz coils to compensate for the Earth’s magnetic field, which can cause PMT response to be non-uniform. The coils reduce the ambient magnetic field from 450 mG to about 50 mG.

The PMTs used in SK are all hand blown borosilicate glass made by the Hamamatsu corporation. The 20 inch ID tubes (Fig. 2.2) were constructed specifically for SK. Originally all of the 8 inch OD tubes were Hamamatsu R1408 model, originally used in IMB, and then reused for SK. Unfortunately, the OD was also affected by the

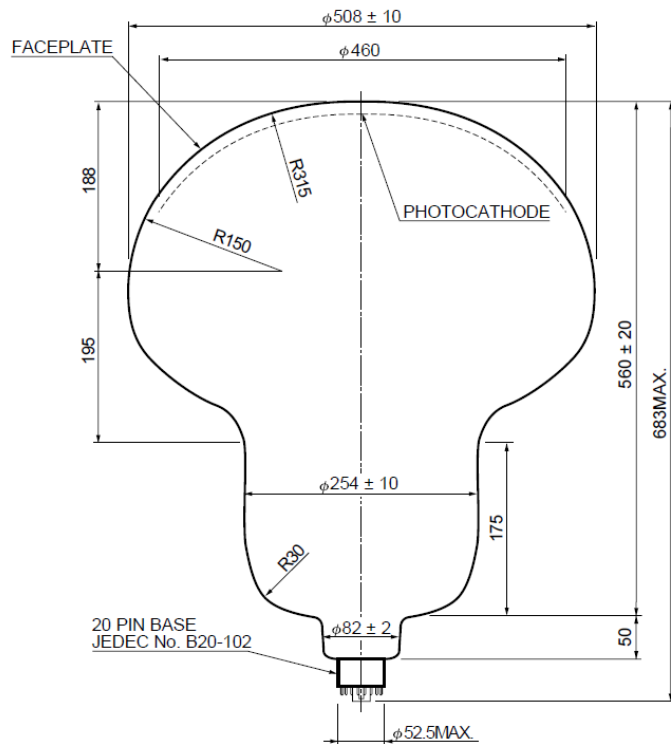


Figure 2.2: Schematic of the Hamamatsu R3600 PMT

2001 accident, and most of the OD tubes in the lower two thirds of the detector had to be replaced with new tubes. As of October 2010, 591 of the original IMB R1408 tubes remained, while 1253 of the tubes were the new, Hamamatsu R5912 model.

PMTs operate by releasing a photo-electron (p.e.) when struck by a photon (it doesn't always work; the success rate is measured by the tube's quantum efficiency). This photon is accelerated by a high voltage (about 2kV), then strikes a dynode. When an accelerated electron strikes a dynode, more electrons are released, which are all accelerated again to the next dynode. By the time the initial signal has made it through the series of dynodes, 1 p.e. will have turned into about ten million p.e. (gain of 10^7), which is output as an electronic signal to the DAQ. The downside to this design is that it is highly susceptible to false signals, where a thermally excited electron in the PMT itself starts the chain reaction without any photon causing it. PMTs show false positive low energy signals, or 'dark noise', at a rate of a few KHz.

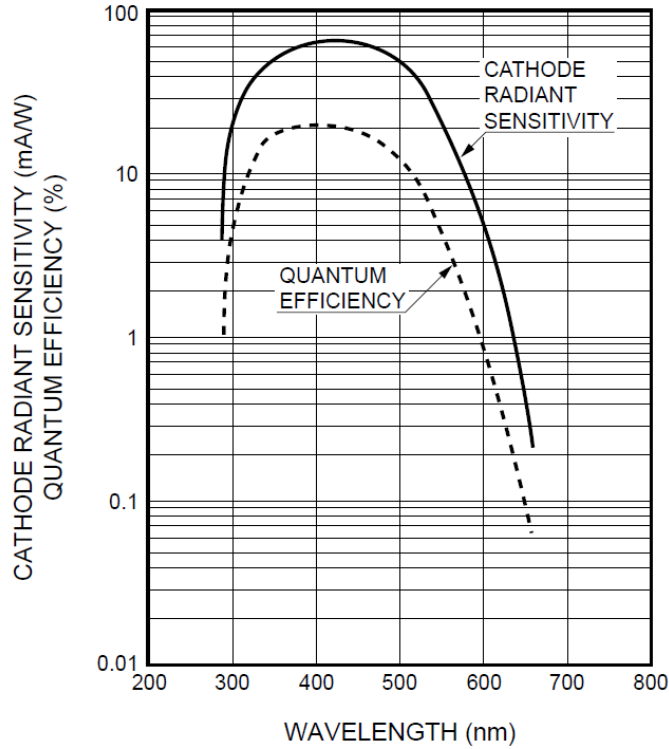


Figure 2.3: Quantum efficiency of the Hamamatsu R3600 PMT

The naturally cool temperature of the SK water helps keep the dark noise rate from being even higher.

The quantum efficiency (QE) of a PMT is defined as the percentage of time that an impinging photon will cause the PMT to fire. The QE is wavelength dependent, and the QE for the Hamamatsu R3600 model PMT used in the ID is shown in Fig. 2.3.

2.2 Physics in the Detector

As a water Cherenkov detector, SK operates by observing Cherenkov light. Cherenkov light is a ‘shock wave’ of light that occurs when something with charge travels faster than the speed of light inside a medium (never faster than the speed of light in vacuum), much akin to the sonic boom of sound that occurs when a physical object

travels faster than the speed of sound in air. The condition for a charged object to radiate Cherenkov light is often written in terms of the index of refraction of the medium, n , as $\beta > 1/n$, where $\beta = v/c$. Some example Cherenkov energy thresholds for charged particles are: $e^{+/-}$.767 MeV; $\mu^{+/-}$ 157.4 MeV; π^+ 207.9 MeV.

The Cherenkov light will be emitted at an angle θ_c with respect to the particle track direction, where $\cos\theta_c = 1/n\beta$.

For pure water, the index of refraction is about 4/3 (it's wavelength dependent). Highly energetic particles have a value of β very close to 1, which means they emit Cherenkov light at an angle θ_c of 42°. Electrons in the detector, being so light, tend to always be traveling at the speed of light, and emit light at this angle, while heavier particles often travel slower and emit light at smaller angles.

When a neutrino interacts in the SK detector, it can produce a charged particle such as an electron or muon with enough energy to create Cherenkov radiation. An electron will only travel a short distance in the detector (10's of cm) before becoming sub-Cherenkov due to energy loss, and can be considered point like. Even during the short distance it travels, however, it can produce enough light to be seen. The cone of light created will travel through the pure water and shine on the inner detector wall as a shape such as an ellipse, where the light intensity is recorded by the PMTs. Using the charge and timing of the light, critical information about the particle can be reconstructed, such as location, direction, and energy. An example event is shown in Fig. 2.6.

Muons can be more complicated due to the continuous emission of light as it travels in the detector, usually for the whole length of the detector before exiting. Some muons are created by neutrino interactions, but many more (~ 2 Hz) are cosmic ray muons that penetrate the rock overburden and enter the detector. These events are easily distinguishable from muons created in the detector by use of the OD, and the entire muon track can usually be reconstructed. Other charged particles, such as

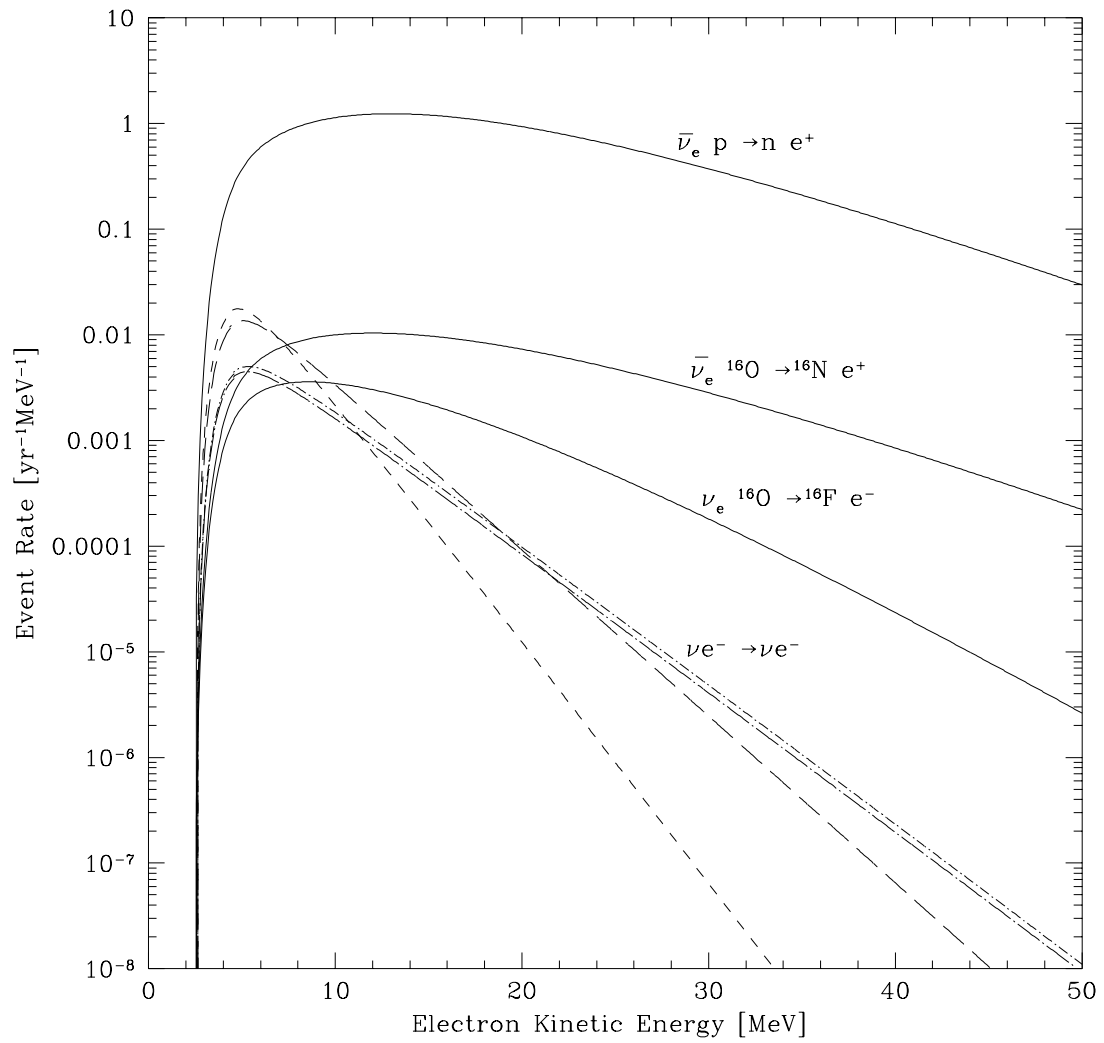


Figure 2.4: Interaction modes of DSNB neutrinos in SK as calculated by [30].

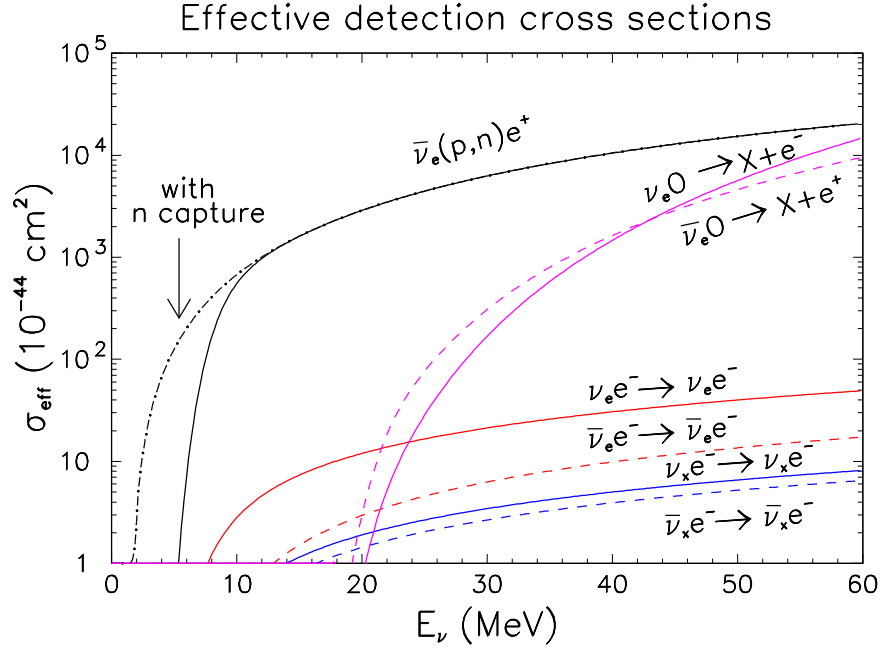


Figure 2.5: Neutrino interaction cross sections in a large water Cherenkov detector, including resolution and threshold effects, from [8].

pions, are also seen.

SK can see neutrinos from the sun, from atmospheric cosmic ray interactions, from supernovae, from neutrino beams, and most likely from nuclear reactors, though these are incredibly hard to isolate. Due to SK's large size, the detector is also useful for proton decay and dark matter searches. As this thesis is dedicated to SN relic neutrinos, little detail will be given about the solar [31, 32], atmospheric [33], beamline, proton decay [34], or dark matter analyses [35], but information can easily be found in the given references.

DSNB events would interact in SK mostly by means of inverse beta decay ($\bar{\nu}_e + p \rightarrow e^+ + n$), about 100 times more than the next most likely interaction mode (see Figures 2.4 and 2.5). Because this is the dominant reaction, SK is almost exclusively sensitive to electron type anti-neutrino DSNB events. Furthermore, a free neutron is created in the reaction. In pure water, this neutron is captured by hydrogen, producing a 2.2 MeV gamma ray that is usually not detectable, but could possibly

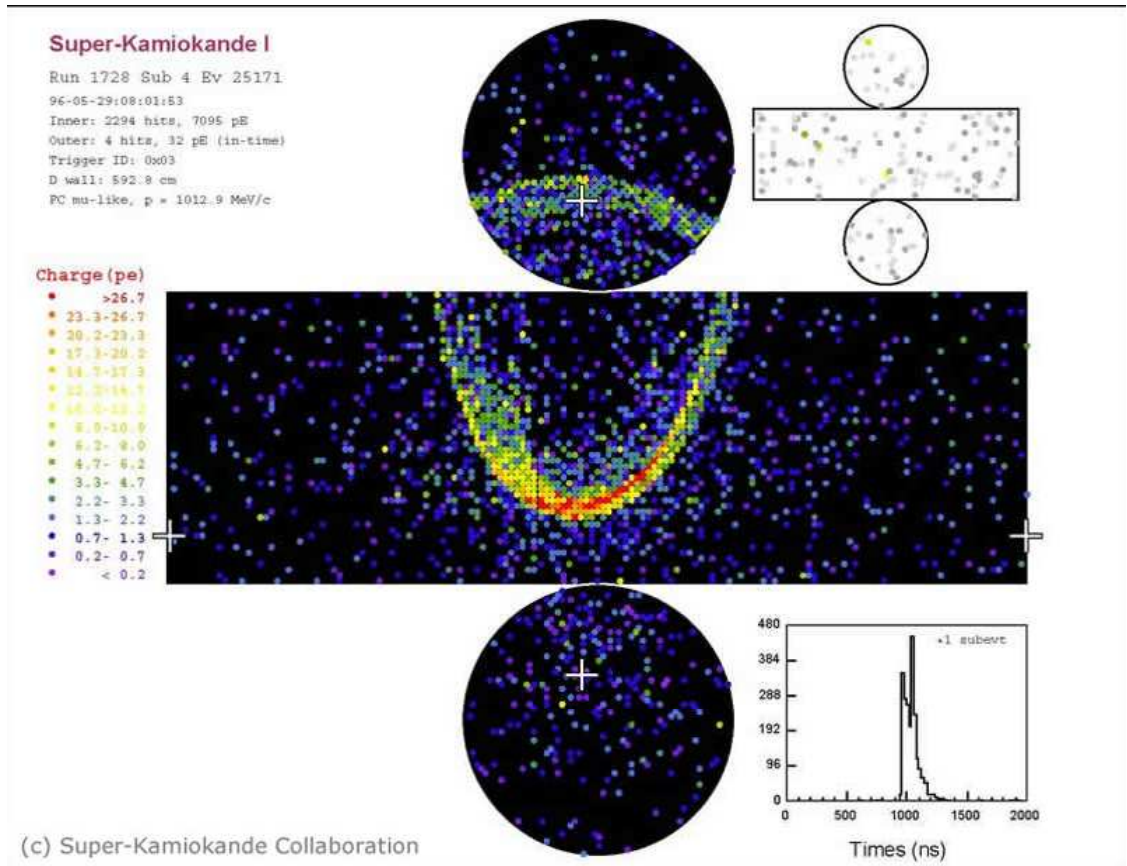


Figure 2.6: A muon neutrino event interacting in the SK detector and making a muon, the Cherenkov light from which shines on the inner wall of the detector in a ring (or conic section).

be seen in rare occasions or if the detector energy threshold can be lowered. This neutron however opens up the possibility for possible neutron tagging physics in future water Cherenkov experiments with the addition of a doping material (for example, gadolinium [36]).

2.3 The Water System

Water purity in the detector is of primary importance. The water needs to be clear, so the Cherenkov light can travel through it and reach the tubes without obstruction. Furthermore, the water needs to be kept clean of radioactive particles that can cause background.

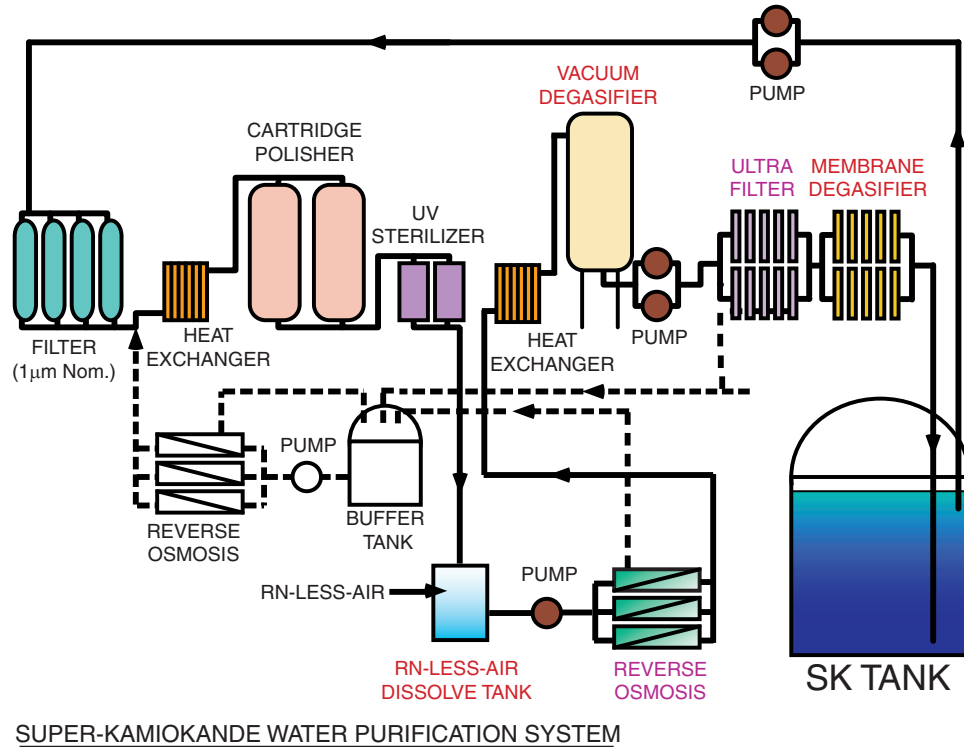


Figure 2.7: Schematic of the SK Water Purification System.

The SK water supply is a small river that runs through the mine. This water must be filtered to meet the detector standards. The SK water is continuously recirculated through the filtration system, at a rate of 30-60 metric tons per hour (usually around 50). This is also the fill rate when the detector is emptied.

The water system is pictured in Fig. 2.7. It starts with 1 μm mesh filtration to remove larger particles and contaminants. A heat exchanger keeps the water cool (around 13° C) in order to curb bacterial growth. An ion exchanger removes ions, and UV radiation kills bacteria. It is further filtered through reverse osmosis, and a vacuum degasifier removes dissolved oxygen and radon gas ($\sim 96\%$ effective). An ultrafilter removes particulates down to a size of 10 nm, and a membrane degasifier further reduces radon and other dissolved gases.

Water entering the detector from the filtration system has a resistivity of around 18.2 $\text{M}\Omega\text{-cm}$, near the chemical limit, and radon in the water passing through the

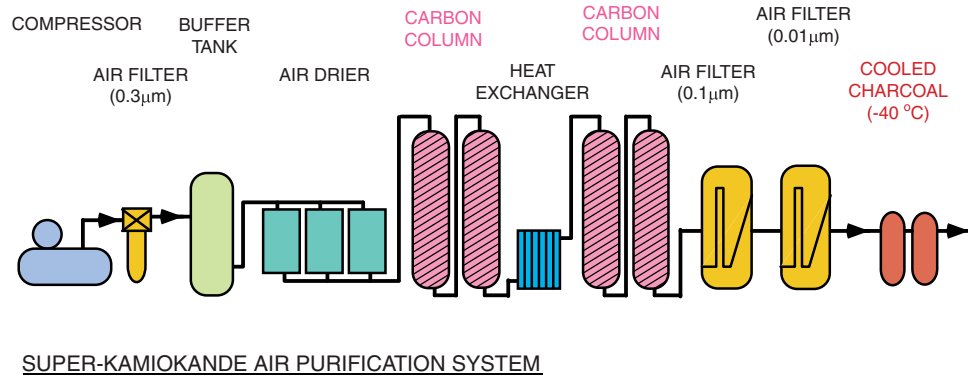


Figure 2.8: Schematic of the radon free air system.

system is reduced by about seven orders of magnitude.

2.4 Radon Free Air System

The water isn't the only thing that needs to be kept clean. Being a deep mine, there are radioactive elements present in the rock and air that can not only cause background in the detector, but can also be harmful to the health of workers in the mine. Most important of these contaminants is radon. In the mine, radon levels are seasonal due to varying temperature differences and airflow. In the winter, radon concentrations tend to be a few hundred Bq/m^3 , while in the summer the concentration is much higher, usually a few thousand Bq/m^3 . Two special systems were developed, one to keep the air in the detector area (dome and water purification system areas) clean of radon, the other to reduce radon in the detector itself.

The detector system (pictured in Fig. 2.8) supplies purified air to the gap between the top of the water and the lid of the tank. The system for the dome and surrounding area starts at a hut outside the mine entrance. Here, fresh outside air is collected, pressurized, and passed through a series of carbon filters and cooled charcoal, which remove the radon. The fresh air is then pumped into the SK work area in the mine at a rate of about $10 \text{ m}^3/\text{min}$. The system removes more than 99.9% of the radon in the air that passes through it, and keeps radon concentrations in the

detector area to 10-40 Bq/m³, which is safe for a sustained human environment.

2.5 The DAQ

This is just an overview of the pertinent information regarding the DAQ; more detailed information on the DAQ hardware and structure can be found in reference [37].

2.5.1 ID DAQ

In 2008, the SK ID DAQ was overhauled and replaced with new, custom hardware. As this thesis focuses solely on data prior to this renovation, the new DAQ will not be described. Detail on the new DAQ can be found in references [38, 39].

The ID and OD data acquisition systems (DAQs) are separate, and were designed independently for different purposes.

Each PMT in the ID is connected via cable to an Analog Timing Module (ATM). These modules are located in the peripheral electronics huts in the dome above the tank. The ATM modules take the analog timing and charge information from a PMT and digitize it using a 12 bit ADC. Each ATM module can handle up to 12 PMTs. The ATM modules are grouped physically inside of what are called TKO (Tristan KEK Online) crates [40]. There are 48 TKO crates, each holding up to 20 ATM modules.

Each PMT has 2 channels on an ATM module, so that when reading out and digitizing the data from one channel, data can be collected on the secondary channel, reducing dead time. Each PMT signal is amplified and split 4 ways: the two digitizer channels, a discriminator, and one to the flash ADC DAQ. The discriminator channel checks if the signal passes a threshold of 0.25 p.e., and if this threshold is reached, the PMT triggers. The ADC starts to digitize the information from one of the 2 signal channels and store it in its first in first out (FIFO) internal memory, and a 200 ns, -15

mV square wave pulse is sent to a global trigger (HITSUM). 200 ns is approximately the longest time it could take for a Cherenkov photon to travel through the detector.

The ID-HITSUM signal is passed through an AC coupled discriminator to subtract out dark noise. After this process, the signal is reduced to approximately -11 mV/PMT.

The global trigger HITSUM is the analog sum of all self triggers, and any time the square waves add up to more than a certain threshold, a global trigger is issued. Information for each hit ID PMT is stored for 400 ns before and 900 ns after anytime a global trigger is issued, for an event window of $1.3 \mu\text{s}$. In the case of a global trigger, the digitized timing and charge information is sent to and stored in Super Memory Partner (SMP) boards, one per TKO crate, from which the data is eventually read out by server computers in the central electronics hut via an optical network called the Fiber Distributed Data Interface (FDDI), and saved to permanent storage. If a global trigger is not issued within sufficient time, the PMT information stored in the internal FIFO memory of the ATM module is discarded.

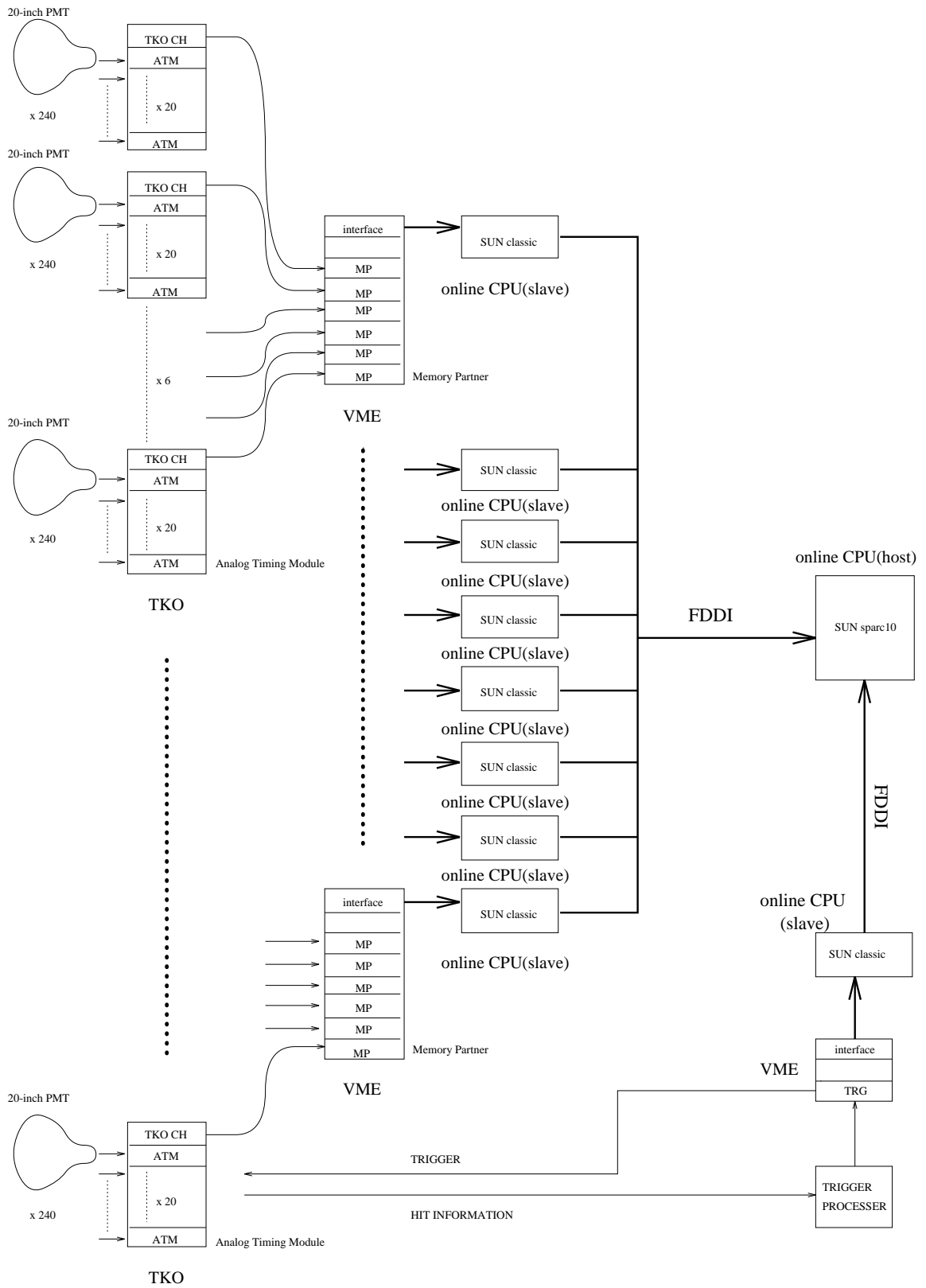


Figure 2.9: Schematic of the SK ID DAQ.

window means separate but overlapping events occur more frequently.

2.5.3 Triggers

The detector has multiple triggers useful for different analyses. There are four main trigger types: the ID triggers (high energy [HE], low energy [LE], and super low energy [SLE]), each of which have a different HITSUM threshold, and the OD trigger. Any of the four triggers will result in a global trigger which stores the event information into permanent storage.

The HE trigger is mostly used for atmospheric neutrino studies. The LE trigger is good for SN relic events and solar neutrino events. The SLE trigger was introduced to look for low energy solar neutrino events. The lower threshold of the SLE trigger causes a much higher trigger rate (roughly an order of magnitude more triggers per MeV the threshold is lowered). Much of the increase comes from background, such as gammas from the rock walls and radioactivity from the PMT glass itself. In order to effectively lower the low energy threshold and not be swamped by background, a prefilter was introduced for SLE events called the intelligent trigger (IT). The IT does a quick vertex fit to SLE events and only saves those within the fiducial volume (inner 22.5 ktons), eliminating much of the background. As computing power increased throughout SK-I, the IT system was upgraded to handle a higher event rate, and the SLE threshold was lowered multiple times as SK-I progressed. During SK-II, all thresholds were lowered to reflect the decreased cathode coverage. Trigger thresholds are summarized in Table 2.1. The OD trigger has remained constant at 19 OD hits.

Table 2.1: ID Trigger thresholds for SK-I through SK-III.

Name	SK-I Threshold	SK-II	SK-III
HE	-340 mV (31 hits, about 6 Hz)	-180 mV	-320 mV
LE	-320 mV (29 hits, about 16 Hz)	-152 mV	-302 mV
SLE1	-260 mV (May 1997 to May 1999)	-110 mV	-186 mV
SLE2	-250 mV (May 1999 to Sep 1999)		
SLE3	-222 mV (Sep 1999 to Sep 2000)		
SLE4	-186 mV (Sep 2000 to July 2001)		

Chapter 3

Detector Calibration

Herein I will summarize relevant detector calibrations; more details on many of the calibrations can be found in [37].

3.1 LINAC

A medical LINear ACcelerator (LINAC) was acquired from a hospital and converted into a calibration tool for SK in 1996 (described in depth in [41]). Permanently housed in the dome area above the tank, the variable energy (roughly 5-18 MeV) mono-energetic electron beam can be controlled (through bends and around corners) with a series of steering magnets. Beam intensity is tunable, and the beam can be collimated such that electrons are injected into the tank at a low enough rate (down to around 0.1 per 2 μ s microwave pulsed ‘bunch’) to allow single electron events (multiple electron events can still rarely occur, and are identified during the offline analysis). The exact beam energy is measured with a germanium detector with an energy resolution of 1.92 keV.

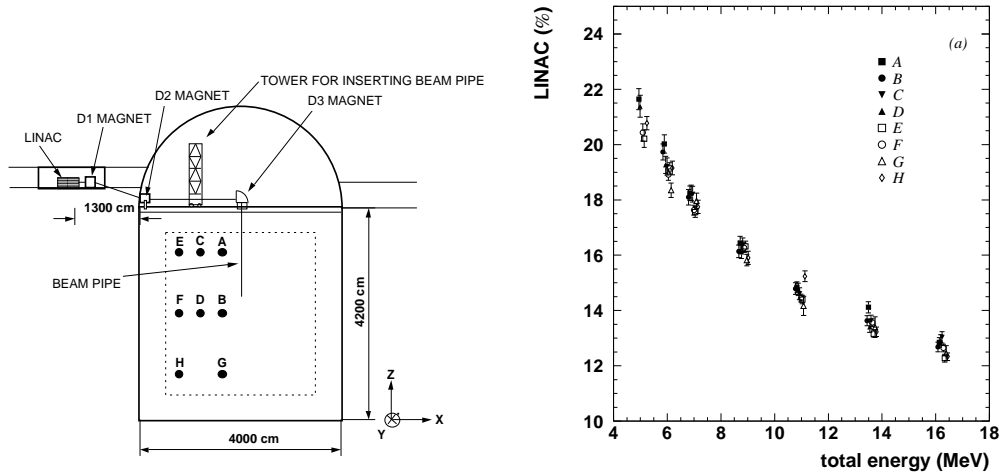
Multiple calibration port holes exist on the top of the detector, and the beampipe can be lowered to a variable depth in the detector. In this fashion, many different areas in the detector are accessible and can be calibrated (for example, to check the

center of the detector compared to the sides, or the top compared to the bottom). LINAC calibration data is taken after any major change to the detector to ensure MC and data quality.

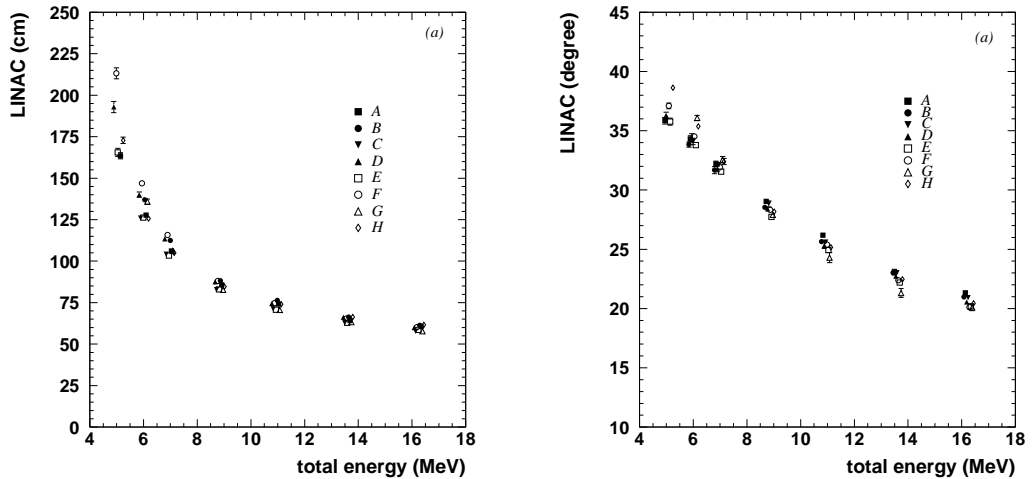
The LINAC was developed for the solar neutrino analysis, for which the energy scale was measured to better than 1%. The energy scale can be extrapolated to higher energies, however, and this calibration is also relevant for the DSNB analysis.

Knowing the location of the injection point also allows the data to be used to check the accuracy of vertex and direction reconstruction software. For example, in SK-I, the LINAC data shows the energy resolution to be between 21% at 5 MeV to 13% at 16 MeV; the vertex resolution to vary from 180 cm at 5 MeV to 50 cm at 16 MeV; and the angular resolution to go from 37 degrees at 5 MeV to 21 degrees at 16 MeV, as can be seen in Fig. 3.1. SK-II energy resolution is about 18% at 16 MeV, and vertex resolution is about 80 cm at 14 MeV [32]; for SK-III all resolutions are slightly slightly better than SK-I [42].

The LINAC has one major drawback: the beam pipe must always be directed in from the top of the detector, thus only allowing a beam with a downwards direction. Just as energy and position can be varied, it would be ideal if direction could be varied as well to check all combinations of parameters.



(a) Schematic of the LINAC system. Various calibration points in the detector are shown. (b) Energy resolution in SK-I as measured by the LINAC at various energies and beam injection position.



(c) Vertex resolution in SK-I as measured by the LINAC at various energies and beam injection position. (d) Angular resolution in SK-I as measured by the LINAC at various energies and beam injection position.

Figure 3.1: LINAC information

3.2 DT Generator

A deuterium-tritium (DT) generator is used to check the absolute energy scale for low energy events [43]. It operates in conjunction with the LINAC, providing a cross check on the energy calibration. It is less time consuming to use than the LINAC and better for monitoring long term stability with frequent checks. Furthermore, the

device output is isotropic, and isn't limited to only downward going events like the LINAC, thus allowing study of direction dependent effects.

The device is a custom built calibration tool consisting of a computer operated crane that lowers the DT generator itself into the detector, and can raise and lower it to specific depths. The accelerator isotropically produces 14.2 MeV neutrons via the reaction ${}^2\text{H} + {}^3\text{H} \rightarrow {}^4\text{H} + n$, and the neutrons can then interact with ${}^{16}\text{O}$ in the SK water to produce ${}^{16}\text{N}$. The ${}^{16}\text{N}$ isotropically beta decays, with the primary mode (66%) having a half-life of 7.13 seconds and being accompanied by a 6.13 MeV gamma. The second most likely mode (28%) has no accompanying gamma ray.

DT data is taken every few months, and the energy scale as determined by the DT agrees with the results of the LINAC calibration to better than 1%. Various positions in the tank are monitored to assure the energy scale at all regions are consistent.

3.3 PMT Calibration

The detector PMTs need to be calibrated in order to understand the data properly. The PMT timing and gain are especially critical; the PMT hit timing is the fundamental quantity that underlies all SK data, and the recorded charge, which is affected by the gain, is also critical (for muon reconstruction, even if not for SN relic events, which make a 1 p.e. per PMT assumption).

The PMT gain is approximately 10^7 , but needs to be calibrated for each PMT (by adjusting the PMT voltage), as a uniform detector response is desired to minimize systematic errors. In order to achieve uniform response, the relative gain of each PMT in SK is measured using a Xe lamp which is capable of producing light flashes of very consistent (within 5%) intensity. Briefly described, the light from the Xe lamp is split, and fed to a reference, as well as a scintillator ball which produces almost uniform light

similar in wavelength to Cherenkov light (peaking at 440 nm). The light recorded by each PMT is then corrected to take into account distance traveled by the light in water (water transparency effects), PMT acceptance (geometry), and scintillator ball non-uniformities. After corrections, the light is compared to the reference to determine the PMT gain, which can be tweaked by adjusting PMT voltages. For SK-I, the spread in the PMT gain was about 7%. For SK-II and SK-III, a method of pre-calibrating some PMTs before mounting them in the tank, which the surrounding PMTs could then be compared to, allowed improved measurements, and the SK-II and SK-III gain spreads were within 2%.

PMT absolute gain is also measured. Even if the gain of each PMT is the same, it is important that amount be carefully understood. This number is expressed as a conversion between ADC charge and number of photo-electrons. To measure this, a Ni-Cf source was used. The Cf source emits neutrons which are captured on Ni wire, causing the emission of 6-9 MeV gamma rays. This source causes events with around 50 hit PMTs, >99% of which are only 1 photo-electron hits. The resultant conversion factors were as follows: 2.055 pC/p.e. for SK-I; 2.297 for SK-II; and 2.243 for SK-III. The Ni-Cf source is also used to measure the quantum efficiency (QE) of each PMT on an individual basis. Not only can the QE for a PMT differ slightly from the manufacturer's specifications, but the tubes installed in SK-III to replace those destroyed in the accident are newer than the others and somewhat different (higher quality in general).

Furthermore, in SK-II the Ni-Cf calibration found that in general the hit rates of PMTs in the top of the detector were lower than those on the bottom by 3-5%. This leads to a 'top-bottom asymmetry', which was carefully measured and modeled in the MC by means of adding a z dependent term to the light absorption parameter. As the Ni-Cf source releases gammas isotropically it can also be used to calculate any vertex shift in the reconstruction software, which could cause events actually in the fiducial

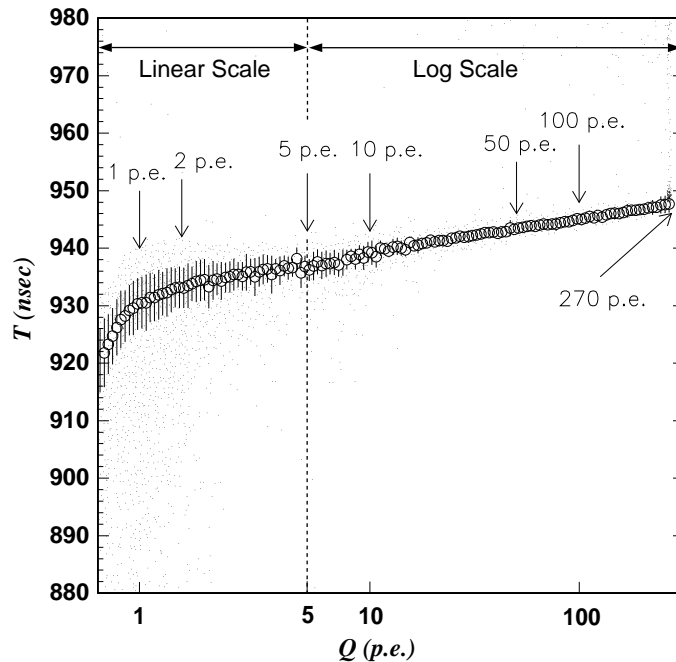


Figure 3.2: Example TQ map. Larger timings (vertical axis) represent earlier hits.

volume to reconstruct outside the fiducial volume or vice-versa. Any systematic bias in the fitter could cause an error in the number of events in the fiducial volume; this error is measured to be on the order of 1%.

PMT timing must also be checked. Due to slewing, or the ‘time walk’ effect (where larger charge hits exceed the TDC threshold more quickly, causing different response even if the hit time is the same) PMT response can vary as a function of the amount of charge seen, which must be understood. Scatter plots of PMT timing vs. pulse heights (called ‘TQ maps’) are constructed using a N_2 laser connected to a diffuser ball, which is capable of creating diffuse light with a very small timing spread. A typical TQ map is shown in Fig. 3.2. The light intensity can be varied to measure the PMT timing response for different light inputs. The PMTs typically have a measured timing resolution of around 3 ns for a single photo-electron pulse height.

The PMT timing resolution is fine enough that for proper accuracy, the length of the cables connecting the tube (in the tank) to the electronics system (in the dome

on top of the tank) must be measured and taken into account as well. In SK-I and SK-II, to find the ‘time’ of the event for N₂ laser calibration data, the average of the TOF-subtracted timing distribution for the event (after noise hits are cleaned from the event) is used. However, this average can be affected by late or scattered hits, which can be a position dependent effect. For events closer to the walls, for instance, reflected hits are more likely, leading to systematic errors in this calibration. For SK-III, the method was improved by using the timing peak rather than the average, which led to greater timing accuracy.

3.4 Water Transparency

3.4.1 Laser Measurements

Lasers are used to directly measure light scattering and absorption parameters in a variety of wavelengths. SK-I and SK-II mostly used a titanium sapphire laser (tunable to output light between 350 and 500 nm), a diffuser ball, and a CCD camera. Laser light is directed through the diffuser ball via optical fiber and recorded by the CCD at different distances; the change in intensity over distance allows determination of the water transparency. Data must be taken at regular intervals as the water transparency changes over time. For SK-III, Nitrogen and dye lasers were used, at 337 nm, 365 nm, 400, and 420 nm. The light attenuation length from laser measurements tends to be about 90 meters and agrees well with separate measurements using cosmic ray muons. However, for the SN relic study, this data was only used as a cross check, and the water transparency parameters were obtained by the decay electron method described below.

The SK MC utilizes a model with one water absorption parameter, and two water scattering parameters (for Mie and Rayleigh scattering). The MC parameters are obtained from the laser measurements as well.

3.4.2 Decay Electrons

Cosmic ray muons enter the detector at a rate of about 2 Hz, and about one in 20 will stop in the detector. These stopping muons decay into electrons with the well known Michel spectrum. These decay electrons can be identified by associating the event with a muon that closely precedes it in time, and whose reconstructed muon stopping point is near (< 5 m) in space to the location of the decay electron vertex. With about 2850 live days of data from SK-I through SK-III, a very large sample of the events accumulate, and they can be used as an independent means of monitoring detector stability.

Water transparency can be calculated from the decay electrons recorded during the time in question. While maintaining the water transparency table for the SK low energy group for SK-III (particulars of the SK-I and SK-II methods vary only slightly, and are detailed in [37]), I used six day bins. During six days, many thousands of decay electrons would be recorded.

A few simple cuts were required to ensure the decay electron quality, including requiring that the decay electron follow the parent muon by between three and eight microseconds, in order to prevent contamination by events from the hardware after-triggers (forced triggers that occur set times after HE triggers in order to try and catch decay electrons, but often are empty; sufficient statistics exist that carefully selecting the true decay electron events from this sample is not necessary). The standard fiducial volume cut (where any event within 2 meters of the inner detector wall is cut out) is also applied.

After cuts, the light recorded by the PMTs during each event were binned by distance from the event vertex to the PMT. For each event only information inside of a 50 ns time window was used. The amount of contribution from each PMT was corrected for occupancy and geometry, in the same way as these terms are corrected for in the energy reconstruction (see section 4.2). When fitting each decay electron,

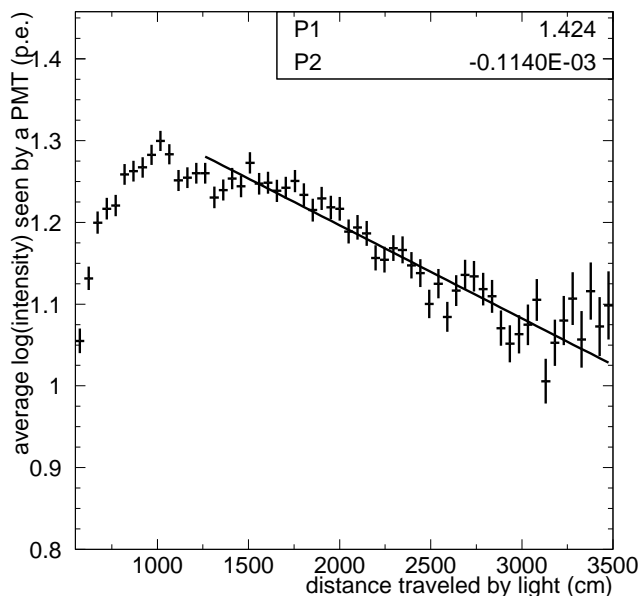


Figure 3.3: The light intensity vs. distance distribution used to determine water transparency from decay electrons, for a example 6 day period. The first bins exhibit strange effects, and are neglected.

and when reconstructing the energy, both of which occur at the beginning of the decay electron event selection, a water transparency must be assumed, so the process of determining the water transparency from decay electrons is iterative. Once a distribution of light intensity vs distance the light has traveled is obtained (see Fig. 3.3), a simple line is fit to the data, and the water transparency is simply the inverse of the fit slope. The first bins of the distribution are not used in the fit, due to strange effects for light traveling shorter distances, which were never fully understood. The fit was found to be more accurate if the y-intercept of the fit line was fixed to an average value, as opposed to a free-floating y-intercept. An error on the fit is also recorded.

The water transparency is not constant (Fig. 3.4). Changes in temperature, alterations to the water system, introduction of contaminants, and more can all affect the water transparency, making constant monitoring of the water transparency critical

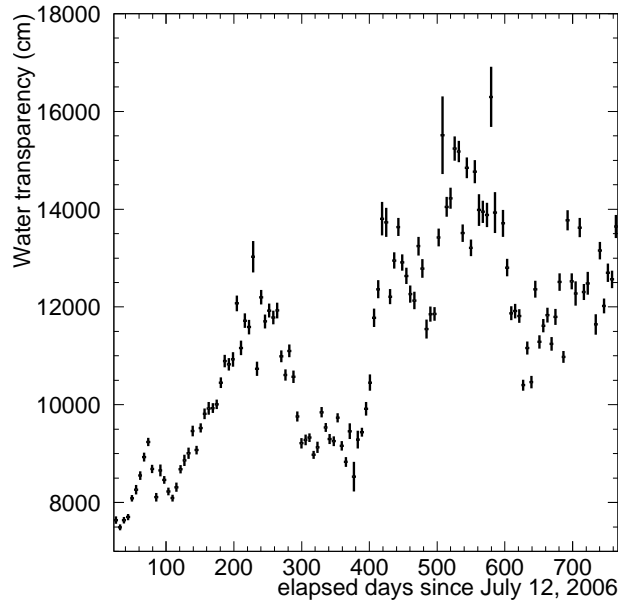


Figure 3.4: Water transparency of SK-III, from the decay electron method. The bin to bin variation in some cases exceeds the statistical error; this effect was not well understood.

for accurate data analysis. A water transparency is used in the fitting process as a correction to the light intensity recorded by each event. This correction, along with occupancy and geometry effects, is used to convert the number of hits seen in the event (within 50 ns) into an ‘effective’ number of hits, a number which is directly proportional to the energy of the event.

Because of this, the accuracy of the water transparency measurement can be verified by monitoring the stability of the average value of this ‘effective’ number of hits over time. Fig. 3.5 shows the average value of this parameter over time, as opposed to assuming a constant water transparency of 90 meters. We can see that by using the final values of the water transparency from decay electrons, the most stable distribution is obtained. In fact, the average effective number of hits was stable to within 1% over all SK-III.

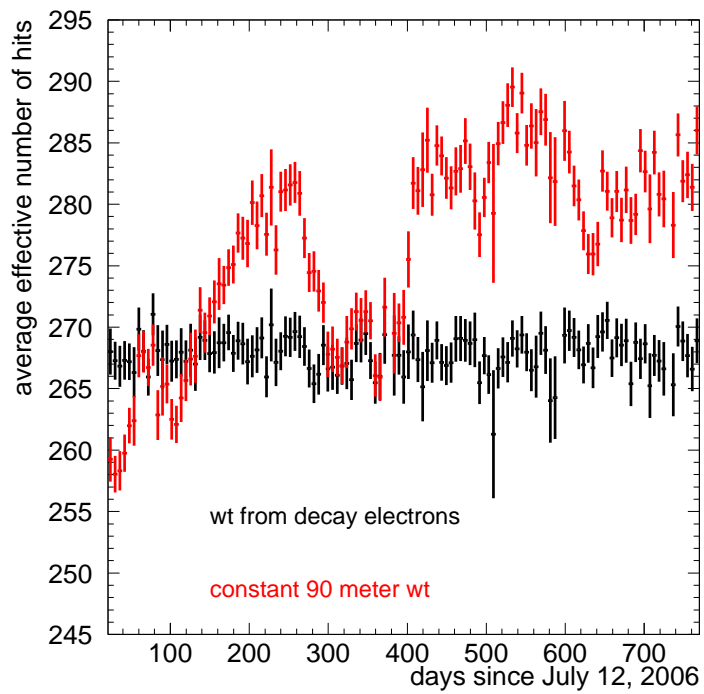


Figure 3.5: The difference in the stability of effective number of hits (see Eq. 4.1), depending on water transparency assumed. Assuming a constant 90 meter water transparency causes the N_{eff} to vary greatly, tracking the true water transparency. The variation of N_{eff} assuming the water transparency from decay electrons is stable to within 1%.

Chapter 4

Software Tools

4.1 Vertex Reconstruction

Electrons and positrons resulting from an interaction will only travel a short distance (~ 10 cm at 20 MeV, and ~ 20 cm at 50 MeV) before stopping in the detector, and are considered point sources (an assumption that may come close to being inaccurate at the highest energies, but is still reasonable considering the small distances compared to the size of the detector). Reconstructing the vertex of these events is of primary importance. Numerous vertex fitters were developed for the solar analysis. The one with the best vertex resolution is BONSAI (Branch Optimization Navigating Successive Annealing Iterations, with a vertex resolution of better than $50 \text{ cm} > 16 \text{ MeV}$), which fits events based almost entirely on PMT hit timing.

In BONSAI, many possible starting points are constructed out of combinations of four hit PMTs, for which a likelihood is calculated by matching timing residuals to a timing residual likelihood shape determined from LINAC calibration data. The likelihood is maximized by checking against 12 nearby points on a grid of successively smaller sizes, down to 1 cm. A flat dark noise component is assumed. Bonsai was used for all low energy ($< 100 \text{ MeV}$) non-muon fits in the DSNB study. BONSAI

was introduced in the SK-II solar analysis, and is described there in more detail [32]. One nice feature of BONSAI is that it is least likely of all the SK low energy vertex fitters to misfit an event. The fitter also returns a fit goodness value which can be used to evaluate the quality of the fit, and identify misfits.

4.2 Energy Reconstruction

First, it should be noted that all particle energies considered in this thesis are quoted in terms of total energy, not visible energy. Secondly, the energy reconstruction always assumes that the base particle is an electron (or positron). Other events (such as a pion or muon) for whom this reconstruction algorithm is applied will be assigned an energy that will be inappropriate; for instance a pion with a total energy of some hundreds of MeV could conceivably be reconstructed as having an energy of 40 MeV total energy, which is less than the pion rest mass and unphysical. However, all events have a reconstructed energy using the following algorithm (since in many cases it is not certain what the particle that caused the event really is), and all energy values should be considered as a ‘total electron equivalent energy’. Ultimately this search looks for inverse beta decay positrons, and we can hope to remove all events that aren’t electrons or positrons through our cuts.

The energy reconstruction algorithm used was originally developed for the SK solar neutrino analysis. However, events up to 100 MeV are considered ‘low energy’ in SK, and the energy reconstruction can be applied to events at these higher energies. For very low energy events (electrons and positrons < 5 MeV or so), PMTs are typically hit by only one photon, and event energy can be reconstructed from the number of hit PMTs, ignoring the amount of light seen by each PMT. The higher the energy of the event, the more the one photon per PMT assumption breaks down; a correction is applied for accurate energy reconstruction.

To reconstruct the energy, first most of the dark noise is filtered out, by only considering hit PMTs with time residuals in a 50 ns window. Then the number of PMT hits is converted into an ‘effective’ number of hits, N_{eff} , by applying a few corrections. N_{eff} represents the number of photoelects. The formula is as follows (from [31]):

$$N_{eff} = \sum_{i=1}^{N_{hit}} \left((X_i + \epsilon_{tail} - \epsilon_{dark}) \times \frac{N_{all}}{N_{norm}} \times \frac{R_{cover}}{S(\theta_i, \phi_i)} \times e^{\left(\frac{r_i}{\lambda(r_{un})}\right)} \times G_i(t) \right) \quad (4.1)$$

Where X_i is the occupancy correction (described shortly), ϵ_{tail} and ϵ_{dark} are corrections for dark noise and late time hits (generally there is a measurable tail of late time hits due to multiple Coulomb scattering); N_{all} is the total number of PMTs in the experiment phase (11146 for SK-I), and N_{norm} are the number properly operating, thus making the second factor a correction for bad (broken or hot) PMTs; the third factor is for PMT photo-coverage, with R_{cover} being the ratio of area on the walls covered by PMTs to full inner detector area (0.4041 in SK-I), and $S(\theta_i, \phi_i)$ taking into account how the PMT coverage changes with incidence angle (PMT shadowing effects); fourth is the water transparency (λ) correction, with r_i being the distance from reconstructed event vertex to hit PMT; and lastly $G_i(t)$ is a single photon time dependent gain factor.

The occupancy is the correction that allows reconstruction of higher energy events that break the single photon per PMT assumption. The basic idea is that the Cherenkov ring doesn’t only strike one PMT in isolation. If a PMT is going to detect multiple photo-electrons, it is likely that the PMT is located in the center of a ‘bright spot’. If this is true, then it is likely that the neighboring PMTs also detected light; in fact the brighter the spot, the more likely multiple photo-electrons were detected, and the more likely that the neighboring PMTs detected light.

Since the algorithm doesn’t use the information of the intensity of light detected by the PMT, each PMT to start is simply assigned a value of 0 (not hit) or 1 (hit).

So for every hit PMT, the 8 neighboring PMTs (the PMTs are aligned on a grid) are searched. If none, or just a few are hit, then it is likely that the PMT is in a dim region of the Cherenkov ring (the entire ring may be dim for low energy events), or saw light simply because of a scattered photon, or a coincidental dark noise fluctuation, and little or no correction is applied ($X_i \sim 1$). If many of the neighboring PMTs are struck however, it is likely that the PMT is in the middle of a bright spot of light, and the PMT is given a value larger than one. If all eight neighboring PMTs are also hit, then the hit PMT under consideration is assigned a value of 3, which basically means it should be treated as if it saw three photo-electrons.

Formally, if we define the fraction of the nine PMTs in the 3x3 patch that are hit as x_i (the center tube is always hit by construction), then if all 8 neighboring PMTs are hit ($x_i = 1$), then $X_i = 3$; otherwise, from Poisson statistics,

$$X_i = \frac{\log \frac{1}{1-x_i}}{x_i} \quad (4.2)$$

The energy calculation is described in more detail in the SK-I solar paper [31]. The energy resolution for an 18 MeV event is about 10%.

4.3 Direction Reconstruction

Incoming neutrinos that interact through elastic scattering create recoil electrons that retain the directionality of the neutrino to within about 15 degrees (in general, positrons formed through inverse beta decay do not retain a significant correlation to the incoming neutrino, although a very weak backwards bias exists below 15 MeV, and slight forward bias exists that grows with energy above 15 MeV [44]). The direction is important for identifying solar neutrinos, as well as for background reduction (such as eliminating radioactivity events).

The direction reconstruction is also copied from the SK solar neutrino analysis [31]. Only hit PMTs with timing residuals within 30 ns are considered when determining the direction. Starting at the already reconstructed vertex, many direction vectors are considered, and the angle between each direction vector and the hit PMTs is compared to an angular likelihood function extracted from MC. This likelihood function broadly peaks around 42 degrees, which is the Cherenkov angle of an ultra-relativistic particle in pure water. The contribution of each hit to the total likelihood is a combination of the angular likelihood value and a factor that corrects for the varying quantum efficiency of the PMT due to the incidence angle. The direction that returns the maximum likelihood is the final reconstructed direction.

As with most reconstructed quantities, the directional resolution improves with event energy, although the increased hit statistics of a higher energy event is offset by the increased likelihood of multiple Coulomb scattering, which is the limiting factor in the direction resolution; a 16 MeV event in SK-I has an angular resolution of around 22 degrees. In SK-II the lower photo-cathode coverage reduced angular resolution by about 10% compared to SK-I; in SK-III the likelihood function was modified by tuning it to be a function of the total event energy, allowing an improvement in angular resolution over SK-I by about 10%.

4.4 Muon Fitting

Muons in the detector were fit using software called Muboy; these muon fits were used for the spallation cut, and are critical to the analysis. Muboy is described in detail in [45, 46].

The Muboy algorithm starts with PMT selection. ID tubes are required to pass a charge threshold to be considered by Muboy; the cut is dependent on the number of hit ID tubes. For less than 8000 hit tubes, the charge threshold is 2 p.e.; from 8000

to 10,000 tubes it is 2.5 p.e.; and it is 3 p.e. for more than 10,000 hit tubes.

Next, Muboy takes the center tube of the patch of nine tubes with the highest total charge as a first guess for a likely exit point for the muon. Typically, the exit point of a through-going muon is the region of highest charge in the event, as the Cherenkov light emitted from each point on the track is directed into progressively smaller rings (or conic sections) centered on the exit position.

Thirdly, Muboy introduces another selection criteria for which hit PMTs are considered by counting the number of nearest neighbor hit PMTs within 10 ns for each hit PMT. If the number of nearest neighbor hit PMTs within 10 ns is below a certain threshold, the tube is disregarded. This threshold depends on the number of tubes left after the charge threshold cut, and goes between 1 (< 500 hit tubes left) and 5 (> 7500 tubes remaining).

The first guess of an entry position is the earliest time hit PMT with at least 3 hit neighbors within 10 ns. If no such PMT exists the number of required nearest neighbors within 10 ns is relaxed until a PMT is found. An entry and exit position gives an initial guess of the track.

Causality arguments are used to gain further information. For a single through-going muon, if the entry position is known, then it is physically impossible for light from the same muon to strike a PMT if not enough time has passed for an object traveling at velocity c to traverse the distance to the PMT from the entry position. Any such hit PMT is either a noise hit, or many may be an indication of a multiple muon event (where many muons from the same parent interaction all are traveling parallel and enter the detector simultaneously).

Muboy is unique among the muon fitters available at SK as it not only fits simple single through-going muons with a single entry and exit position, but actually looks for different types of muon events as it fits, and categorizes the event accordingly. Muboy will categorize each event as being one of the following: single through-going muon

($\sim 82\%$ of events), stopping muons (muon enters from outside but stops in detector, usually decaying into electron $\sim 7\%$), multiple muon bundles (found two different ways, described later $\sim 7\%$), and so called ‘corner clippers’ (where the track length is very short, $\sim 4\%$). There are a small fraction of events that Muboy completely fails to fit as well.

If Muboy finds more than 45 hit tubes (after previously described charge threshold and nearest neighbor timing cuts) that have a PMT time such that to traverse the distance to the PMT from the entrance position would require traveling at more than 33 cm/ns, then the event is tagged as a multiple muon (type 1). For other events, PMT hits that would require travel of more than 34 cm/ns (early time) or less than 18 cm/ns (late time) hits are rejected as noise. For those tagged as multiple muons (type 1) this requirement is tightened to only keeping hit PMTs where the times indicate direct travel from the entrance position would mean a travel speed of between 19.5 cm/ns and 32 cm/ns. Muboy determines final tracks by maximizing a goodness. The information used in this goodness include the fraction of hits inside the Cherenkov cone, and the timing residuals of the tubes. The full form can be found in [46].

The goodness is maximized by fixing the entrance position and moving the exit position on a grid. For events that are not thought to be multiple muons, a second iteration allows the entrance time to change slightly; a third iteration allows the Cherenkov angle to change slightly. If, after this new goodness maximization, the number of early time hits has risen above 35, the event is classified as multiple muon (type 2).

For non-multiple muon type events, the event is then checked to see if it qualifies as a corner clipper. If the event is near the top of the detector, the direction is checked; if near the bottom, the track length is checked (< 3 m indicates a corner clipper). Corner clipper muons were not found to cause any measurable amount of

spallation.

The remaining events are checked to see if they stop in the inner detector. If the amount of charge in the patch of events surrounding the exit position by 2 m is abnormally small (< 300 p.e. if no OD data exists; otherwise combinations of OD and ID tubes are tested) then the event is classified as a stopping muon, and the stopping position is guessed by looking for a fall off in the dE/dx information.

Events that have made it this far without being classified as anything else are determined to be single through-going muons.

If the event was classified as a multiple muon, then the fit track has all the correlated hits removed, and another fit is performed on the remaining hit tubes. The full procedure is actually a bit more complicated and can be seen at [46]. If another reasonable fit is found, the procedure is repeated. Up to 10 tracks can be fit; or, in some cases, only 1 track is ever fit, even though the event is considered a multiple muon.

All events have a quality of fit goodness number calculated. For multiple muon type events, a quality of fit goodness is calculated for each track, and are typically increasingly poor for each additional track. In general, fit tracks above the second or third are not very trustworthy.

Studies were carried out to determine Muboy accuracy. Taking a sample of about 2000 muons, the events were fit with Muboy and also scanned by eye. Out of 1728 events judged by Muboy to be single through-going muons, only 9 were thought to be something else by eye scan. Of 74 events Muboy judged as corner clippers, one was a stopping muon by eye scan. Of 129 thought by Muboy to be multiple muon events, 17 were thought to be through-going by eye scan; of 113 found by Muboy to be stopping muons, almost a third were considered through-going by eye scan, leading to the largest discrepancy. Overall, the agreement was very good.

Resolutions studies found that the entry point resolution was around 100 cm for

all muon types, excluding multiple muons with more than 3 tracks. The direction resolution in all cases was around 6 degrees.

All in all, Muboy is ideal as it can fit a muon more quickly than the precision muon fitters available to SK, but still fits the track well. Furthermore, its ability to categorize muons is highly valuable for determining spallation.

4.5 Multiple Coulomb Scattering Estimation

Electrons and positrons traveling in the detector multiple Coulomb scatter more as their energy increases. A measure of the amount of multiple scattering is especially important for increasing the efficiency of cutting solar neutrino events, as the amount of multiple scattering is correlated to how much the direction of the event is changed from the solar direction.

Multiple Coulomb scattering is estimated by software that utilizes a Hough transform to each event to calculate a goodness. Specifically, for each of a pair of two hit PMTs, a cone (with opening angle equal to the Cherenkov angle) is constructed, starting at the reconstructed vertex position, and pointed directly at the PMT. These two cones should intersect, usually in two places. The unit vectors from the reconstructed event vertex to these cone intersection points are recorded. They won't line up exactly. The goodness is the vector sum of all these unit vectors divided by the longest possible path (all vectors exactly aligned). The higher the goodness value, the less multiple scattering should have occurred. This theory is born out by MC studies; plots can be seen in the discussion of solar neutrino background (Fig. 6.6).

4.6 Cherenkov Angle Reconstruction

Reconstructing the opening angle of the Cherenkov cone of events is especially important for the DSNB analysis. This is accomplished by use of 'three hit combinations'

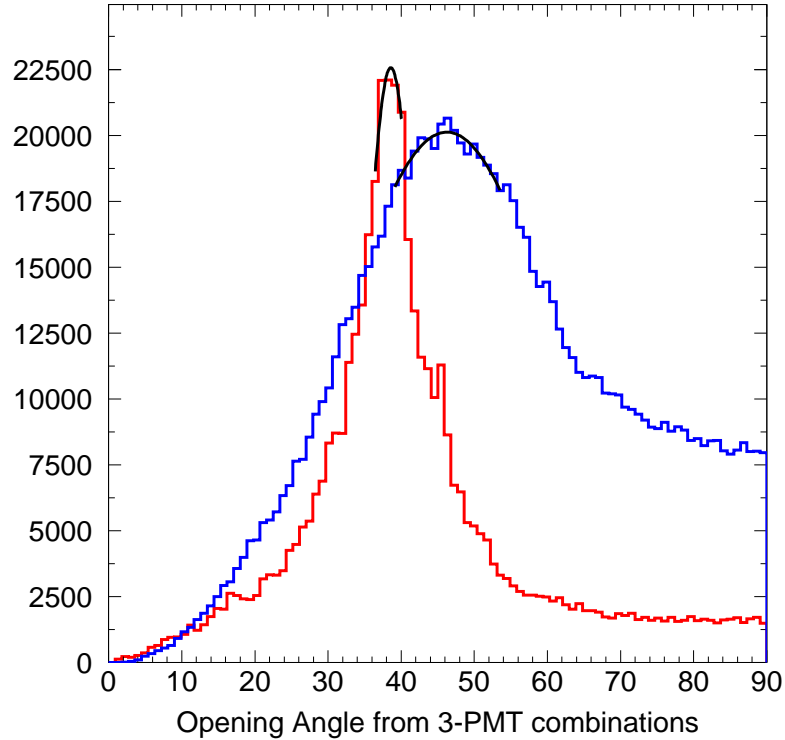


Figure 4.1: Example of distributions of 3-hit combinations used for calculating the Cherenkov angle. The Cherenkov angle (in degrees) is determined by a fit to the peak (shown). Electron-like events have a broader distribution than pion-like events. One of each type is shown.

or ‘triplets’. Every combination of three different hit PMTs in an event can be used to form a cone with a particular opening angle. A distribution is made of the opening angle formed by each three hit combination (see Fig. 4.1). The peak of this distribution is used as the Cherenkov angle of the event. The width of this distribution can help differentiate pions from electrons and positrons, as well.

4.7 dE/dx reconstruction

For muons, it can be useful to know not just the total amount of light deposited in the detector from the event, but also the emission profile along the track. To determine this dE/dx information, the amount of light seen by each PMT was assigned a location along the muon track it probably originated from. This emission point was determined

using timing information. First, Muboy reconstructs the time and place the muon entered the detector. We also have the very precise timing information of each PMT. By assuming the muon is traveling with a velocity c , and that the Cherenkov photon is traveling at a velocity c/n (with n being the index of refraction of pure water), I determine where along the muon track the light originated in order to satisfy all the timing requirements. The equation is as follows:

$$\frac{c^2(t-t_0)^2}{n^2} - r^2 + 2\left[\vec{r} \cdot \hat{\mu} - \frac{c(t-t_0)}{n^2}\right]X + \left[\frac{1}{n^2} - 1\right]X^2 = 0 \quad (4.3)$$

Where t_0 is the time the muon entered the detector, as fit by Muboy; t is the PMT time; \vec{r} is the vector from the muon entry point to the hit PMT; $\hat{\mu}$ is the muon direction (as reconstructed by Muboy); and X stands for $c(t_e - t_0)$, with t_e being the emission time of the Cherenkov photon from the muon track, which is the quantity we need to solve for. As a quadratic equation is involved, there are two possible solutions; if neither is unphysical, both are kept.

The information from all PMTs can then be combined into a dE/dx profile. The amount of light seen by a PMT may be different than the amount of light actually emitted, and therefore water transparency and PMT coverage effects (light traveling in certain directions from a particular point may be more or less likely to be seen by a PMT on average due to the geometric PMT coverage in that direction and the incidence angle the photon would strike those PMTs) are corrected for. An example of a resultant dE/dx profile can be seen in Fig. 4.2.

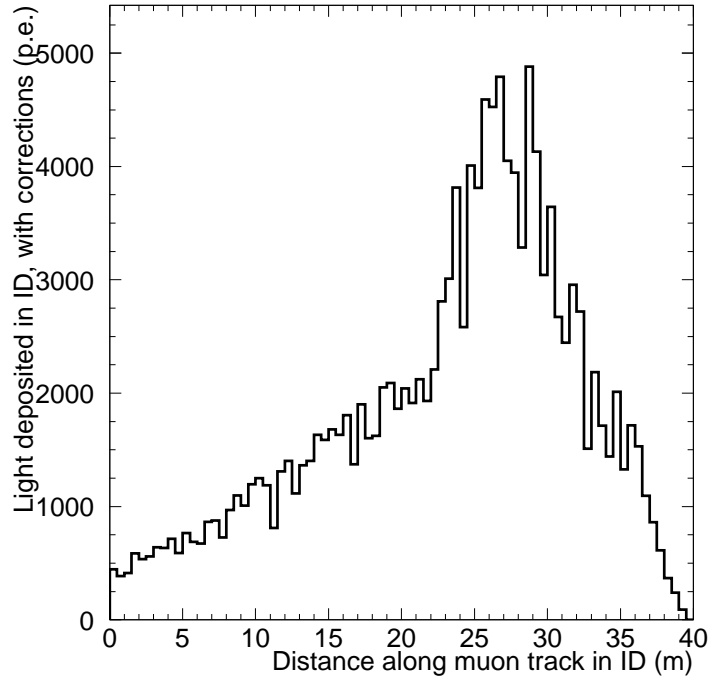


Figure 4.2: Example dE/dx distribution for a typical muon.

4.8 Alternate Muon Fitting

In rare cases, Muboy will have trouble correctly fitting the muon. This is indicated by a poor goodness value being returned by the fit. There are enough single muons that this can be a problem, as the fit is used to search for spallation. If a muon causes spallation, the spallation product should be close in space and time to the muon track. If the track is incorrectly fit, the track may mistakenly seem far away from the spallation product, possibly causing important spallation events to not be rejected by our spallation cut.

To help deal with this problem, an alternate muon fitter was developed for the rare cases when Muboy was unreliable. This fitter was quite crude and slow, and simply projected a grid onto the inner surface of the detector. Many possible combination of muon entry and exit points were then tested (the single muon case was assumed). This slow method was termed the Brute Force Fitter (BFF). To improve

computation speed, the total charge in the surrounding PMTs within 2 m of the exit position was required to be at least 70 photo-electrons, and the total charge of the PMTs within 2 m of the entry position was also required to exceed a threshold, as described in Table 4.1. For each combination of entry and exit point, a goodness was calculated; the combination that maximized the goodness was then used as the fit, and the goodness value itself was recorded as an indication of quality of fit. The goodness used is defined as follows:

$$G = \frac{N_{all}}{N_{cone}} \times \sum_{i=1}^{n_{hits}} e^{-\frac{t_i^2}{2\sigma_i^2}} \quad (4.4)$$

where n_{hits} is the number of hit PMTs with a time residual within +/- 100 ns of zero; t is the timing residual of the PMT; σ is the time resolution of PMT i (and is a function of charge); N_{all} is the total number of hits above the charge threshold; and N_{cone} is the number of hits above charge threshold inside the Cherenkov cone for the considered fit. In order to calculate timing residuals and the location of the Cherenkov cone, a Cherenkov angle of 42 degrees was assumed. The PMT charge threshold is a function of the total charge Q_{total} :

$$Q_{thresh} = C \times \frac{Q_{total}}{1000} + 1 \quad (4.5)$$

where C is 1.6 if $Q_{total} \leq 50,000$ and 1.8 for $Q_{total} > 50,000$.

The BFF was able to correctly refit about 75% of the muons Muboy had trouble with (Muboy goodness < 0.4).

Table 4.1: Charge requirement of total number of photo-electrons seen by PMTs within 2 m of the considered entry position, as a function of total light seen in the event.

Event total light (p.e.)	Entry position threshold (p.e.)
$\leq 100,000$	12
$> 100,000$	20
$> 250,000$	26
$> 400,000$	33

Chapter 5

Modeling

5.1 The Monte Carlo

Backgrounds were modeled using SKDETSIM, which is the official SK MC, using GEANT 3.21 for particle tracking and NEUT [47] to model neutrino interactions (mostly inside the nucleus). Hadronic interactions are simulated using a combination of CALOR and custom SK code ([48, 49]). The SKDETSIM MC has been well tested and verified at most energies. Rayleigh and Mie scattering and absorption are considered, as is the varying transparency of the water.

For tuning the solar neutrino cut, we made use of the detailed and well studied solar neutrino MC which already exists for the SK solar analysis, and models 8B and *hep* neutrinos [31].

The physics occurring in NEUT is tracked by a code, which is especially useful for understanding the complicated NC background. Particles created in NEUT (not GEANT) are each listed, as is their created position and momentum, which allows us to track the MC in detail.

5.2 Atmospheric Neutrino Backgrounds

The main remaining backgrounds left in the analysis after all of the cuts are applied are from atmospheric neutrino interactions. Carefully modeling these remaining backgrounds are critical to accurately understanding the final sample. To achieve this, 500 years of MC was used for each SK experimental phase, and the entire analysis reduction was applied. A recent effort, largely due to this analysis, has been made at SK to check and revise the MC at the lowest energies, as a few bugs were found. This has led to new, corrected MC with revised cross sections for certain processes (especially NC processes). The MC used here for SK-I/II/III does not have these corrections applied. Instead we had to take careful steps to prevent the bugs from harming the analysis. We believe the resulting MC is mostly correct, and that any inaccuracies are within our highly conservative systematic errors.

The first bug noted was that 15.1 MeV gamma rays appeared in elastic scattering interactions far more frequently than they should. This was traced to a typo in branching ratios causing these events to appear orders of magnitude more often than was appropriate. In order to prevent this from affecting the analysis, all 15.1 MeV gamma events were suppressed. Although this also removes any few 15.1 MeV gamma events that should be in the sample, these are estimated to be quite few, and we believe this small issue is well covered by the highly conservative systematics.

The types of events seen can be sorted into 3 categories:

- 1) ν_e **CC events**. Atmospheric $\bar{\nu}_e$'s are indistinguishable from DSNB $\bar{\nu}_e$'s on an individual basis, but have a very different energy spectrum. Atmospheric ν_e 's can in principle be distinguished from DSNB $\bar{\nu}_e$'s, but SK cannot distinguish between electron and positron events. Sometimes ν_e events can emit low energy pre-activity gammas, which, if detected, allows the event to be rejected; in practice, however, only a small portion of events can be caught with this method. For simplicity, both the $\bar{\nu}_e$ and ν_e CC events are combined under the label ' ν_e CC'.

2) ν_μ **CC events**. This is the largest remaining background in the sample. Atmospheric ν_μ 's and $\bar{\nu}_\mu$'s interact in the water of the detector and create a muon via a charged current (CC) reaction. This muon can be very low energy, often below Cherenkov threshold, in which case its decay electron cannot be removed like other decay electrons (by correlation to the preceding muon), since the muon is invisible. This background's energy spectrum is the well known Michel spectrum, slightly modified by resolution effects, and is quite different from the SN relic spectrum.

Furthermore, the muons themselves that are created, when low energy, can be mistaken for positrons. Most of these events are cut in our event reduction, especially through Cherenkov angle considerations. A few, however, survive in our final sample in our signal region.

When a sub-Cherenkov muon is created, a low energy (around 6 MeV) prompt gamma can be created. Seeing this gamma and correlating it to the decay electron allows reduction of this background. The new SK-IV electronics, as well as proposed improvements that could allow further lowering of the SK energy threshold, may allow improved effectiveness of detecting this pre-activity. Again, both the ν_μ and $\bar{\nu}_\mu$ signals are combined as ' ν_μ CC'.

3) **NC events**. This category is especially complicated, and can be subdivided as follows (with spectral plots for each subdivision available in Appendix C), where the percentages listed represent the proportion of events in the MC sample after cuts:

a) Pion absorption (36%): These events were mistakenly high in energy in the MC, reconstructing at energies > 16 MeV and therefore entering the final sample. An independent study ¹ concluded that this was due to outdated code, and was not correct; $>99\%$ of pion absorption events in our MC should instead result in a gamma ray of < 7.6 MeV, which cannot reconstruct > 16 MeV. Therefore events from this mode were neglected.

¹Private communication with M. Sakuda

b) NC elastic scattering (25%): Neutral current (NC) elastic events (meaning elastic scattering on a nucleon, which then becomes excited, and can give off de-excitation gammas, or cause other nuclear reactions) have an energy spectrum that rises sharply at our lower energy bound, similar to SN relics. Most are removed by Cherenkov angle reconstruction, but some still leak into our final sample and must be modeled. With the lowering of the energy threshold from 18 MeV to 16 MeV, this background has become especially relevant.

c) Single π^- events (all energies), and single π^+ events (> 200 MeV/C only) (19%): The pion events >200 MeV mostly deposit energy in the detector through Cherenkov radiation from the accelerated pion. As the energy reconstruction assumes these are electrons, the reconstructed energy varies largely and is roughly flat. π^- events below 200 MeV generally capture on an oxygen, leading to an excited nucleus which gives off de-excitation gammas.

d) Single π^+ events < 200 MeV/C (7%): Lower energy π^+ events cannot capture on an oxygen like their negatively charged counterparts, as their charge is wrong. However they are less relativistic, create less Cherenkov light, and decay faster, generally into a muon, which then decays into an electron, giving these events a Michel spectrum.

e) Single unabsorbed π^0 events (7%): The spectrum of these single particle events fall slowly as energy increases.

f) Multiple pion production (5%): The spectrum is roughly flat in energy.

g) Other (for instance, deep inelastic scattering) ($<1\%$): So few events we neglect.

Of all these modes, the NC elastic is the most important. This is because of the sharp spectrum increase at low energy, similar to the behavior of real relic events, as well as the large amounts of them. Also important is c), as there are quite a few of these events.

Treating each of these modes as a separate channel to model is prohibitively difficult, both in terms of manpower and computing power, and is unnecessary. Mode a) is neglected; b) must be modeled; and c) is important. Modes d), e) and f) not only have a small number of events, and relatively flat spectra that won't greatly change our results, but furthermore it was discovered that the spectrum of each of these modes can be well described as a linear combination of the spectra of modes we do consider. In other words, if we consider ν_e CC events, ν_μ CC events, NC elastic events, and single π^- events with single π^+ events > 200 MeV/C, then when we perform our maximum likelihood search on our final sample in an attempt to fit the data to these spectra, modes d), e), and f) will be absorbed into the other modes in the fit. This means we don't have to worry about them.

Also, both the charged pions (mode c) and the muons from ν_μ CC events that are confused as positrons have Cherenkov angle distributions that tend to be smaller than relics. They are also both quite a bit less important than the other modes. To simplify the analysis, it was deemed prudent to merge these two categories into one channel, referred to as ' μ/π '.

Thus, the remaining atmospheric backgrounds are grouped into four categories:

1) **Atmospheric ν_μ CC events.** Specifically, decay electrons from sub-Cherenkov muons. This background was considered in the 2003 study.

2) **ν_e CC events.** This background was considered in the 2003 study.

3) **Atmospheric ν NC elastic events.** This background was not considered in the 2003 study.

4) **Heavy particle production from atmospheric ν events, or μ/π .** This last category is a grouping of two different things, both heavier particles. First, NC reactions produce charged pions (only π^+ events > 200 MeV/C are included here), some of which survive the pion cut. Included with them, since the spectrum and Cherenkov angle distribution are relatively similar, are surviving muons (from

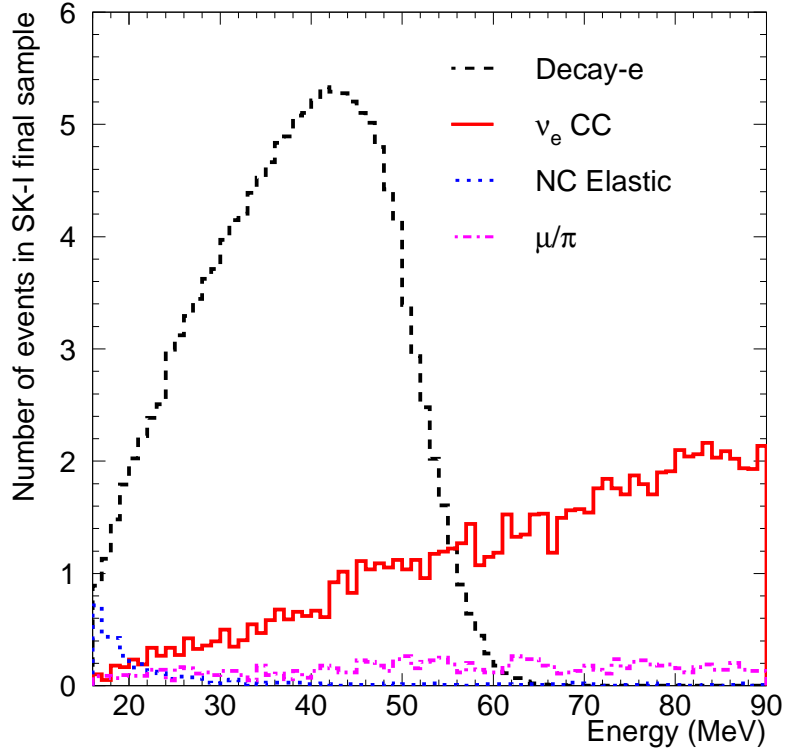


Figure 5.1: Spectra of the four remaining backgrounds.

muon neutrino interactions) above Cherenkov threshold. This background was not considered in the 2003 study.

The background spectra of the four backgrounds are shown in Fig. 5.1. Another important handle is their Cherenkov angle distributions, which are shown in Fig. 7.1.

5.3 DSNB Modeling

MC was made for the following DSNB models: Malaney’s cosmic gas infall model [14]; Woosley and Hartmann’s chemical evolution model [13]; Kaplinghat et al.’s heavy metal abundance model [16]; Ando et al.’s LMA model [17] [NNN05 ref]; Lunardini’s failed supernova model [15]; and many cases of the formulation by Horiuchi et al. [19] (see Chapter 9), of which the 6 MeV case is featured. Although many more excellent models exist, I have worked towards a new, model independent method of presenting our results (Chapter 9), and therefore did not feel it was necessary to perform a

comprehensive survey of all existing models.

The MC was created using SKDETSIM, with the energy spectrum of the events matched to the energy spectrum of the particular model, from 10 to 90 MeV. MC was simulated for each model, for SK-I, SK-II, and SK-III separately, and events were assumed to occur uniformly in the detector, up to a distance of 50 cm from the PMTs (a comfortably larger volume than the fiducial volume, which discards all events up to 2 m from the PMTs).

Chapter 6

Analysis: Event Reduction

There are many types of events in the SK data set, many of which are backgrounds to the SN relic analysis. Each PMT fires thousands of times a second due to dark noise fluctuations; cosmic ray muons enter the detector at a rate of approximately 2 Hz, lighting up the detector and often breaking apart oxygen nuclei (spallation), resulting in radioactive isotopes; radioactivity in the rock walls or PMT glass itself can cause events, and more. From this enormous rate of data it is our job to search for a signal that we expect to see only a few times a year. The first step in this difficult task is to filter out as best we can anything that is probably not a supernova relic neutrino event, followed by the second task of understanding everything that is left. This chapter describes the series of cuts that were implemented in order to generate our final data samples.

6.1 First Reduction

The first reduction is a series of loose cuts that eliminates noise, muons, calibration events, and other things that are clearly not SN relics. It is the first set of cuts applied, and greatly reduces the data volume, giving us an easily manageable sample to study. Events that survive the first reduction we consider to be ‘relic candidates’,

although most if not all will be further background events. These cuts are largely the same for the relic analysis as they are for the long established SK solar analysis, from whence the name ‘first reduction’ carries over. With the exception of the fiducial volume cut, the first reduction is estimated to be more than 99% efficient. The first reduction is comprised of the following cut criteria:

OD triggered events

We search for SN relic events that are fully contained inside the ID. If both the ID and OD have triggered it generally means that a charged particle has entered the detector from the outside, depositing light in the OD along the way. These events in general will not be SN relics, as the incoming neutrino has no charge, and the positron resulting from the inverse beta decay reaction only travels a short distance (10 - 20 cm). Thus, any event with an OD trigger is removed from the sample.

Charge cut

One basic variable is the total light deposited in the detector. In general, cosmic ray muons create much more light in the detector than a SN relic event would, as only high energy muons can penetrate the rock overburden. Although most muons are caught by the OD cut, some may escape it, and fully contained muon events (where an atmospheric muon neutrino creates a muon in the ID) are possible. A simple charge cut will eliminate most of them (Fig. 6.1).

In SK-I and SK-III, events with more than 2,000 p.e., or that cause more than 800 PMTs to see light within the event, are eliminated from the data sample. For SK-II, the criteria is halved, due to the reduction of PMT coverage by approximately a factor of 2.

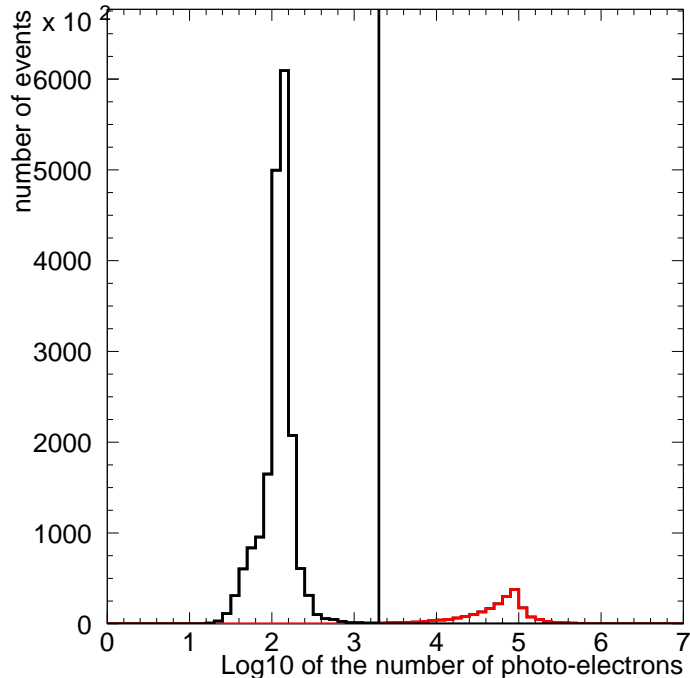


Figure 6.1: Photo-electron distribution of amount of light deposited in the detector by events in SK for over a 24 hour period. The line is at 2000 p.e.; the red histogram to the right of the line shows the distribution of rejected events that are mostly muons.

Fiducial volume

The entire ID volume is not used. First, there is an excess of low energy events near the boundary of the ID, due largely to radioactive events (some from the PMT glass itself, or their shielding installed after SK-I). Secondly, our reconstruction tools, especially the energy reconstruction, begin to fail near the ID boundary. By removing the outer 2 m of the ID, we eliminate almost all of this extra background, and restrict ourselves to the volume in which our tools work well. The ID contains 32.5 ktons of water; when we remove the volume within 2 meters of any wall, we are left with the FV, which contains 22.5 ktons. Only events in the FV are used in the DSNB analysis.

50 μs cut

Events close in time can be evidence for background. For instance, after a high energy muon, electronic noise and pulse reflections may cause the illusion of another event shortly afterwards. Also, many muons stop in the detector (~ 0.15 Hz) and decay into electrons which can mimic the relic signal. The muon lifetime is $2.2 \mu\text{s}$, although in water, it is not the same for positive and negative muons due to the possibility of μ^- capture, and averages to about $2.08 \mu\text{s}$. Since a real SN relic event should not have any correlation with any other event occurring in the detector, we can eliminate electronic noise and decay electrons by rejecting all events for a short time after every event (LE trigger or higher). $50 \mu\text{s}$ is used, which adds an almost negligible amount of inefficiency as the LE rate is less than 20 Hz.

Calibration events

Calibrations occur periodically even during normal data taking. These are tagged as calibration events and are removed from the relic sample.

Noise cut

With a dark noise rate of several kHz in the PMTs, sometimes accidental coincidence can conspire to cause enough tubes to fire inside a 200 ns window to trigger the detector. For events such as these, most of the tubes channels will record very little charge. If the fraction of PMTs that see less than 0.5 p.e.'s in an event is more than 40%, then the event is cut. Also, sometimes noise in an ATM board itself will cause all the channels on the board to fire simultaneously; thus, if an event contains an ATM board where more than 95% of the channels counted a hit, which should not normally happen for low energy events like a relic, then the event is removed.

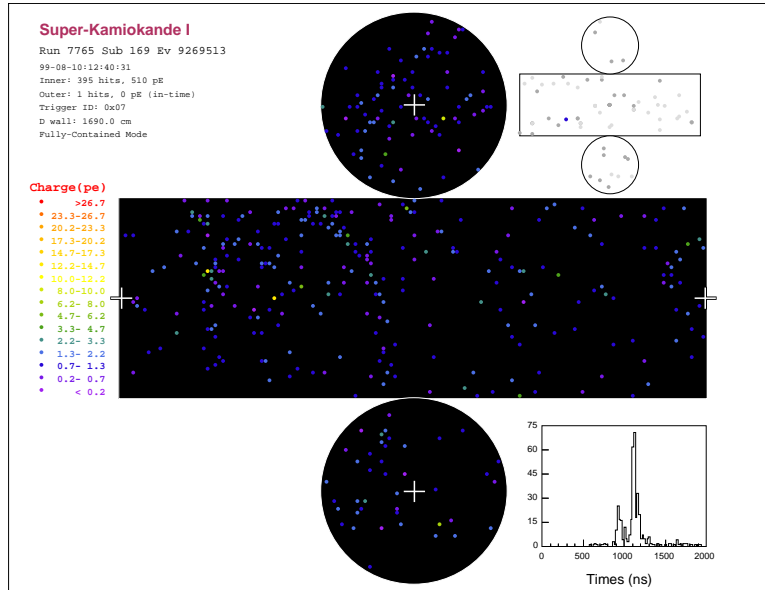


Figure 6.2: Example event in SK-I that exhibits a double timing peak structure, visible in the timing plot in the lower right of the display.

6.2 2-peak cut

Although most decay electrons are eliminated by the $50 \mu\text{s}$ cut, occasionally it occurs that the muon decays quickly enough that both the muon and the decay electron information are captured in the same $1.3 \mu\text{s}$ timing window that comprises a single event. In these cases, the timing information for that event will have a double peak structure [see Fig. 6.2]. Other, even rarer events can cause multiple peaks as well.

In order to find and reject such events, the timing information of the event was searched for any indication of a peak outside the main timing peak. The algorithm uses the BONSAI (see section 4.1) fit time to determine the probable timing location of the main timing peak. Any hits with time of flight subtracted times earlier than 12 ns before the BONSAI event time is considered possible pre-activity; any time after 20 ns after the BONSAI event time is considered post activity.

Each hit is assigned a goodness, which is a sum of all other hits within 25 ns, each weighted by a Gaussian $e^{(-t/2)^2}$, where t is the time difference between the hits, divided by a characteristic time of 5 ns. This goodness is used to noise filter the hits;

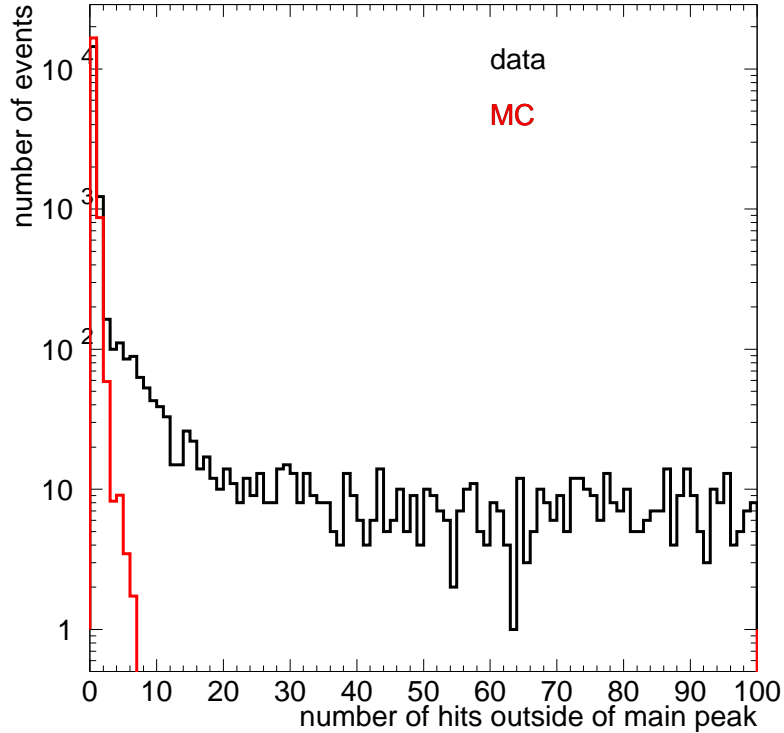


Figure 6.3: Distribution of maximum number of grouped hits outside the main timing peak, for the SK-I/III data sample (no cuts except first reduction), compared to SN relic MC.

all hits are required to be above a certain goodness to be considered. In most cases this goodness threshold is 4, but an exponentially decaying signal of late time hits are assumed (from multiple Coulomb scattering), increasing the required goodness threshold for hits at the beginning of the post-activity region.

Each of the 3 regions (pre-activity, main, and post-activity) then have the remaining hits (that pass the goodness threshold cut) searched in a sliding 15 ns window. If the maximum number of hits found in a 15 ns time window in either the pre or post-activity region is five or more, the event is rejected.

This cut is estimated to have a signal inefficiency of $< 0.02\%$, as estimated by MC.

6.3 Incoming Event Cut

Physics events that are incoming into the detector from the outside or the walls (such as radioactivity from the PMT glass itself) can be a background. Although the FV cut eliminates most of these types of events, some travel farther than 2 meters. Rather than tightening the FV cut, which causes significant inefficiency, we can use the reconstructed direction of the event. An effective distance parameter d_{eff} is used, which is defined in the same way as the SK solar neutrino analysis [31] (where it is called the ‘Gamma ray cut’), by projecting the event back opposite its reconstructed direction until we hit the wall of the ID. That distance (the distance ‘traveled’ in the detector) is the d_{eff} variable.

An artifact of the vertex fitting method also causes many misreconstructed events to have low d_{eff} , which are eliminated by the same cut. This effect is not fully understood, and may even be a larger contribution to low d_{eff} events than the physics backgrounds, making this cut doubly important.

In all data periods, a 300 cm d_{eff} cut was applied at all energies. Due to higher amounts of background at low energy, however, additional cuts were required. In SK-I sufficient statistics (1497 days) existed to allow tuning of an energy dependent cut for the low energy region, maximizing efficiency (98% efficient; see Fig. 6.4). This energy dependent function is simply a linear cut off from 300 cm at 19 MeV to 450 cm at 16 MeV. In SK-II and SK-III, the cut needed to be reconsidered, as the addition of FRP shielding on the tubes added a new radioactive source, potentially increasing background. Also, the smaller cathode coverage in SK-II worsened the energy and vertex resolution compared to SK-I and SK-III. So, all three periods had to be considered separately, and due to the decreased statistics, an energy dependent cut was not possible for SK-II (794 days) or SK-III (562 days). Instead, a single d_{eff} cut was implemented for events less than 22 MeV, with a value of 450 cm for SK-III (96% efficient), and 500 cm for SK-II (95% efficient). No evidence of contamination

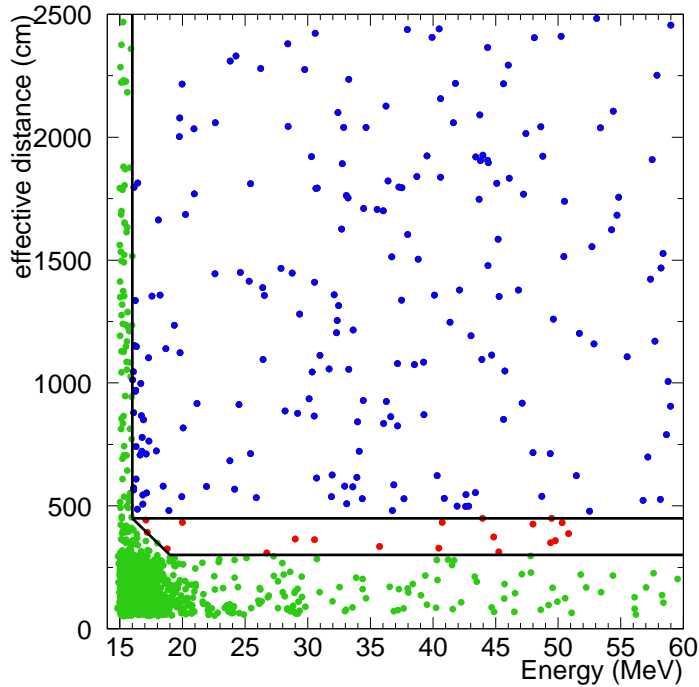


Figure 6.4: SK-I data distribution showing original published analysis d_{eff} cut value of 450 cm, and new value of 300 cm at most energies, with an energy dependent cut at low energy. The vertical axis is d_{eff} (cm) and the horizontal axis is reconstructed event candidate energy (MeV). The red dots represent events that would have been eliminated by the old cut. A line is drawn at 16 MeV to represent the current energy threshold; it should be recalled the 2003 published analysis used a threshold of 18 MeV instead.

remains after the cuts (Fig. 6.5).

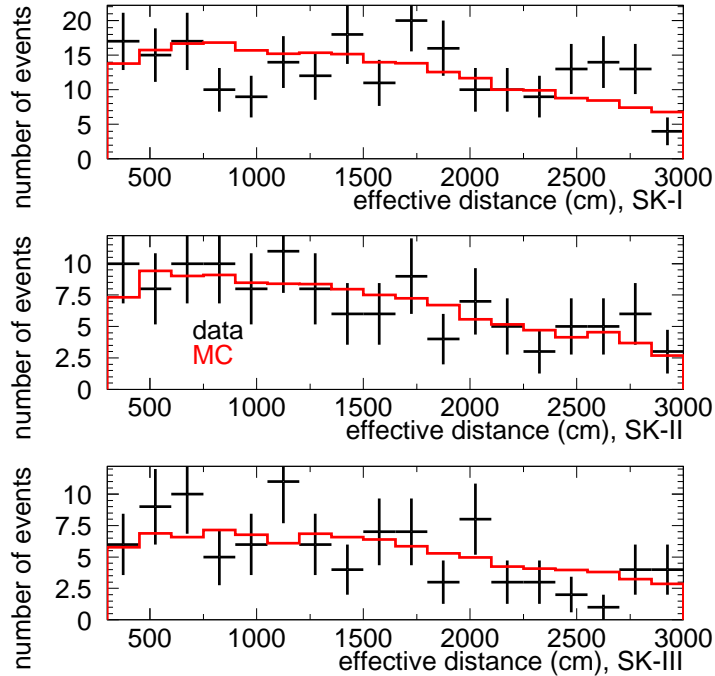


Figure 6.5: d_{eff} distribution of final data for all three data phases (black, all cuts applied) compared to SN relic MC (LMA model, red, scaled to data). No evidence of d_{eff} excess (expected in the first bin, if at all) is indicated.

6.4 Solar Cut

Solar neutrinos from the sun can elastically scatter in the detector, creating events that look like SN relics. In order to eliminate such events, we can use the angle between the reconstructed direction vector of the event and the direction vector from where the sun was in the sky at the time of the event. The cosine of this angle is used; a $\cos(\theta_{sun})$ of one means the event came from the solar direction.

Unfortunately, due to electron multiple Coulomb scattering leading to imperfectly reconstructed event directions, as well as up to 15 degree differences between the angle of the neutrino and the electron, solar neutrino events rarely have a $\cos(\theta_{sun})$ of exactly one. This distribution makes cutting solar events using $\cos(\theta_{sun})$ tricky, especially since solar neutrino flux increases sharply right at the critical lower energy

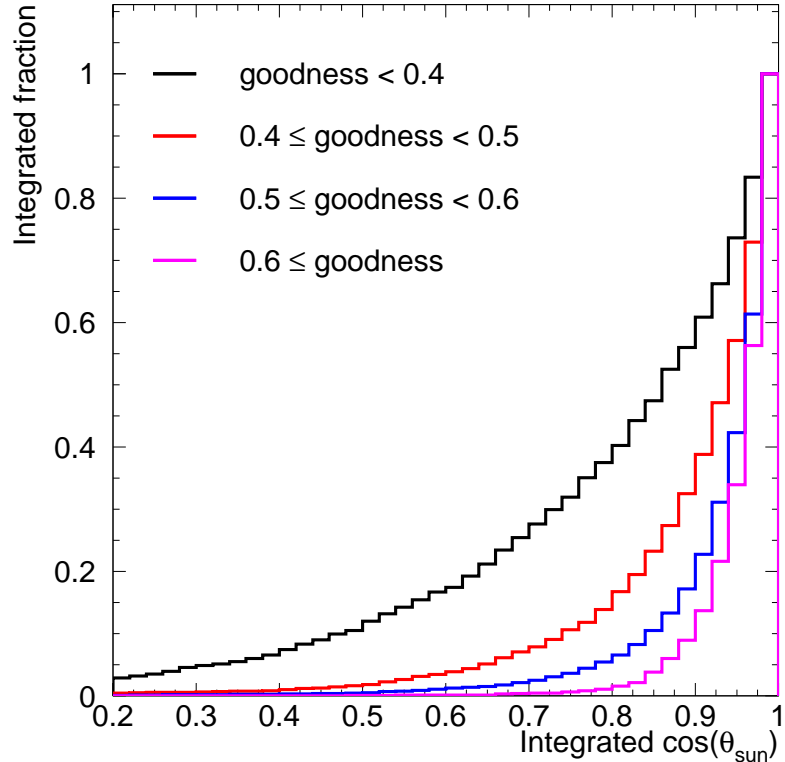


Figure 6.6: SK-I/III solar MC integrated $\cos(\theta_{\text{sun}})$ distributions by multiple Coulomb scattering goodness bin.

edge of our analysis, where any inefficiency hurts the most. In order to maximize our sensitivity, we used an energy dependent cut coupled with the multiple Coulomb scattering goodness (see section 4.5).

To quantitatively determine the best cut thresholds, the SN relic candidate sample was divided into four different multiple Coulomb scattering goodness bins (see Fig. 6.6), and a significance function was developed:

$$\text{Significance} = \epsilon / \sqrt{\kappa S + \epsilon \alpha} \quad (6.1)$$

where ϵ is the cut efficiency, S is the number of solar neutrino events, κ is the reduction effectiveness of the cut (such that $\kappa \times S$ is the number of solar neutrino events remaining after the cut is applied), and α represents the non-solar neutrino background.

The solar neutrino spectrum is modeled using the Monte Carlo developed for the SK solar analysis. The solar neutrino flux was normalized using real SK data below energy threshold (14-16 MeV), with all cuts applied (except the one on $\cos(\theta_{\text{sun}})$). To normalize, it was assumed that all events with $\cos(\theta_{\text{sun}}) < 0$ were not solar neutrino events, and that all non-solar remaining events had no $\cos(\theta_{\text{sun}})$ dependence (it is difficult to imagine a situation where this would not be true). Thus, simply subtracting the number of events with $\cos(\theta_{\text{sun}}) < 0$ from the number of events with $\cos(\theta_{\text{sun}}) > 0$ allows us to estimate the number of solar neutrino events at a particular energy, and then extrapolate the number of solar neutrino events at all energies.

The dominant non-solar neutrino background was assumed to be decay electrons from atmospheric ν_{μ} CC events, which is our largest background (see section 5.2). The spectrum was modeled using a sample of data that was identified as decay electrons by timing and spatial correlation to a preceding muon that had no OD trigger (muon from a fully contained atmospheric muon neutrino reaction). The normalization of the background was determined by fitting to the data (see Fig. 6.7).

As with many of the cuts, SK-I and SK-III used one cut, and a separate version of the cut was tuned for SK-II. The SK-II cut criteria is simply the SK-I/III cut with the energy bins shifted by +6% to reflect the poorer energy resolution. The cut is multiple Coulomb scattering goodness bin dependent for $E < 19$ MeV (SK-I/III, < 20.14 MeV SK-II), while for 19-20 MeV (20.14-21.2 MeV SK-II) there is a simple, multiple scattering goodness bin-independent cut that eliminates events with $\cos(\theta_{\text{sun}}) > 0.93$. More cut details can be found in Table 6.1. Note that the cut values in the table mean that events with $\cos(\theta_{\text{sun}}) > \text{cut value}$ are rejected. Also note that the inefficiencies are already weighted by the fraction of events in that MCS goodness bin, so that they can be simply added for the total.

After the cut, no statistically significant evidence for remaining solar neutrino events exists, and the estimated number of remaining solar neutrino events in the

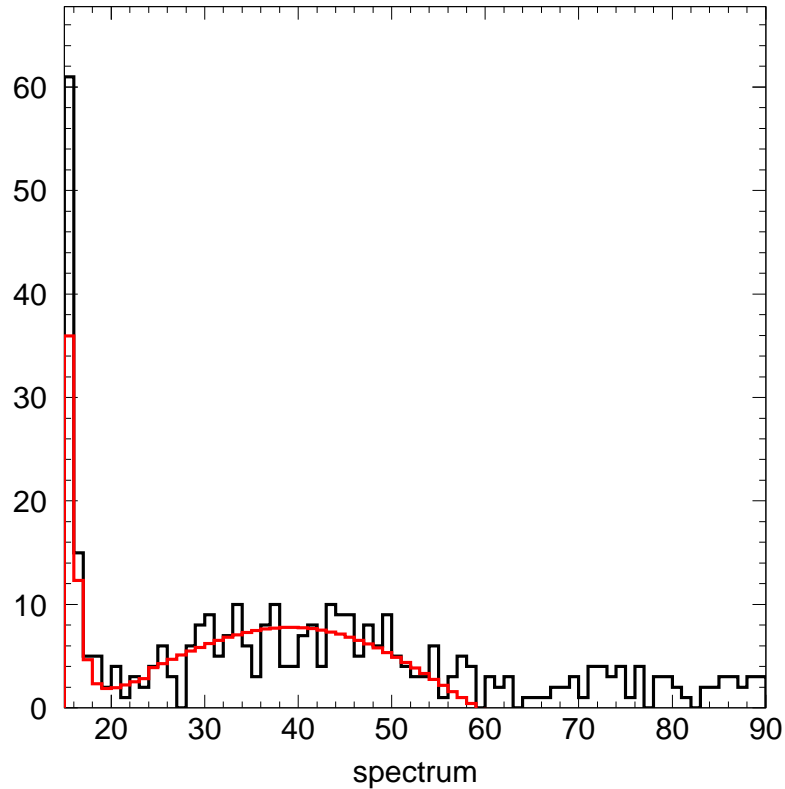


Figure 6.7: SK-I fit to data to determine amount of background. Horizontal axis is energy (MeV), vertical is number of events. Black is SK-I final data sample (without solar cut), red is estimated solar (from MC) + background (estimated to be mostly decay electrons from near-threshold fully contained muons). The 15-16 MeV bin is shown, which is not used in the final analysis due to the left over spallation.

combined SK-I/II/III final data sample is two or less.

Table 6.1: SK-I/III solar $\cos(\theta_{\text{sun}})$ cut value (inefficiency)

Goodness bin	16-17 MeV	17-18 MeV	18-19 MeV
$g < 0.4$	0.05 (7.2%)	0.35 (5.0%)	0.45 (4.3%)
$0.4 \leq g < 0.5$	0.39 (9.7%)	0.61 (6.4%)	0.77 (3.8%)
$0.5 \leq g < 0.6$	0.59 (6.7%)	0.73 (4.5%)	0.81 (3.2%)
$0.6 \leq g$	0.73 (2.4%)	0.79 (2.0%)	0.91 (1.0%)
Total	26.2%	17.9%	12.2%

6.5 Spallation Cut

Perhaps the most difficult reducible background to eliminate is spallation. Cosmic ray muons enter the detector at a rate of around 2 Hz, even with the rock overburden. These high energy muons can spall an oxygen nuclei, as well as cause other reactions resulting in radioactive isotopes which then decay in the detector, mimicking a relic signal.

The highest energy spallation product believed to be produced in the detector is ^{11}Li and ^{14}B , each with beta decay end point energies of up to 20.6 MeV. Because of energy resolution effects, these events can have a reconstructed energy up to 23 or even 24 MeV. Luckily, these events only have a half-life of around 0.01 seconds, so they are rather easy to associate with the muon which created them.

As we go lower in energy, however, the number of possible isotopes increases rapidly, as do their half-lives. Therefore spallation events become increasingly abundant and difficult to deal with as the energy threshold of our analysis is lowered. The original 2003 SK analysis had an energy threshold of 18 MeV total positron energy, and the spallation cut was 37% inefficient. For this thesis, after much work, this cut has been significantly improved. Now, for the same SK-I data as the published analysis, the energy threshold has been lowered to 16 MeV, and in the $E > 18$ MeV region, inefficiency has been lowered from 37% to around 9%.

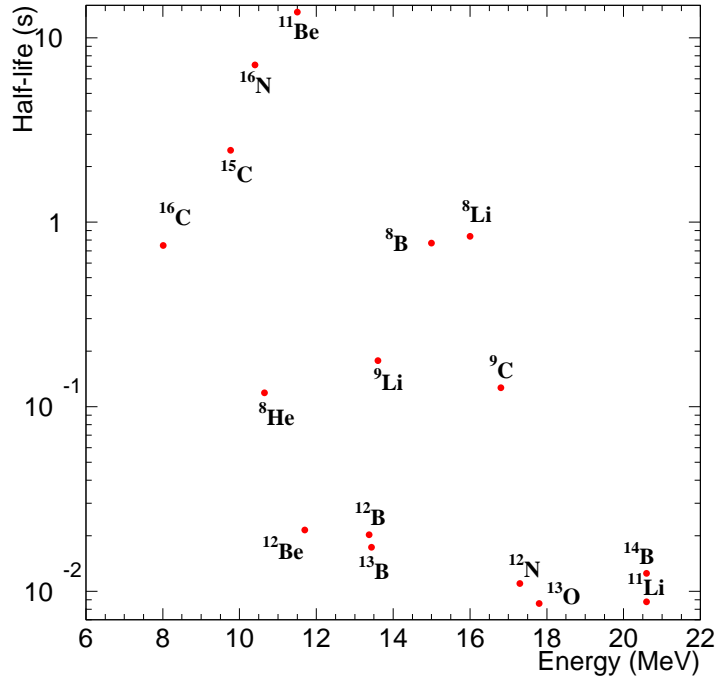


Figure 6.8: Scatterplot of spallation products expected to occur in SK, showing their half life and energy. Energy values are maximum possible; decays may often be lower in energy, and multiple modes may be involved. Data is listed in Table A.1.

6.5.1 Spallation Likelihood Variables

To eliminate spallation products, we correlate relic candidates to preceding muons. In the SK data, we have four main handles on spallation events.

The first, and most important, is simply the time difference of the relic candidate compared to that of the preceding muon, dt . Most spallation products have half-lives of less than 0.1 seconds (see Fig. 6.8), while the muon rate is about 2 Hz; thus any event with a muon preceding it by less than 0.1 seconds is quite likely to be spallation. Some spallation products have longer half-lives however. Some events with around 0.7 or 0.8 s half-lives have sufficient energy that energy resolution effects can cause a reconstructed energy above 16 MeV. If we try to lower the energy threshold below 16 MeV, we start to acquire events with even longer half-lives, from over a second, up to 13.8 s for ^{11}Be . The longer lived events are especially difficult to remove from

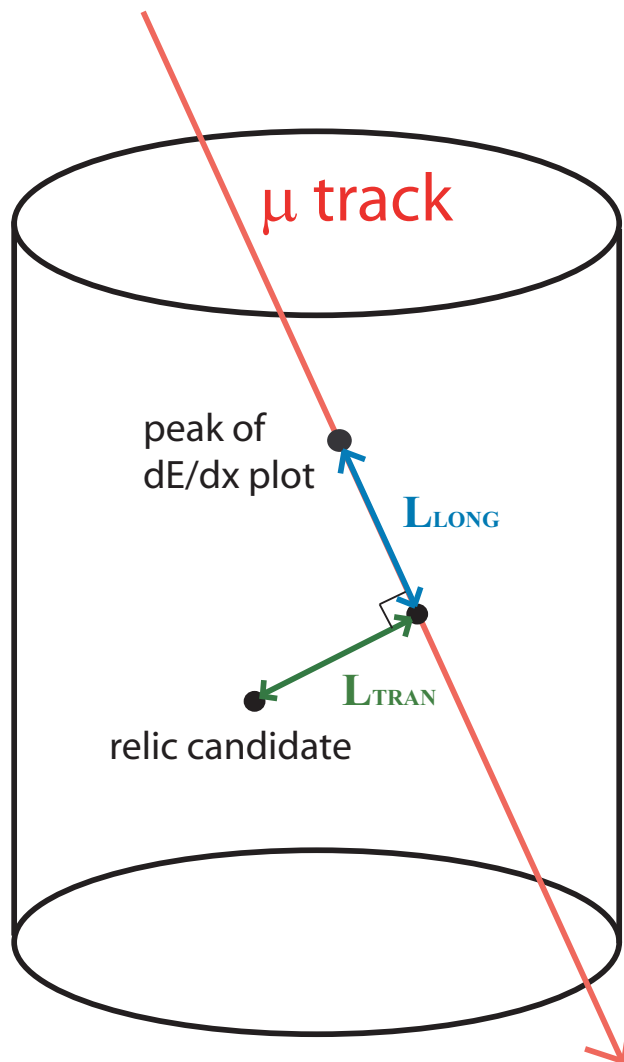


Figure 6.9: Schematic showing spallation distance variables.

our sample, and because of these events our energy threshold can be no lower than 16 MeV if we want to be able to remove all the spallation background.

The second most important variable used in determining spallation is the transverse distance (L_{TRANS}). This is defined as the perpendicular distance from the muon track to the reconstructed event vertex of the relic candidate (see Fig. 6.9). The vertex resolution of events 16-30 MeV tends to be around 30 or 40 cm. The resolution of the muon track is about a meter. The spallation product itself cannot travel far in the detector before decaying, especially for short lived events. For muons unassociated

with the relic candidate, accidental coincidence of L_{TRANS} less than a few meters is quite rare. Thus L_{TRANS} is a powerful handle on spallation, and a 16-20 MeV relic candidate with a preceding muon within a second of dt and a meter of L_{TRANS} is almost certainly a spallation product.

The third and fourth variables used for spallation determination come from the muon dE/dx plots described in section 4.7. Spallation causing muons tend to have a peak in their dE/dx plots at approximately where the spallation occurred. Thus, the distance from where the peak in the dE/dx plot occurs and where the relic candidate lies on the muon track is called the longitudinal distance, or L_{LONG} , and is used as our third variable. L_{LONG} is not as powerful of a correlation as L_{TRANS} , but is still useful. The longitudinal spallation tagging used was discovered and developed for this analysis. The underlying physics behind the utility of the dE/dx plot in predicting spallation longitudinally is not fully understood and may deserve further investigation. For the sake of this thesis, the correlation has been proven and is used without further questions.

The last variable used is the amount of light seen in the dE/dx plot in a width of 4.5 m centered on the peak. Very strong peaks, which show that lots of light was deposited in the detector originating from that region of the muon track, usually indicate spallation. This variable, Q_{PEAK} , is similar to a variable used in the spallation cut of the 2003 analysis, called the residual charge. The residual charge means the amount of light deposited in the detector above that expected by a minimum ionizing particle of the same track length. The Q_{PEAK} is like a local residual charge. Again, the power of Q_{PEAK} is not as great as that of dt and L_{TRANS} , but we still gain information by using it.

6.5.2 Method of Determining Spallation

All relic candidates are compared to preceding muons to check for the possibility of being spallation. The primary means of determining whether or not an event is spallation is by use of a likelihood method utilizing the four variables described in the previous section. The cut also includes a mix of cuts on specific quantities. The complete cut algorithm is described in Appendix A.3.

First, the data set is broken into relic candidates (events that have passed the first reduction) and muons (events that deposit more than 1000 p.e.'s in the detector). Then, the muons are fit and subdivided into the various Muboy categorizations (see section 4.4): single through-going, stopping, multiple, and corner clipper. If the fit is poor (Muboy goodness < 0.4) for single-through going type muons, a BFF fit (see section 4.8) is used instead (if the BFF goodness is < 0.3 , neither fit is trusted and all events are vetoed for 2 s. Even if the BFF fit is good, both the BFF fit and the Muboy fit are checked for indications of spallation; if either find a correlation that looks like spallation, the event is rejected). Then, the relic candidates are compared to every muon within 30 seconds of the event time. From these correlations, distributions are made of each spallation variable, for each muon type. Correlations to muons preceding the relic candidates make the 'data' distributions; correlations to muons following the relic candidates in time comprise a random sample. The random sample distributions are subtracted from the data distributions, which gives the spallation correlations.

The spallation correlation and random sample distributions are then parameterized by analytic functions (as are shown in Figures 6.10 and 6.11, for example, or see [Appendix A] for a reference of all such plots), and these functions are used as PDFs to make the spallation likelihood. Then, when a correlation between a relic candidate and a preceding muon is checked to determine whether or not it is spallation, a full log-likelihood is calculated from the PDF distributions. In most cases the full

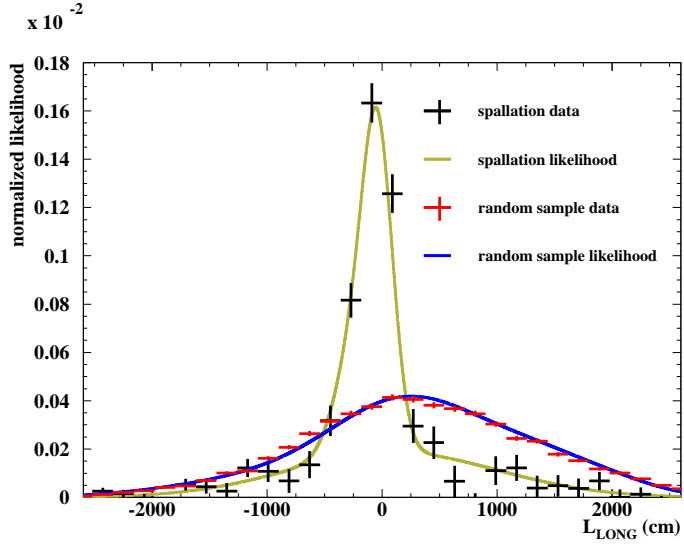


Figure 6.10: SK-I/III longitudinal distance correlations from data with longitudinal distance likelihood functions overlaid for single through-going muons.

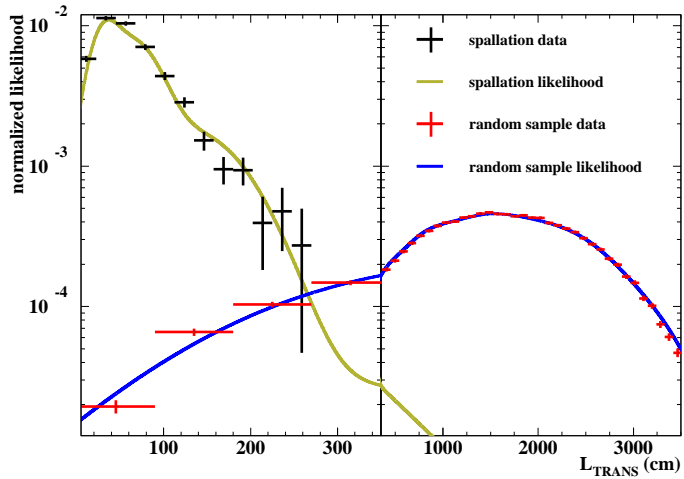


Figure 6.11: SK-I/III transverse distance correlations from data with transverse distance likelihood functions overlaid for single through-going muons.

log-likelihood is simply:

$$\mathcal{L}_{total} = \log \left[\frac{\mathcal{L}_{spall}^{dt}}{\mathcal{L}_{random}^{dt}} \cdot \frac{\mathcal{L}_{spall}^{L_{TRANS}}}{\mathcal{L}_{random}^{L_{TRANS}}} \cdot \frac{\mathcal{L}_{spall}^{L_{LONG}}}{\mathcal{L}_{random}^{L_{LONG}}} \cdot \frac{\mathcal{L}_{spall}^{Q_{PEAK}}}{\mathcal{L}_{random}^{Q_{PEAK}}} \right]$$

A likelihood threshold is determined for each muon type and energy range, and, if the calculated likelihood for an event is larger than the threshold, the event is eliminated. While the likelihood is the primary way that spallation events are elim-

inated, some cuts on specific quantities also exist. For instance, after the most rare and energetic muons (total detected light $> 400,000$ p.e.'s), all data is rejected for a few seconds. Furthermore, multiple muon type events have further complications explained later.

The likelihood thresholds are tuned to remove all statistically significant traces of spallation and still be highly efficient. Due to the low statistics of the analysis, it is virtually impossible to determine with certainty if all spallation events have been removed from the sample. However, if one or two events remain in the sample, they will occur at low energy, and any resulting limit on relic flux will be worsened; thus, as long as no relic signal is claimed, any error introduced will make the results more conservative.

The basic method of tuning the cut is to look at the distribution of the spallation variables, especially dt and L_{TRANS} , as well as the likelihood distribution itself, for the final sample after the spallation cut is applied, and compare it to the random sample. If there is an excess in the final data sample at low dt or L_{TRANS} , or high likelihood, compared to the random sample, then we cut more stringently (lower the likelihood threshold for the appropriate muon type), until the distributions look as close as can be statistically determined.

6.5.3 Multiple Muons

Multiple muons events are when more than one muon is physically traveling through the detector in the same event window. The muons in these muon bundles arise from a common parent atmospheric interaction, and thus not only is the similar timing no coincidence, but the muon directions should be virtually identical. Even though the directions are the same, the muons can be spread out, having entry and exit positions that can be quite different. Also, the dE/dx plot information is compromised, since the electronics only saves the timing information of the first time a PMT is hit inside

an event. Muboy is very good at identifying multiple muon events, and attempts to determine the number of muons involved and fit a track for each. However, the more muons in the bundle, the more difficult it is, and the poorer a job Muboy does with each track. The primary track will be the one Muboy is best able to determine (either due to being the brightest, or the first), and each subsequent track fit will be less and less reliable. Muboy can try to fit a maximum of 10 tracks; furthermore, in some cases Muboy is certain there is many muons involved, but is unable to fit more than a primary track, thus returning the seemingly contradictory result that the muon event is a multiple muon with only one muon track. These multiple muons with one track tend to behave strangely and were considered and tuned separately. Not only does all this make the multiple muon case more complicated than the single muon case, but because there are more muons in each event, multiple muon events are almost four times more likely on average to cause spallation than a single through-going muon (although they occur more than 10 times less often), making this case both difficult and important.

It was found that, even with the light from many muons overlapping, the L_{LONG} and Q_{PEAK} information extracted from a dE/dx plot calculated using the primary muon track information still correlated to real spallation events, although not as strongly as for single muons. For our cut, each muon track was treated as a separate muon event. A second dE/dx profile was calculated for the secondary track, and the secondary track L_{LONG} and Q_{PEAK} variables are used in attempting to determine spallation from the secondary track. When three or more tracks are present, these additional tracks, which were least likely to cause spallation, were grouped together in a cut utilizing only dt and L_{TRANS} information, specially tuned to cut stringently, even at the cost of additional inefficiency, so as to ensure no spallation slipped through. Even the L_{TRANS} distributions for tracks beyond the first differed from the primary track distribution, and required its own likelihood (Fig. A.9). Again, the full details

of the cut can be found in Appendix A. As these events occur only rarely, the increased inefficiency cost of a stricter tuning was not great.

6.5.4 Spallation Summary

SK-I and SK-III likelihood distributions were so similar that they were merged into one combined SK-I/III spallation cut. As with many other cuts, the differences in SK-II required that it be treated separately, so new likelihood functions were constructed for SK-II; it was tuned separately, and has a worse energy threshold due to poorer resolutions. Position dependent efficiency maps were calculated for each spallation cut, revealing that the cut is more efficient near the walls (probably because there are less muons to correlate to). Relic MC vertex distributions, coupled with the position dependent inefficiency maps, were utilized to obtain overall inefficiency numbers (see Table 6.2).

Each cut has two separate tunings - one, stricter cut at lower energies (16-18 MeV for SK-I/III, 17.5-20 MeV for SK-II), and a more efficient higher energy tuning (18-24 MeV for SK-I/III and 20-26 MeV for SK-II).

Table 6.2: Spallation Cut Signal Efficiencies

EFFICIENCY	SK-I/III	SK-II
Low energy	81.8 % (16-18 MeV)	76.2 % (17.5-20 MeV)
High energy	90.8 % (18-24 MeV)	88.2 % (20-26 MeV)

6.6 Pion Cut

Some of the higher energy events in our sample (usually > 30 MeV) are actually pions that are created by atmospheric neutrino interactions. One way to distinguish between pions and electrons is by looking at the 'fuzziness' or 'sharpness' of the Cherenkov ring. This is because pions are quickly captured by an oxygen nucleus, while electrons tend to travel a little farther and multiple scatter. This multiple scattering causes the electron direction to change as it travels, causing the Cherenkov ring to be more poorly defined.

Quantitatively, this difference can be used to construct a tool for discriminating pions and electrons. When the Cherenkov angle for an event is calculated (see section 4.6), a distribution of the cone angles from three-hit combinations (or triplets) is formed. This distribution will be narrower for pions than for electrons, though the two peak at the same angle. Using this logic, a pion likelihood variable was constructed, where pion likelihood is defined as follows (using the triplet distribution):

$$\mathcal{L}_{PION} = \#entries \pm 3^\circ \text{ from peak} / \#entries \pm 10^\circ \text{ from peak}$$

By looking at SN relic MC compared to pion MC, the cut criterion was determined to be 0.58 for all SK run periods. This cut is approximately 1% inefficient.

6.7 Multi Ring Cut

Sometimes an atmospheric neutrino can create several charged particles at the same time. As the particles all come from a common parent interaction, the timing information for the event only shows one timing peak, and thus the event won't be removed by the 2-peak cut. Although most are removed by the Cherenkov angle and pion cuts, a few can survive. To remove these specifically, we use the fact that these multi-particle events have multiple Cherenkov rings (for example, Fig. 6.12).

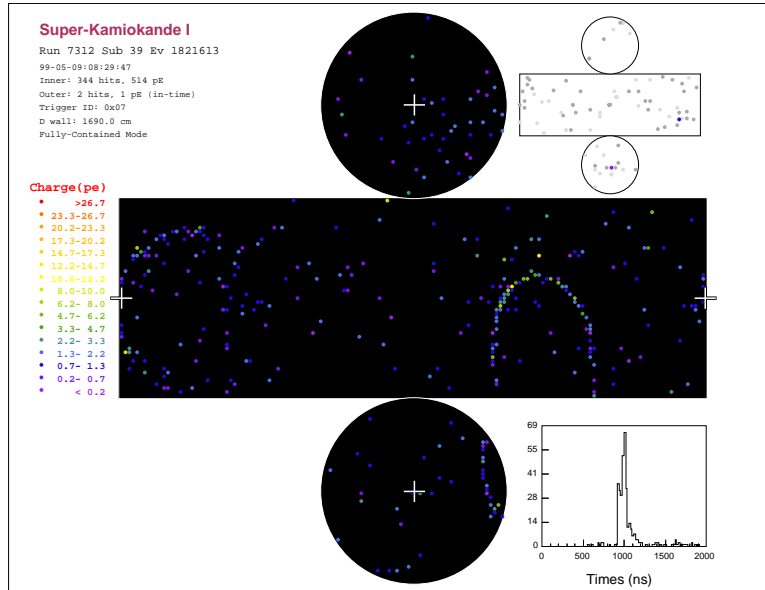


Figure 6.12: Event display of an example multi-ring event. A sharp ring can be seen on the right half of the detector display, and a diffuse ring on the far left.

A ring counting method has already been developed for SK atmospheric neutrino analyses utilizing Hough transforms, and is described in [50]. We used the same method to look for multi-ring events. The software determines an angle between the rings we can use. In rare cases overly fuzzy electron rings can be mistaken for two different rings by the software; for this reason events determined to be multi-particle, but separated by less than 60 degrees, were kept, while events with multiple rings separated by more than 60 degrees were rejected.

6.8 OD-Related Cut

Any event that has an OD trigger is rejected in the first reduction. However, since the OD has such low photo-cathode coverage (the PMTs are more sparsely distributed than in the ID, and are smaller), it sometimes happens that events originating from outside the detector, such as cosmic ray muons, can enter the detector without depositing enough light to trigger the OD. This is especially problematic if the muon then decays into an electron, as decay electrons mimic the SN relic signal and cannot

be rejected by other cuts.

Even if the OD doesn't trigger, however, traces of the muon's passage usually remain in the OD. OD PMTs will still record light, even if it is not enough to reach trigger threshold. By correlating the timing and position of PMT light between OD hits and ID hits, we can look for correlations. If tubes in the OD are hit, and can be correlated to the reconstructed event position in the ID, and the timing information of the hit ID tubes is correlated to that of the hit OD tubes, it may indicate an entering event.

The ID time of flight subtracted timing information for each relic candidate is searched with a 50 ns sliding time window. The time value for which the most hits are seen is considered the peak. Then all OD tubes within 5 m of the reconstructed candidate position are searched. The amount of tubes that saw any light within 150 ns of the ID peak time is determined. If this is two or more tubes, the event is rejected.

The OD timing information is then searched with a 100 ns sliding time window. The maximum number of OD PMTs hit within 100 ns and within 5 m of the candidate vertex is determined; if this is three or more tubes, the event is rejected.

6.9 'Sub-event Cut'

In the first reduction, a 50 μ s cut is applied, which removes any event occurring within 50 μ s of an LE or HE triggered event. Events occurring after an SLE event are ignored, however, as the rate of SLE events is so high, the inefficiency would be too great. However, some events that are only triggered as SLE may be correlated to backgrounds. For instance, atmospheric neutrino interactions that produce sub-Cherenkov muons may also create a prompt gamma (which is therefore earlier in time than the decay electron, which comes from the muon with a half-life of 2.2

μ s). This gamma will usually be low energy (6 MeV) and trigger as SLE only. Furthermore, if the relic candidate is itself a low energy muon that has somehow survived the Cherenkov angle cut, then it may have decayed into a decay electron itself. So although the 50 μ s cut in the first reduction looks to see if there is a LE or HE trigger before the relic candidate, we also need to check after the relic candidate. This collection of additional timing and distance correlation cuts removes such events and is referred to as the 'sub-event cut'.

6.10 Cherenkov Angle Distribution

Charged particles traveling close to the speed of light in pure water emit Cherenkov light in a cone shape with an opening angle of about 42 degrees. Heavier particles, such as muons, pions, and nucleons, may travel slower if their energies are relatively small, producing Cherenkov light with an opening angle that is smaller than 42 degrees. The resolution of our reconstruction algorithm is not perfect (see section 4.6), and multiple scattering can confuse the ring, so the reconstructed Cherenkov angle distribution is not as sharp as we could hope. Fig 6.13 shows the Cherenkov angle distribution of SN relic MC (LMA model). The main peak is determined to be between 38 and 50 degrees, and this is the cut applied to the data to eliminate remaining heavy particles at lower angles, and more isotropic events at higher angles. The region from 38-50 degrees is called the 'signal region'. Due to the poorer energy resolution of SK-II, the cut loses more of the signal for that phase, as the events are pushed to above 50 degrees.

This is not strictly a cut, as the information in these excluded regions is not thrown away, but instead is utilized at a later stage in the analysis.

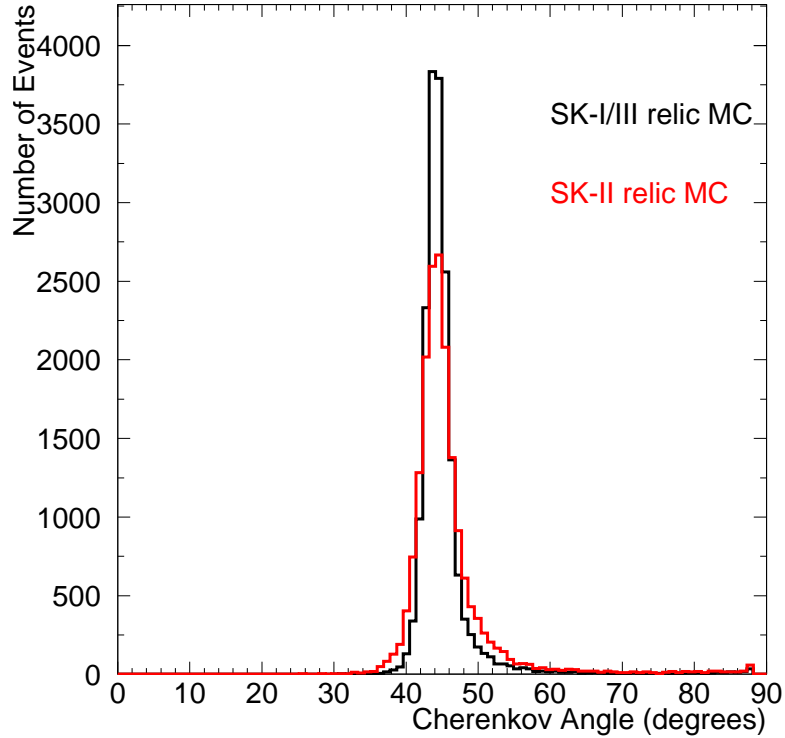


Figure 6.13: Reconstructed Cherenkov angle distribution of SN relic MC (LMA model).

6.11 Reduction Efficiency Summary

Most cut efficiencies were calculated using relic MC. Each relic model has slightly different efficiencies; the ones listed in Table 6.3 are from the LMA model. The systematic error of most cuts was calculated by comparing LINAC [41] MC to LINAC data, or by using the values established in the solar analyses when the cuts are similar (noise reduction, incoming event cut). The OD correlated cut uses a random sample of cosmic ray muon data for OD hit information for determining efficiency. The efficiency of the spallation cut is a function of position (efficiency is greater near the edges of the detector, where the candidate can be correlated to fewer muons), and the vertex distribution of relic MC is used to estimate the average efficiency. The error on this estimation is likely dominated by the statistics of our relic MC and spallation random sample, and is rounded up to be conservative. The efficiency of the solar angle cut is mostly geometric and therefore exact; the only source of systematic error

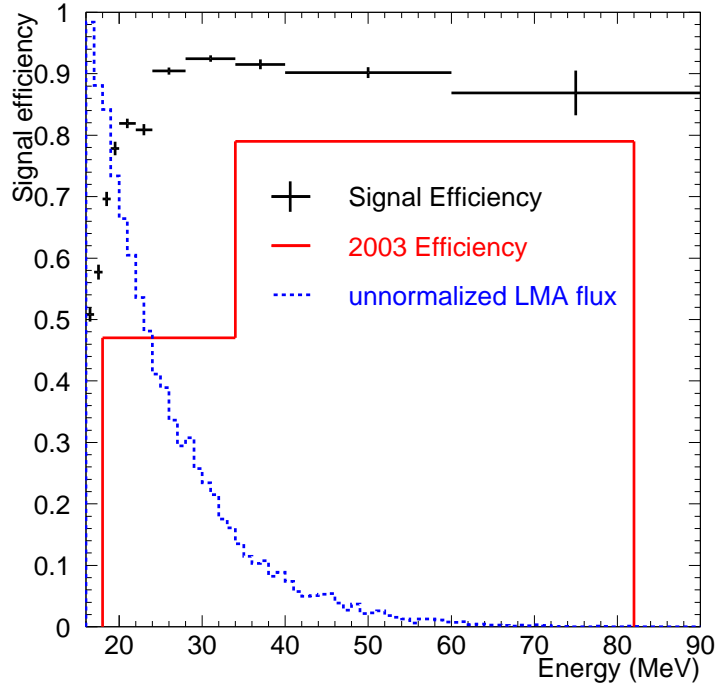


Figure 6.14: Signal efficiency of new analysis compared to 2003 study. An unnormalized LMA spectrum is overplotted to show the importance of the improvements.

comes from the ratio of events falling in each multiple Coulomb scattering goodness bin, as determined from solar MC. Values of the systematic errors, along with the cut efficiencies, can be seen in Table 6.3.

Table 6.3: Cut Signal Efficiency (Systematic Error)

Cut	SK-I	SK-II	SK-III
Noise Reduction	99% (1%)	99% (1%)	99% (1%)
Spall + Solar	88% (1%)	87% (1.4%)	89% (1%)
Incoming event	98% (0.5%)	95% (0.3%)	96% (0.3%)
Pion	98% (0.2%)	97% (0.5%)	98% (0.5%)
Cherenkov angle	95% (0.4%)	88% (3%)	94% (0.3%)
Other cuts	98% (2%)	98% (2%)	98% (2%)
Total	78.5% (2.5%)	69.2% (4.0%)	76.7% (2.5%)

Chapter 7

Analysis: Limit Extraction

After the event selection, a final sample is obtained, which is searched for any indication of SRN events. This chapter describes the methods used to accomplish this.

7.1 Cherenkov Angle Regions

Inverse beta decay positrons in our final sample (> 16 MeV) are highly relativistic and will have a Cherenkov angle of around 42 degrees. For heavier particles, such as muons and pions, only the highest energy ones will have a comparable velocity, and most will travel more slowly and emit light with a small Cherenkov angle. On the other hand, some events can actually reconstruct at higher Cherenkov angles; especially events with a more isotropic nature, such as multiple gamma events.

SK-I SRN MC simulations show that most SRN events are expected to reconstruct at a Cherenkov angle of between 38 and 50 degrees, which is the region of the Cherenkov angle cut (henceforth called the ‘signal region’). However, important information exists at other Cherenkov angles that can be utilized. Although the two remaining backgrounds (see section 5.2) that were considered in the 2003 study (ν_μ and ν_e CC) also mostly fall in the same Cherenkov angle region, the two newly considered remaining backgrounds (NC elastic and μ/π) mostly fall outside the signal

region (see Fig. 7.1). By understanding the behavior of these two backgrounds everywhere, we can use the data at other Cherenkov angles to help normalize the two new backgrounds in the signal region.

To this end, two new Cherenkov angle regions are defined: 20-38 MeV (the ‘low angle’ or ‘ μ/π ’ region) and 78-90 degrees (the ‘high angle’ or ‘NC elastic’ region). Using such broadly defined regions (only three bins in Cherenkov angle) allows us to bypass concerns about Cherenkov angle resolution yet still take advantage of the important information present in the data.

PDFs following the spectrum shape were constructed for each of the four remaining backgrounds and each SRN model considered, for all three Cherenkov angle regions, for all three SK data phases. Most spectra were obtained from MC (see chapter 5), with the exception of the ν_μ spectra, which were obtained from real decay electron data, whose Michel spectrum should be identical to that from the decay of sub-Cherenkov muons. This has the advantage of not requiring any MC systematic errors for this channel, which is our dominant background. The high statistics of decay electrons in SK allows this spectrum to be measured with negligible statistical error as well.

All of the PDFs can be found in Appendix B.

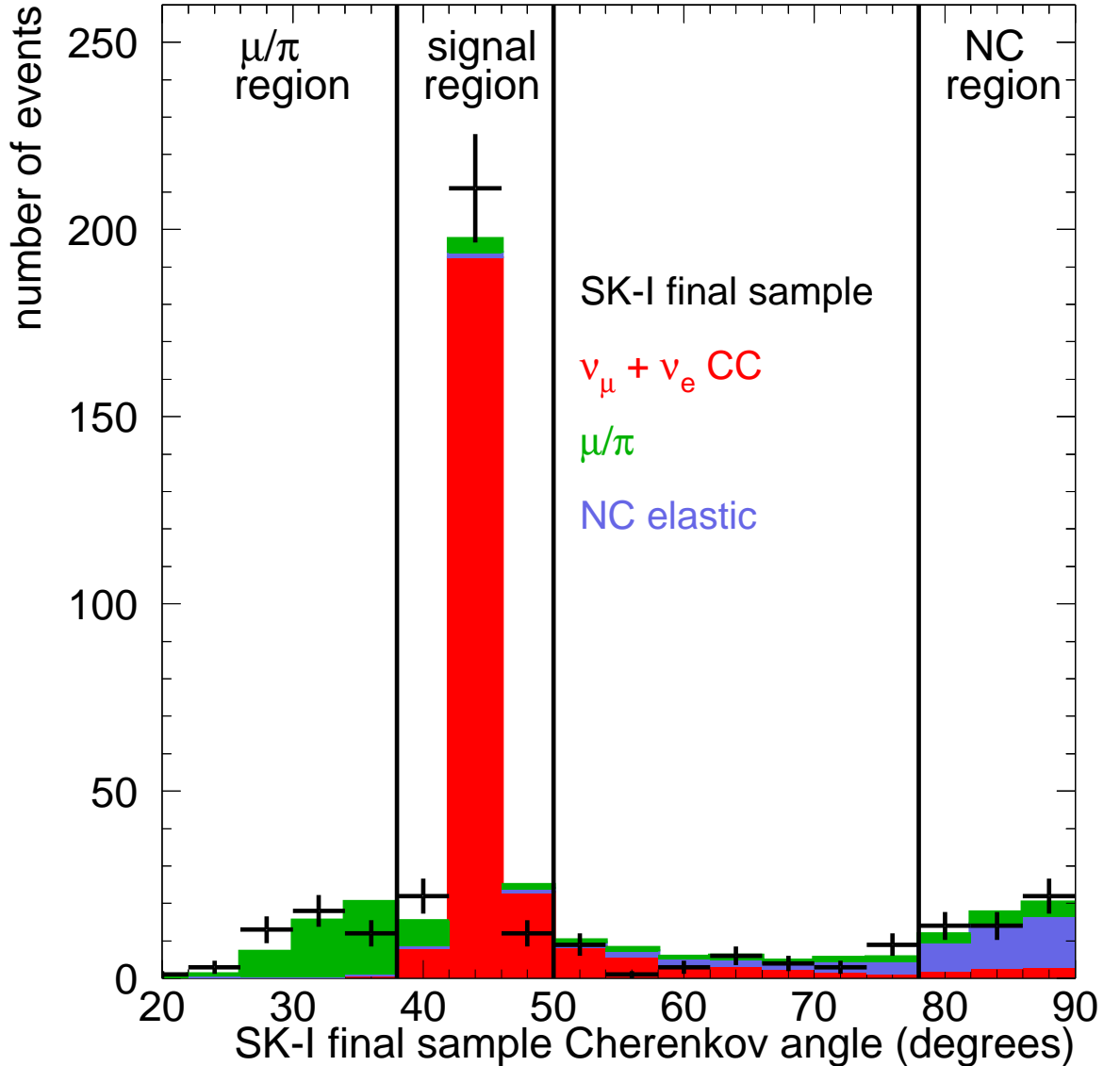


Figure 7.1: Cherenkov angle of SK-I combined final data (all cuts except Cherenkov angle cut applied) overlaid with distributions of the four remaining backgrounds from SK-I MC (same cuts applied). The division of Cherenkov angle regions is also pictured.

7.2 Extended Maximum Likelihood Fit

An unbinned maximum likelihood fit on the final sample spectrum determines how much (if any) SRN signal existed in the final sample. For each SK data phase four remaining backgrounds and a possible SRN component were assumed (5 parameters). The fit is done on the spectrum in each of the three Cherenkov angle regions

simultaneously. For each combination of parameter coefficients c (the coefficients are simply how many events of each channel is assumed in all three Cherenkov angle regions combined), and for each parameter PDF $pdf(E)$, a likelihood is constructed, as follows:

$$\mathcal{L} = \prod_{i=1}^{N_{events}} e^{-\sum_{j=1}^5 c_j} \times \sum_{j=1}^5 c_j pdf_j(E_i) \quad (7.1)$$

The likelihood is maximized for each SK phase separately.

In this formulation the relative normalizations of each Cherenkov angle region is fixed; for instance, for SK-I, if we disregard the 50-78 degree region, which is not used, and normalize the rest to 1, then 99.2% of SRN events (LMA model) are found in the signal region, 0.5% in the high angle region, and the other 0.3% in the low angle region. However, the relative normalization of how many events are in each channel (relic, NC elastic, etc.) is free floating.

The 5 parameter likelihood space is searched, starting at a contribution of 0 relic events. The number of relic events is incremented with a 0.1 event spacing, and for each number of relic events, all reasonable combinations of the four remaining backgrounds is searched, and the combination with the maximum likelihood value is recorded. As the number of relic events is incremented, this gives us a curve of likelihood vs. number of relic events. This roughly Gaussian curve has a peak (best fit), with a width that indicates the significance of any positive indication. The curve also allows us to extract a 90% confidence level limit on the relic flux rate, simply by integrating the curve starting at 0 relic events, and finding the point at which 90% of the area under the entire curve is reached.

Put another way, the 90% CL point $limit_{90}$ is determined by the following simple

relationship, where r represents the number of SN relic events:

$$\int_0^{\text{limit}_{90}} \mathcal{L}(r) dr / \int_0^{\infty} \mathcal{L}(r) dr = 0.9 \quad (7.2)$$

The likelihood curves for each different relic model are very similar, and a representative example is shown in Fig. 8.4.

7.3 Inclusion of Systematic Errors

The following systematic errors are considered:

7.3.1 Energy Scale and Resolution Uncertainty

The energy scale and energy resolution systematic uncertainties are considered to be uncorrelated. They are separately calculated, then added in quadrature. The amount of the energy scale and energy resolution systematic errors are based on the SK solar analyses [32], then slightly increased due to the larger energies involved. The energy resolution systematic uncertainty used in our study is 3%, while the energy scale uncertainties used are 1% for SK-I and SK-III, and 2% for SK-II. Inclusion of this systematic error was not found to have an appreciable effect on the results.

To take the energy scale systematic uncertainty into account, the PDFs for four of the five channels (the ν_μ CC was taken from decay electron data, and is thus not MC, and not susceptible to this error) were shifted by the amount of the uncertainty. To take into account the energy resolution systematic uncertainty, the energy resolution function from reference [32] was applied to the likelihood functions to distort them.

Finally, the full uncertainty was incorporated into the likelihood calculation algorithm as follows. Let ϵ be a variable representing the amount of spectral distortion, such that an ϵ of 1 represents a 1σ deviation in the energy scale and resolution; and

let $\mathcal{L}(\epsilon)$ be the likelihood evaluated with the likelihoods distorted by an amount ϵ . Then the new final likelihood \mathcal{L}' is:

$$\mathcal{L}' = \frac{1}{\sqrt{2\pi}} \int_{-\infty}^{\infty} e^{-\epsilon^2/2} \mathcal{L}(\epsilon) d\epsilon \quad (7.3)$$

such that the originally calculated likelihood \mathcal{L} is now simply the $\epsilon = 0$ case.

7.3.2 Atmospheric ν Background Systematic Errors

Three of the four remaining backgrounds are modeled by SK MC (the exception being the ν_μ CC background, which is modeled by decay electron data). The SK MC is well verified above 100 MeV; however, in the lower energy region of 16-100 MeV that is relevant to our study, the MC accuracy is less well studied. Little data exists to compare to the MC, especially for the NC elastic mode. To incorporate these concerns into the analysis, two systematic errors on the ν_e CC and NC elastic backgrounds were included. These systematics were designed to cover any remaining uncertainties in the MC. As for the other two background channels, the ν_μ CC comes from real data and therefore is not vulnerable to MC inaccuracies, and the μ/π channel is by far the least relevant of the four channels, and therefore the safest to neglect.

For the NC elastic channel, the greatest potential for error lies in the relative normalization across Cherenkov angle regions. The amount of NC elastic found in the 78-90 degree region determines the amount of the fit in the signal region. If the ratio of the amount of NC elastic in the high angle region compared to the signal region as determined by MC is off by some factor, this will tend to have a larger influence on the result than a distortion of the spectrum of the NC elastic in the signal region by the same factor.

For SK-I, the NC elastic MC has 7.4% of events occur in the signal region, while

87% of events occur in the high angle region. Considered is a 100% change in the normalization of the number of NC elastic events in the signal region, with all changes to be correspondingly balanced by a change in the normalization of the high angle region. Thus, a $+1\sigma$ effect would be for 14.8% of events to occur in the signal region, and 79.6% of events to occur in the high angle region, while a -1σ effect would be for no NC elastic events to occur in the signal region, and 94.4% of the events to occur in the high angle region. As we can't have less than 0 events in the signal region, there is a physical boundary at -1σ . Thus, we applied the error asymmetrically from -1 to $+3\sigma$.

For the ν_e CC channel, the relative normalization across Cherenkov angle regions is not a concern, as more than 99% of the events fall into the signal region, so instead a distortion of the spectrum in the signal region was considered. The ν_e CC PDF in the signal region was distorted as follows:

$$\text{PDF}_{new} = \text{PDF}_{old} \times N\left(1 + \frac{0.5\epsilon(E - 16)}{74 \text{ MeV}}\right) \quad (7.4)$$

where E is the energy (MeV), σ is the magnitude of the spectral distortion, and N is a constant such that the new PDF is normalized the same as the old.

A -2σ effect would reduce the PDF to 0 at 90 MeV. This was considered to be unphysical, and thus a -1σ effect was considered the physical lower bound, forcing us to apply this error in the same asymmetric manner as the NC elastic, from -1 to $+3\sigma$.

We applied the background channel systematics using an integral method with a weighting function (which acts as a Bayesian prior). However, as our error is applied over an asymmetric region (-1 to $+3\sigma$), we could not use a symmetric Gaussian (such as we use in the next section) without introducing a bias in our result. Instead, we used a weighted Gaussian that as closely as possible maintained the properties of the

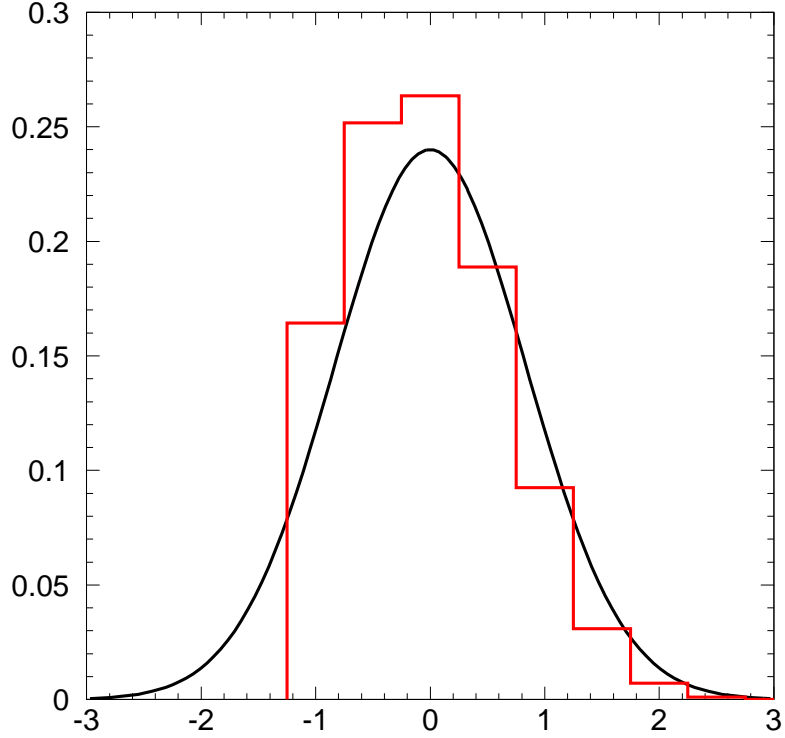


Figure 7.2: Example of a symmetric Gaussian (black) and the asymmetric weighted Gaussian used to normalize the atmospheric neutrino background systematics. Horizontal axis is the amount of the systematic distortion in units of sigma.

symmetric Gaussian.

Specifically, in the case of a symmetric error (i.e., $-\infty$ to ∞), a normal Gaussian would have the following properties: (1) expectation value (first moment) = 0, (2) variance (second moment) = σ^2 . Our weighted Gaussian (see Fig. 7.2) was constructed such that its properties (integrated over σ from -1 to 3) were the same as the symmetric case. This weighted Gaussian was normalized to 1 and used in both the ν_e CC and NC elastic cases, as their integration ranges were identical.

The integral method of applying the systematic error is as follows. Let $G(\sigma)$ be our weighted Gaussian function described above. Let $\mathcal{L}(r, \sigma)$ be the likelihood as a function of SN relic events and whichever systematic error is under consideration. Then, the likelihood after the application of the systematic error of either of the background channels is:

$$\mathcal{L}'(r) = \int_{-1}^3 \mathcal{L}(r, \sigma) G(\sigma) d\sigma \quad (7.5)$$

Inclusion of the atmospheric ν background systematics changed the result (towards a less stringent limit) by less than 6%.

7.3.3 Energy Independent Efficiency Systematic Error

The energy independent portion of the efficiency systematic error is assumed uncorrelated. The systematic error of each cut, as shown in Table 6.3, is added in quadrature, to get the total efficiency systematic error of the reduction. The total efficiency systematic error also includes the uncertainty in the fiducial volume cut, inverse beta cross section, and livetime calculation, as shown in Table 7.1.

The fiducial volume and livetime calculation systematic errors are the same as, and taken from, the SK solar analyses [31, 32].

To apply this systematic error, the likelihood curve (likelihood as a function of number of SN relic events) is modified. The modification for each value of the likelihood is as follows, where ϵ is the efficiency, σ is the efficiency systematic error, $P(\epsilon)$ is a probability function in the shape of a Gaussian centered on ϵ_0 with width $\epsilon_0\sigma$, r is the number of relic events seen in the data, and R is the number of relic

Table 7.1: Total Efficiency Systematic Error

Error Source	SK-I	SK-II	SK-III
Cut reduction	3.1%	4.4%	3.1%
Fiducial Volume	1.3%	1.1%	1.0%
Cross Section	1.0%	1.0%	1.0%
Livetime	0.1%	0.1%	0.1%
Total	3.51%	4.65%	3.41%

events actually interacting in the detector, such that $r = \epsilon R$:

$$\mathcal{L}'(R) = \int_{\epsilon=0}^1 \mathcal{L}(\epsilon R) P(\epsilon) \epsilon \, d\epsilon \quad (7.6)$$

This error is applied last, after all other calculations are complete. Inclusion of this systematic error changed the result (making the limit less stringent) by a few percent.

Chapter 8

Results

8.1 Basic Results

Figures 8.1, 8.2, and 8.3 show the final sample data spectrum in each Cherenkov angle region, overlaid with the best fit results for the LMA model. For SK-I, the relic best fit is negative and unphysical (for all models), so zero relic contribution is shown. For SK-II and SK-III, a positive indication (not significant) of a relic component was found. The 90% CL upper flux limits differ for each model, and are summarized in Table 8.1. Example likelihood curves for the LMA model fit are shown in Fig. 8.4. More detailed numerical values for the results are given in Appendix D.

Table 8.1: 90 % CL flux limit ($\bar{\nu}$ cm⁻² s⁻¹), $E_\nu > 17.3$ MeV

Model	SK-I	SK-II	SK-III	All	Predicted
Gas Infall (97)	<2.1	<7.5	<7.8	<2.8	0.3
Chemical (97)	<2.2	<7.2	<7.8	<2.8	0.6
Heavy Metal (00)	<2.2	<7.4	<7.8	<2.8	< 1.8
LMA (03)	<2.5	<7.7	<8.0	<2.9	1.7
Failed SN (09)	<2.4	<8.0	<8.4	<3.0	0.7
6 MeV (09)	<2.7	<7.4	<8.7	<3.1	1.5

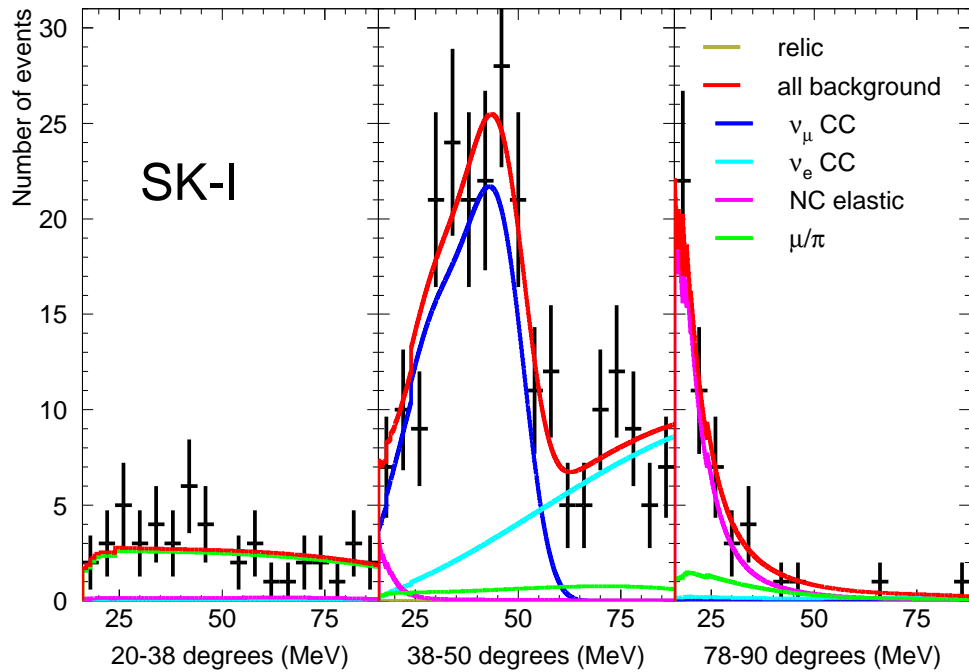


Figure 8.1: SK-I LMA best fit result. The relic best fit is negative, so a relic fit of 0 is shown.

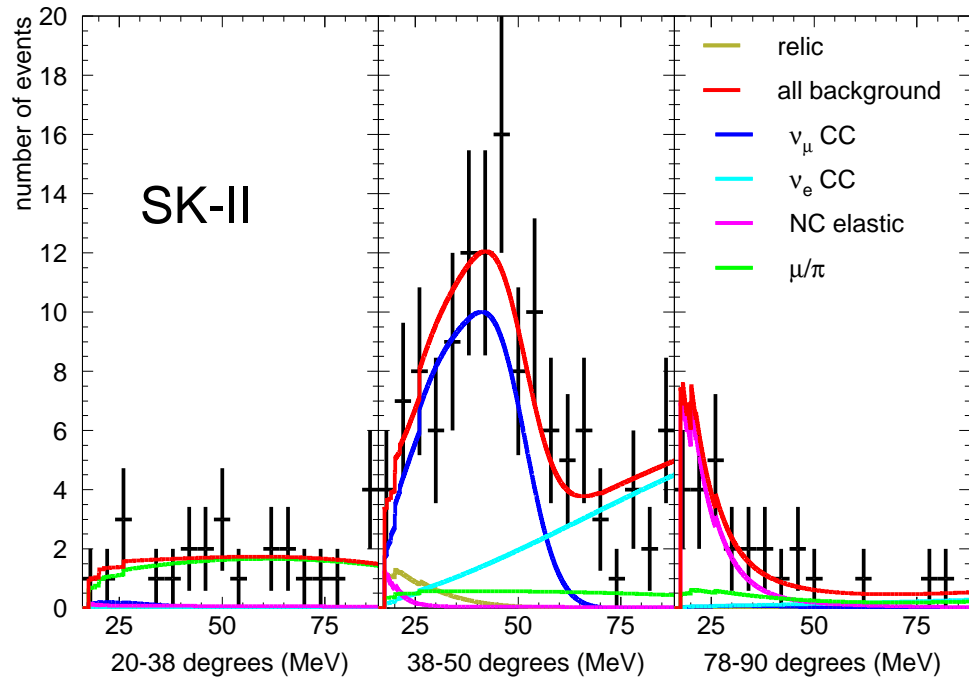


Figure 8.2: SK-II LMA best fit result. The relic best fit is 3.05 events per year interacting in the detector (before reduction efficiencies).

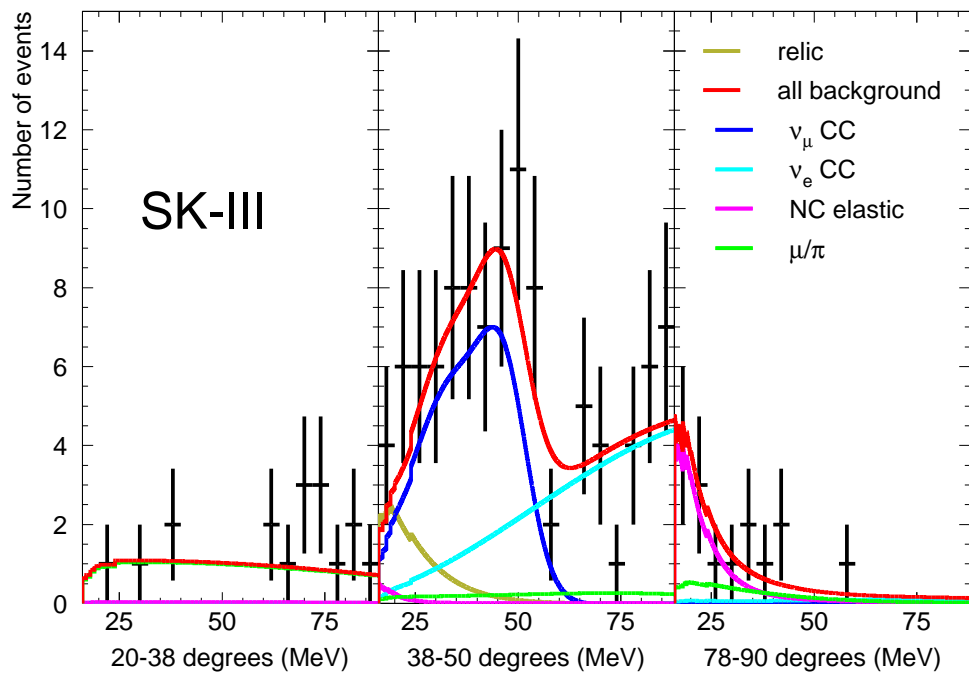


Figure 8.3: SK-III LMA best fit result. The relic best fit is 6.9 events per year interacting in the detector (before reduction efficiencies).

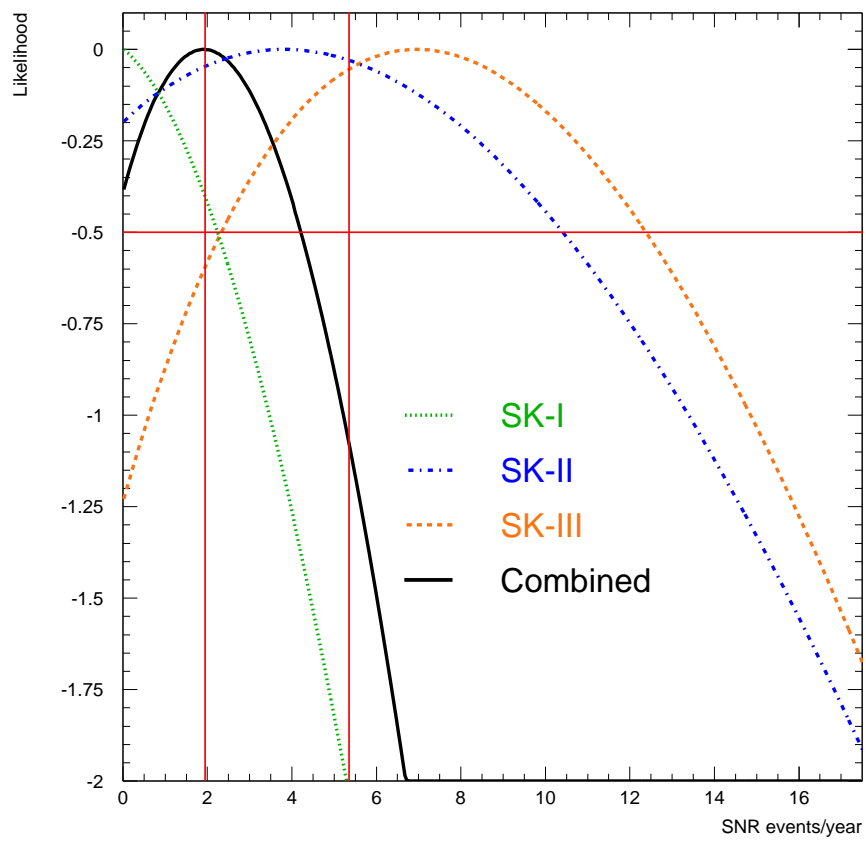


Figure 8.4: Example likelihood curves from the LMA model. Vertical lines represent best fit and 90 % CL results for the combined fit.

8.2 Comparison to 2003 Result

The new analysis has a lower energy threshold than the 2003 study, so the results are not immediately comparable. Furthermore, the previous study presented its result in a model independent fashion, since the result for all models were so similar. Although we verified that with an 18 MeV energy threshold the SK-I results were similar enough to justify a model-independent approach, the lower energy threshold and new data required model dependent results. For comparison purposes, we consider the LMA model. The limit is $2.9 \bar{\nu} \text{ cm}^{-2} \text{ s}^{-1} > 16 \text{ MeV}$ (positron energy), which is equivalent to $2.0 \bar{\nu} \text{ cm}^{-2} \text{ s}^{-1} > 18 \text{ MeV}$ positron energy. It is notable that this result is less stringent than the 2003 result of $1.2 \bar{\nu} \text{ cm}^{-2} \text{ s}^{-1}$ positron energy $> 18 \text{ MeV}$. There are multiple reasons for this.

First, a 0^{th} order approximation of the inverse beta cross section was then used. Now, the full cross section from [51] is used. This raises the limit by about 8%. If events with pre and post-activity are also removed, the old-style analysis limit becomes $1.35 \text{ cm}^{-2} \text{ s}^{-1}$. Furthermore, the binned χ^2 method used assumed Gaussian statistics, while Poissonian statistics are more appropriate considering how few events there are at low energy. This alone would change the limit from 1.2 to $1.7 \text{ cm}^{-2} \text{ s}^{-1}$. When all these corrections are combined, the original analysis result of $1.2 \bar{\nu} \text{ cm}^{-2} \text{ s}^{-1}$ instead becomes $1.9 \bar{\nu} \text{ cm}^{-2} \text{ s}^{-1}$.

With my improved analysis, if we neglect atmospheric ν background systematics, (but keep the other systematics, none of which were included in the 2003 study), the SK-I only LMA result is $1.6 \bar{\nu} \text{ cm}^{-2} \text{ s}^{-1}$ ($> 18 \text{ MeV}$ positron energy), which is more stringent than the published analysis with these corrections. However, the SK-II and SK-III data shows a hint of a signal, which causes the limit to become less stringent when all the data are combined, for the final LMA result (with all systematics) of $2.0 \bar{\nu} \text{ cm}^{-2} \text{ s}^{-1} > 18 \text{ MeV}$ positron energy, or $2.9 \bar{\nu} \text{ cm}^{-2} \text{ s}^{-1} > 16 \text{ MeV}$ positron energy.

So, in summary, the difference is in part due to corrections that should be made

to the 2003 result; in part due to inclusion of many new conservative systematics; and also in part due to the positive indication of a relic signal in SK-II and SK-III data.

Chapter 9

Limit on SN Emission Spectrum

As well as giving the usual model dependent limit result, another formulation is possible, following the procedure outlined in [19, 52]. The basic idea is to parameterize all relic models into two free parameters, and then to express the result as an exclusion contour in this two dimensional space. The goal is to simplify matters for modelers and the community.

9.1 Making a General Relic Model

To summarize [52], the SN relic spectrum at SK ϕ is as follows:

$$\frac{d\phi}{dE_\nu}(E_\nu) = \int_0^\infty [(1+z)\varphi[E_\nu(1+z)]] [R_{SN}(z)] \left[\left| \frac{c}{dz} \right| dz \right] \quad (9.1)$$

where E_ν is the neutrino energy; φ is the neutrino emission per supernova; R_{SN} is the evolving core-collapse supernova rate; and z is the standard redshift parameter.

$R_{SN}(z)$ can be expressed in terms of the star formation rate $R_{SF}(z)$ by:

$$R_{SN} \simeq \frac{R_{SF}(z)}{143M_\odot} \quad (9.2)$$

where the Salpeter IMF is assumed, and the star formation rate is well mea-

sured, with an error of approximately 20% at $z = 0$.

Furthermore, the neutrino emission spectrum can be modeled in terms of a Fermi-Dirac function:

$$\varphi(E_\nu) = E_{\bar{\nu}_e, tot} \frac{120 E_\nu^2}{7\pi^4 T^4} \frac{1}{e^{E_\nu/T} + 1} \quad (9.3)$$

With T being the energy (in units of MeV), and $E_{\bar{\nu}_e, tot}$ being the total energy.

With this formulation, the SN relic rate can be directly related to the two free parameters: T (the neutrino temperature in MeV), and the luminosity (or total energy) of an average supernova.

9.2 Method

The kinematics of inverse beta decay are well understood, as is the cross section [51]. The volume of water in SK, and therefore the amount of proton targets in the volume ($\sim 1.5 \times 10^{33}$ in 22.5 ktons of water), can be calculated.

MC was made from 2 to 8 MeV neutrino temperature, in half MeV steps. A spectrum of positrons in SK was simulated for each temperature (Fig. 9.1).

300,000 events were made for each temperature. These events had the full relic analysis applied to them; all the cuts from the event reduction (see chapter 6) were applied, and the final samples had the full unbinned maximum likelihood fit applied.

Two types of limits were obtained. In one case, each neutrino temperature was considered separately, as a separate relic model, and a limit on rate (and therefore average luminosity) was obtained. These 1-D limits can be connected with a line. In the second case, the likelihoods of all neutrino temperatures were considered simultaneously, and a true 2-D exclusion contour obtained.

The results are shown in two plots. In the first (Fig. 9.2, neutrino temperature is plotted against event rate in the SK fiducial volume (before efficiency losses). On

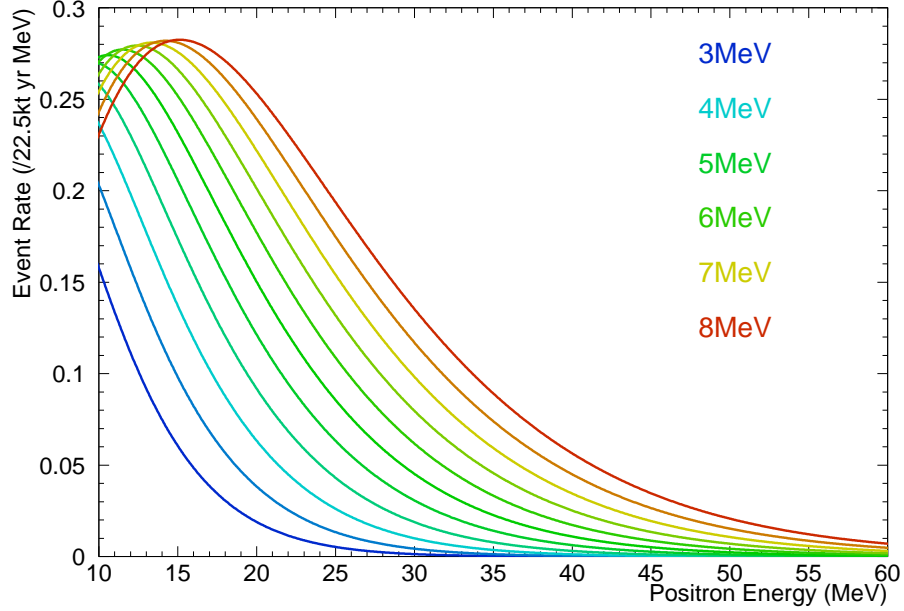


Figure 9.1: True spectra of positrons in SK originating from SN relic neutrinos of a particular temperature (SN $\bar{\nu}_e$ luminosity of 510^{52} ergs assumed).

this plot each of the SN relic models we considered are plotted as well for comparison. In the second plot (Fig. 9.3, both free parameters (neutrino temperature and average luminosity) are plotted, as well as allowed regions from IMB and Kamiokande from the 1987A data. The various considered relic models are not overplotted on the second plot; this is because some of the models are older, and may have used different values of the star formation rate, IMF, etc, than the modern values assumed in this formulation. Thus, overplotting is not appropriate unless each model is checked in detail, and in some cases modified to reflect differences.

The results (1-D limit) are also summarized in Table 9.1.

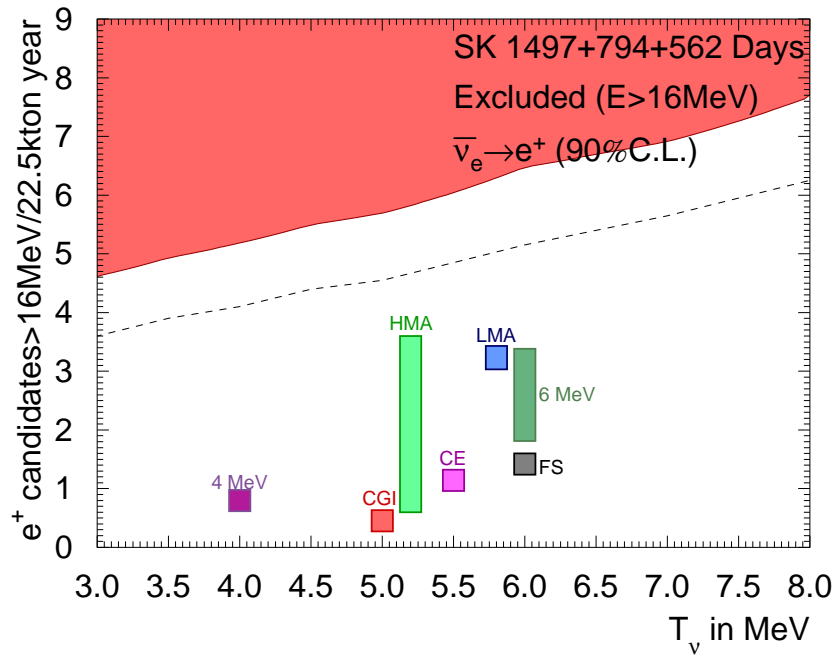


Figure 9.2: Exclusion contour plotted in a parameter space of SRN event rate vs. neutrino temperature. The red shows the 90% CL result. The dashed line shows the individual 90% CL results of each temperature considered separately, which is not a true 2-D exclusion contour. CGI is Cosmic Gas Infall model, HMA is Heavy Metal Abundance model, CE is Chemical Evolution model, LMA is Large Mixing Angle model, FS is Failed Supernova model, and the 6 and 4 MeV cases are assuming that neutrino temperature, from [19].

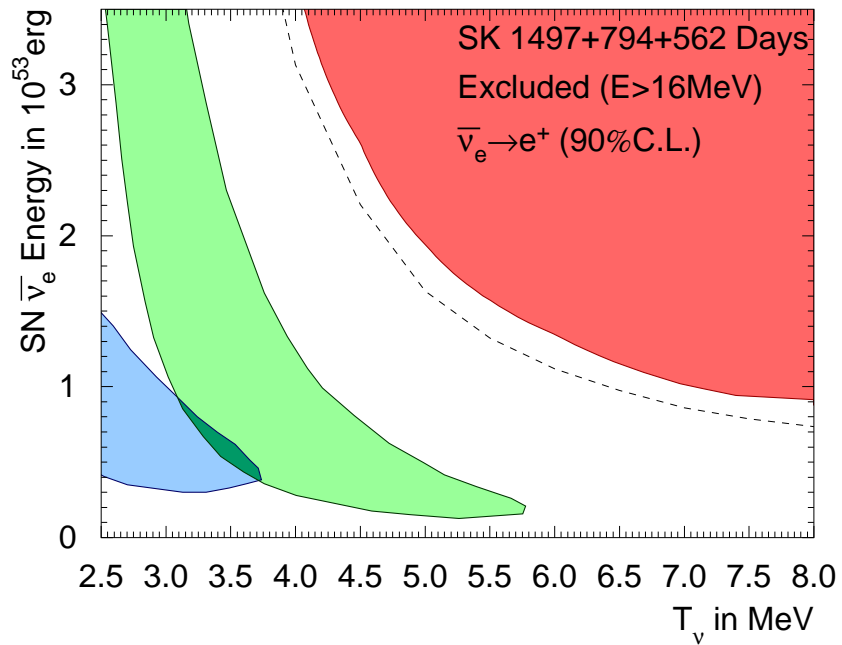


Figure 9.3: Results plotted as an exclusion contour in SN neutrino luminosity vs. neutrino temperature parameter space. The green and blue contours show IMB and Kamiokande allowed areas for 1987A data, respectively (originally from [53]). The red shows our new 90% CL result. The dashed line shows the individual 90% CL results of each temperature considered separately, which is not a true 2-D exclusion contour. Results are in the form of Fig. 6 from [52].

Table 9.1: Summary of limit values.

$\bar{\nu}_e$ Temperature (MeV)	$E_{\bar{\nu}_e,tot}$ ($\times 10^{53}$ ergs)
3.0	9.0
3.5	4.8
4.0	2.9
4.5	2.1
5.0	1.5
5.5	1.3
6.0	1.1
6.5	0.92
7.0	0.82
7.5	0.75
8.0	0.70

Chapter 10

Conclusion and Future

As of this writing, this analysis replaces the published 2003 limit [20] as the most sensitive study and limit on the SN relic neutrino flux to date. The SK study has been improved with an expanded data set, greatly improved event selection (average efficiency improved for SK-I data from 52% to 75%), lowered energy threshold (from 18 to 16 MeV positron energy for SK-I/III), an unbinned maximum likelihood fit (as opposed to a χ^2), and many new systematics.

Although the SN relic signal was not seen, limits were placed on a variety of models, and a positive indication was seen in the new (SK-II and SK-III) data which could be a tantalizing hint of a signal, although the indication was not significant. A limit is also on the neutrino emission spectrum.

Already (2011) SK-IV has over 50 kt-years of data, and the new electronics may allow for improved identification of low energy pre-activity, which could reduce backgrounds further for this new data. However, even if we are on the threshold of seeing the SN relic signal, it is unlikely that a discovery can be made in the near future, due to the low rate and the significance required for a certain discovery. The best prospect for near future SN relic detection is through neutron tagging, for which proposals have already been made [36]. A test facility to determine the feasibility of

such an experiment is already in operation.

Bibliography

- [1] S. Woosley and T. Janka, “The physics of core-collapse supernovae,” *Nature Physics*, vol. Volume 1, Issue 3, pp. 147–154, 2005.
- [2] S. Colgate and R. White, “The hydrodynamic behavior of supernovae explosions,” *Astrophys. J.*, vol. 143, pp. 626–681, 1966.
- [3] H. Nunokawa, “Supernova neutrino oscillations,” *Nucl. Phys. B*, vol. 95, pp. 193–200, 2001.
- [4] The Hubble Heritage Project, “SN1987a in the Large Magellanic Cloud.”
- [5] K. S. Hirata et al., “Observation in the Kamiokande-II detector of the neutrino burst from supernova SN1987a,” *Phys. Rev. D*, vol. 38, pp. 448–458, 1988.
- [6] J. C. Van Der Velde *et al.*, “Neutrinos from SN1987a in the IMB detector,” *Nucl. Instrum. Meth.*, vol. A264, pp. 28–31, 1988.
- [7] E. Cappellaro, R. Evans, and M. Turatto, “A new determination of supernova rates and a comparison with indicators for galactic star formation,” *Astron. Astrophys.*, vol. 351, p. 459, 1999.
- [8] G. Fogli, E. Lisi, A. Mirizzi, and D. Montanino, “Probing supernova shock waves and neutrino flavor transitions in next-generation water-Cerenkov detectors,” *JCAP*, vol. 0504, p. 002, 2005.
- [9] G.S. Bisnovatyi-kogan and Z.F. Seidov, “Supernovae, neutrino rest mass, and the middle-energy neutrino background in the universe,” *Ann. N.Y. Acad. Sci.*, vol. 422, pp. 319–327, 1984.
- [10] L. M. Krauss, S. L. Glashow, and D. N. Schramm, “Antineutrino astronomy and geophysics,” *Nature*, vol. 310, pp. 191–198, 1984.
- [11] S. E. Woosley, J. R. Wilson, and R. Mayle, “Gravitational collapse and the cosmic antineutrino background,” *Astrophysical Journal*, vol. 302, pp. 19–34, Mar. 1986.
- [12] T. Totani, K. Sato, and Y. Yoshii, “Spectrum of the Supernova Relic Neutrino Background and Evolution of Galaxies,” *Astrophysical Journal*, vol. 460, p. 303, Mar. 1996.

- [13] D. H. Hartmann and S. E. Woosley, “The cosmic supernova neutrino background,” *Astroparticle Physics*, vol. 7, no. 1-2, pp. 137 – 146, 1997.
- [14] R. A. Malaney, “Evolution of the cosmic gas and the relic supernova neutrino background,” *Astroparticle Physics*, vol. 7, no. 1-2, pp. 125 – 136, 1997.
- [15] C. Lunardini, “Diffuse neutrino flux from failed supernovae,” *Phys. Rev. Lett.*, vol. 102, p. 231101, Jun 2009.
- [16] M. Kaplinghat, G. Steigman, and T. P. Walker, “Supernova relic neutrino background,” *Phys. Rev. D*, vol. 62, p. 043001, Jul 2000.
- [17] S. Ando, K. Sato, and T. Totani, “Detectability of the supernova relic neutrinos and neutrino oscillation,” *Astroparticle Physics*, vol. 18, no. 4, pp. 307 – 318, 2003.
- [18] L. Strigari, M. Kaplinghat, G. Steigman, and T. Walker, “The supernova relic neutrinos backgrounds at KamLAND and Super-Kamiokande,” *Journal of Cosmology and Astroparticle Physics*, vol. 0403:007, 2004.
- [19] S. Horiuchi, J. F. Beacom, and E. Dwek, “Diffuse supernova neutrino background is detectable in super-kamiokande,” *Phys. Rev. D*, vol. 79, p. 083013, Apr 2009.
- [20] M. Malek et al., “Search for supernova relic neutrinos at Super-Kamiokande,” *Phys. Rev. Lett.*, vol. 90, p. 061101, 2003.
- [21] M. Malek, *A Search for Supernova Relic Neutrinos*. PhD thesis, State University of New York at Stony Brook, 2003.
- [22] W. Zhang et al., “Experimental limit on the flux of relic antineutrinos from past supernovae,” *Phys. Rev. Lett.*, vol. 61, pp. 385–388, Jul 1988.
- [23] K. S. Hirata, *Search for Supernova Neutrinos at Kamiokande-II*. PhD thesis, University of Tokyo, 1991.
- [24] M. Aglietta *et al.*, “Limits on low-energy neutrino fluxes with the Mont Blanc liquid scintillator detector,” *Astropart. Phys.*, vol. 1, pp. 1–9, 1992.
- [25] B. Aharmim *et al.*, “A Search for Neutrinos from the Solar hep Reaction and the Diffuse Supernova Neutrino Background with the Sudbury Neutrino Observatory,” *Astrophys.J.*, vol. 653, pp. 1545–1551, 2006.
- [26] T. K. Collaboration, “A study of extraterrestrial antineutrino sources with the KamLAND detector,” 2011. * Temporary entry *.
- [27] Y. Fukuda et al., “Evidence for oscillation of atmospheric neutrinos,” *Phys. Rev. Lett.*, vol. 81, pp. 1562–1567, Aug 1998.
- [28] Y. Fukuda et al., “Measurements of the solar neutrino flux from super-kamiokande’s first 300 days,” *Phys. Rev. Lett.*, vol. 81, pp. 1158–1162, Aug 1998.

- [29] C. Yanagisawa and T. Kato, “Report on the Super-Kamiokande accident,” tech. rep., Stony Brook University, November 2001.
- [30] T. Totani and K. Sato, “Spectrum of the relic neutrino background from past supernovae and cosmological models,” *Astroparticle Physics*, vol. 3, no. 4, pp. 367 – 376, 1995.
- [31] J. Hosaka et al., “Solar neutrino measurements in Super-Kamiokande-I,” *Phys. Rev. D*, vol. 73, 112001, 2006.
- [32] J. P. Cravens et al., “Solar neutrino measurements in Super-Kamiokande-II,” *Phys. Rev. D*, vol. 78, 032002, 2008.
- [33] R. Wendell et al., “Atmospheric neutrino oscillation analysis with subleading effects in super-kamiokande i, ii, and iii,” *Phys. Rev. D*, vol. 81, p. 092004, May 2010.
- [34] H. Nishino et al., “Search for proton decay via $p \rightarrow e^+\pi^0$ and $p \rightarrow \mu^+\pi^0$ in a large water cherenkov detector,” *Phys. Rev. Lett.*, vol. 102, p. 141801, Apr 2009.
- [35] S. Desai et al., “Search for dark matter WIMPs using upward through-going muons in Super-Kamiokande,” *Phys. Rev. D*, vol. 70, p. 083523, Oct 2004.
- [36] J. F. Beacom and M. R. Vagins, “Antineutrino spectroscopy with large water Čerenkov detectors,” *Phys. Rev. Lett.*, vol. 93, p. 171101, Oct 2004.
- [37] Fukuda et al., “The Super-Kamiokande detector,” *Nucl. Instrum. Meth.*, vol. A501, pp. 418–462, 2003.
- [38] H. Nishino *et al.*, “The new front-end electronics for the Super-Kamiokande experiment,” vol. 1, pp. 127 –132, Oct. 2007.
- [39] S. Yamada, Y. Obayashi, M. Shiozawa, and Y. Hayato, “Commissioning of the new online system for the super-kamiokande experiment,” in *Nuclear Science Symposium Conference Record, 2008. NSS '08. IEEE*, pp. 1387 –1390, oct. 2008.
- [40] T. K. Ohsuka et al., “KEK report,” tech. rep., 1985.
- [41] M. Nakahata et al., “Calibration of Super-Kamiokande using an electron LINAC,” *Nucl. Instr. Meth.*, vol. A421, pp. 113–129, 1999.
- [42] K. Abe *et al.*, “Solar neutrino results in Super-Kamiokande-III,” *Phys.Rev.*, vol. D83, p. 052010, 2011.
- [43] E. Blaufuss *et al.*, “N-16 as a calibration source for Super-Kamiokande,” *Nucl.Instrum.Meth.*, vol. A458, pp. 638–649, 2001.
- [44] P. Vogel and J. F. Beacom, “Angular distribution of neutron inverse beta decay, $\bar{\nu}_e + p \rightarrow e^+ + n$,” *Phys. Rev. D*, vol. 60, p. 053003, Jul 1999.

- [45] S. Desai, *High energy neutrino astrophysics with Super-Kamiokande*. PhD thesis, Boston University, 2004.
- [46] Z. Conner, *A Study of Solar Neutrinos Using the Super-Kamiokande Detector*. PhD thesis, University of Maryland, 1997.
- [47] Y. Hayato, “Neut,” *Nuclear Physics B - Proceedings Supplements*, vol. 112, no. 1-3, pp. 171 – 176, 2002.
- [48] H. Nishino, *Search for Nucleon Decay into Charged Antilepton plus Meson in Super-Kamiokande*. PhD thesis, University of Tokyo, 2009.
- [49] G. Mitsuka, *Study of Non-Standard Neutrino Interactions with Atmospheric Neutrino Data in Super-Kamiokande*. PhD thesis, University of Tokyo, 2009.
- [50] M. Shiozawa, *Search for Proton Decay $p \rightarrow e + \pi^0$ in a Large Water Cherenkov Detector*. PhD thesis, University of Tokyo, 1999.
- [51] A. Strumia and F. Vissani, “Precise quasielastic neutrino nucleon cross section,” *Phys. Lett.*, vol. B564, pp. 42–54, 2003.
- [52] J. F. Beacom, “The Diffuse Supernova Neutrino Background,” *Ann. Rev. Nucl. Part. Sci.*, vol. 60, pp. 439–462, 2010.
- [53] B. Jegerlehner, F. Neubig, and G. Raffelt, “Neutrino oscillations and the supernova SN1987A signal,” *Phys.Rev.*, vol. D54, pp. 1194–1203, 1996.
- [54] O. S. Kirsebom, S. Hyldegaard, M. Alcorta, *et al.*, “Precise and accurate determination of the ^8B decay spectrum,” *Phys. Rev. C*, vol. 83, p. 065802, Jun 2011.
- [55] K. Kobayashi, H. Akimune, H. Ejiri, H. Fujimura, M. Fujiwara, *et al.*, “De-excitation gamma-rays from the s-hole state in N-15 associated with proton decay in O-16,” 2006.

Appendices

A Appendix A - Spallation

Likelihoods are fit based on data. For the random sample, real correlations to muons 30 seconds after relic candidates are used. For the spallation sample, real correlations to muons 30 seconds before relic candidates are used, minus the random sample.

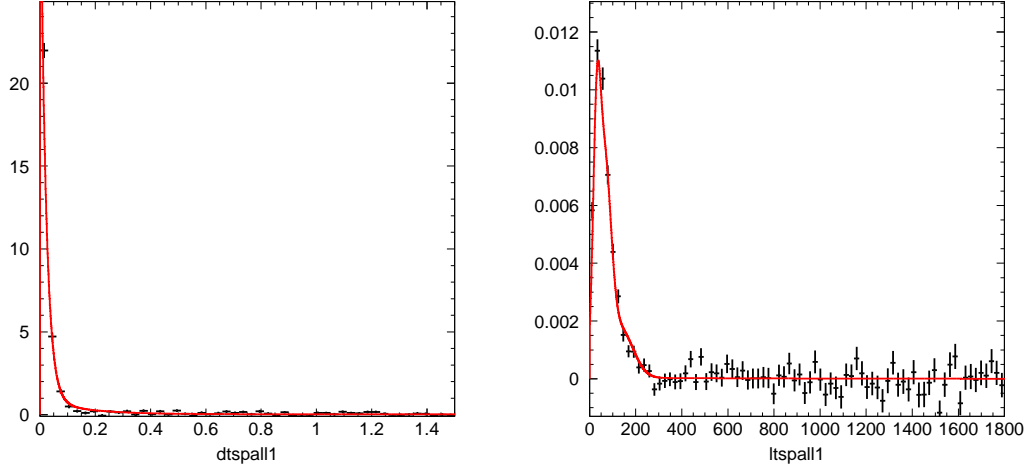
Samples of correlations for relic candidates > 14 MeV, 15 MeV, and 16 MeV were examined. Initially, there were hopes of lowering the energy threshold below 16 MeV. Using correlations from data lower in energy than the analysis threshold risks the possibility of introducing new spallation products that could alter the distributions; however, using the above 16 MeV distributions alone meant insufficient statistics for good fits for all muons types except the single through-going muon sample. Data above 15 MeV was eventually decided on and used as the basis of the likelihoods.

The likelihoods used, compared to the data distributions, are shown in the following plots, for all four spallation likelihood variables (dt , L_{TRANS} , L_{LONG} , and Q_{PEAK}), for all four different muon categorizations (single through-going, stopping, multiple muons with only one track fit by Muboy [type 1], and multiple muons with more than one track fit [type 2]), for both spallation and random samples (the dt random sample is simply a flat line and not shown).

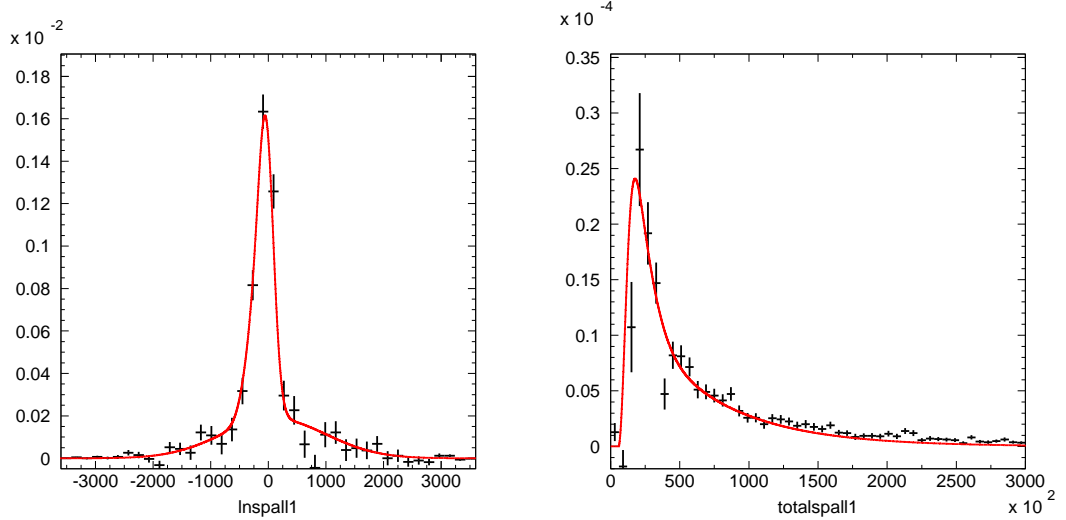
Table A.1: Information on spallation products expected in SK. Energies are total energy released, which can, depending on the decay mode, in some cases be divided into multiple decay particles. All decays are beta decays, some can include neutrons or gammas. Whether or not a neutron emitting mode is common or not is also listed, which can be important for neutron tagging background reduction. Data is from NuDat 2.5 project, NNDC, Brookhaven. Some decays may release more energy than shown, but the beta particle isn't allowed all the way to the ground state, limiting the beta end-point energy to less than the total energy release - for instance, in 8B [54].

Isotope	$\tau_{1/2}$ (sec)	released E (MeV)	Neutron?
${}^{13}_8O$	0.00858	17.8	no
${}^{11}_3Li$	0.00875	20.6	yes
${}^{12}_7N$	0.011	17.3	no
${}^{14}_5B$	0.0125	20.6	no
${}^{13}_5B$	0.0173	13.44	no
${}^{12}_5B$	0.0202	13.37	no
${}^{12}_4Be$	0.0215	11.7	<1%
8_2He	0.119	10.65	yes
9_6C	0.127	16.8	no
9_3Li	0.178	13.6	yes
${}^{16}_6C$	0.747	8.01	yes
8_5B	0.77	15.0	no
8_3Li	0.838	16	no
${}^{15}_6C$	2.45	9.77	no
${}^{16}_7N$	7.13	10.4	no
${}^{11}_4Be$	13.8	11.5	no

A.1 Spallation: SK-I/III Combined Likelihoods

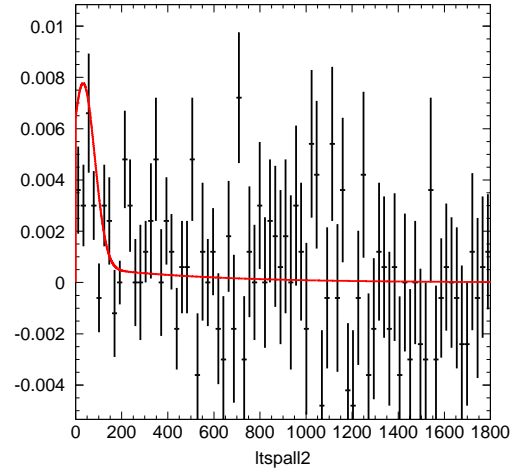
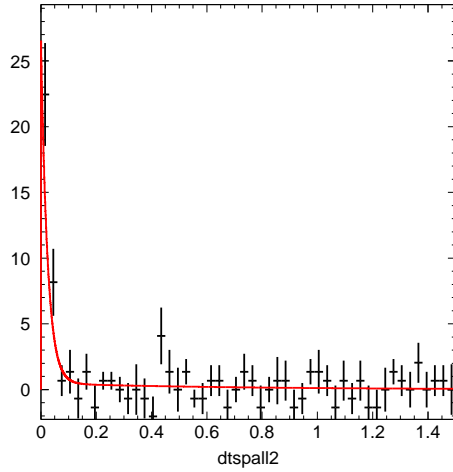


(a) SK-I/III dt spallation likelihood (red) vs SK-I/III L_{TRANS} spallation likelihood (red) vs SK-I/III spallation data > 15 MeV (black) for single through-going muons

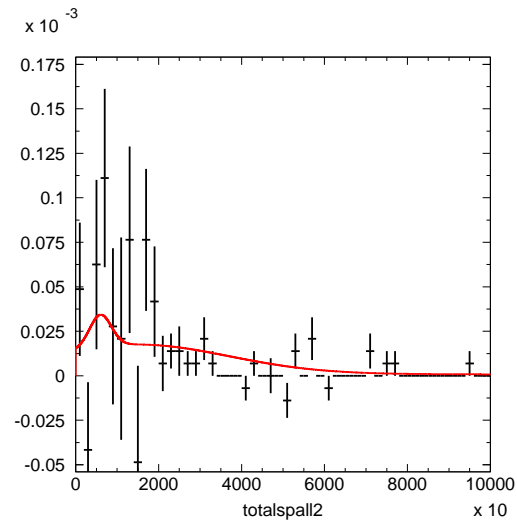
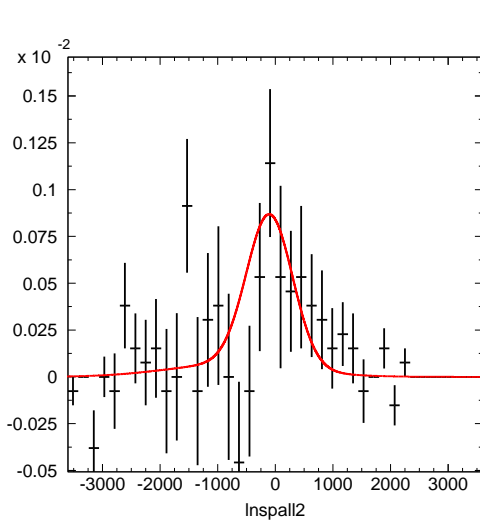


(c) SK-I/III L_{LONG} spallation likelihood (red) vs SK-I/III Q_{PEAK} spallation likelihood (red) vs SK-I/III spallation data > 15 MeV (black) for single through-going muons

Figure A.1: Single muon SK-I/III spallation likelihoods

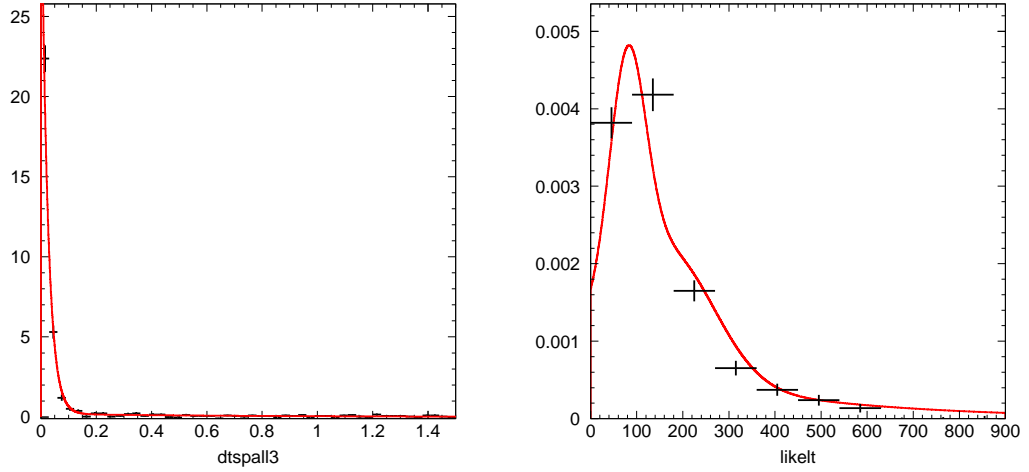


(a) SK-I/III dt spallation likelihood (red) vs SK-I/III L_{TRANS} spallation likelihood (red) vs SK-I/III spallation data > 15 MeV (black) for stopping muons

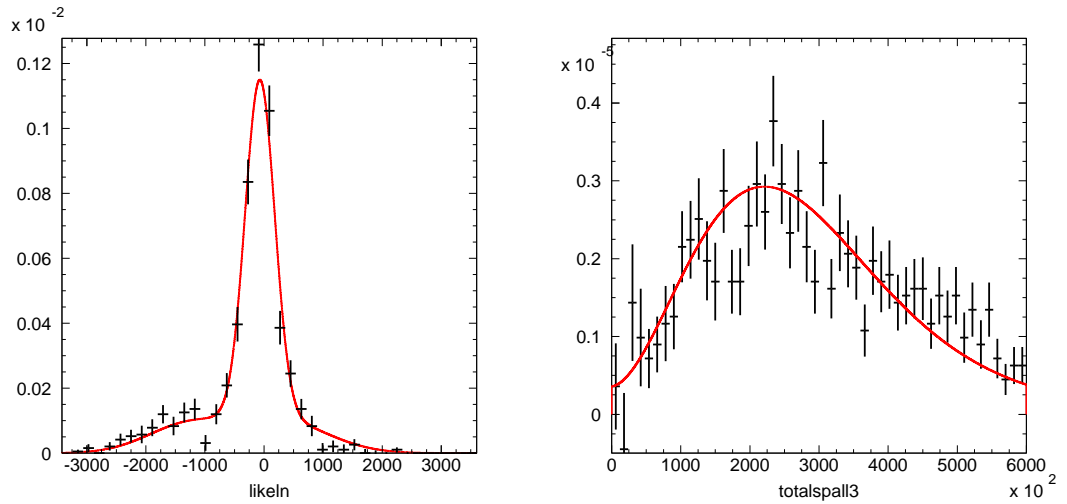


(c) SK-I/III L_{LONG} spallation likelihood (red) vs SK-I/III Q_{PEAK} spallation likelihood (red) vs SK-I/III spallation data > 15 MeV (black) for stopping muons

Figure A.2: Stopping muon SK-I/III spallation likelihoods

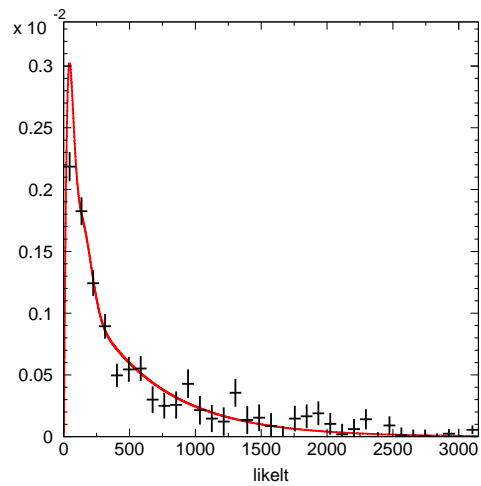
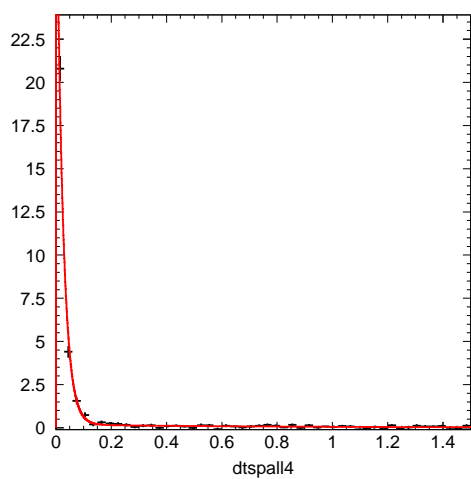


(a) SK-I/III dt spallation likelihood (red) vs SK-I/III spallation data > 15 MeV (black) for multiple muons (type 1) (b) SK-I/III L_{TRANS} spallation likelihood (red) vs SK-I/III spallation data > 15 MeV (black) for multiple muons (type 1)

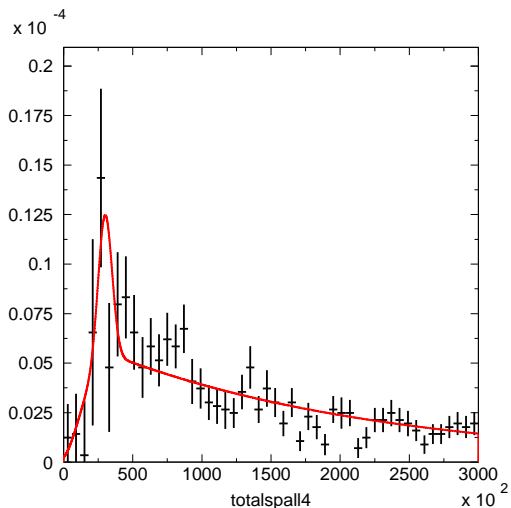
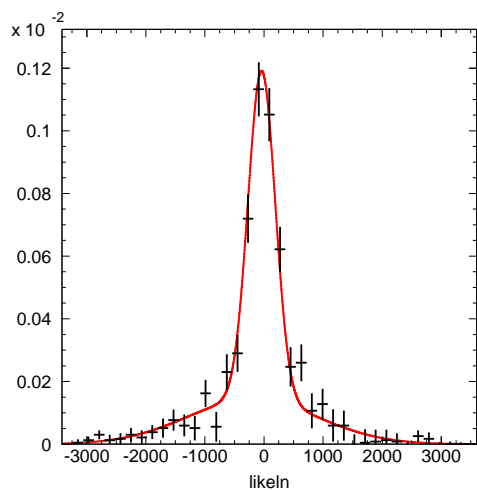


(c) SK-I/III L_{LONG} spallation likelihood (red) vs SK-I/III spallation data > 15 MeV (black) for multiple muons (type 1) (d) SK-I/III Q_{PEAK} spallation likelihood (red) vs SK-I/III spallation data > 15 MeV (black) for multiple muons (type 1)

Figure A.3: Multiple muon (type 1) SK-I/III spallation likelihoods

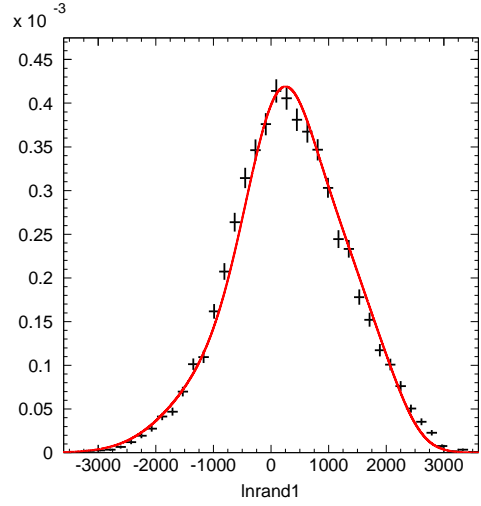
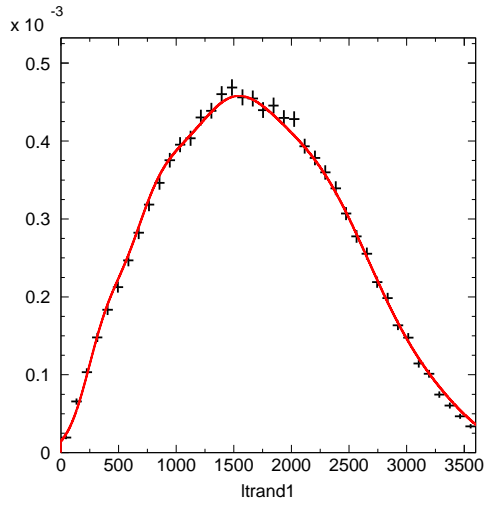


(a) SK-I/III dt spallation likelihood (red) vs SK-I/III L_{TRANS} spallation likelihood (red) vs SK-I/III spallation data > 15 MeV (black) for multiple muons (type 2)



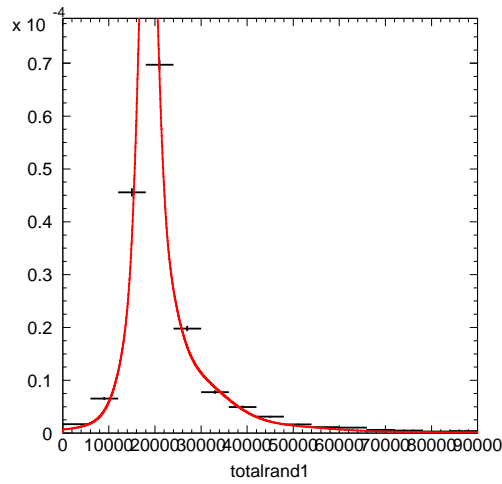
(c) SK-I/III L_{LONG} spallation likelihood (red) vs SK-I/III Q_{PEAK} spallation likelihood (red) vs SK-I/III spallation data > 15 MeV (black) for multiple muons (type 2)

Figure A.4: Multiple muon (type 2) SK-I/III spallation likelihoods



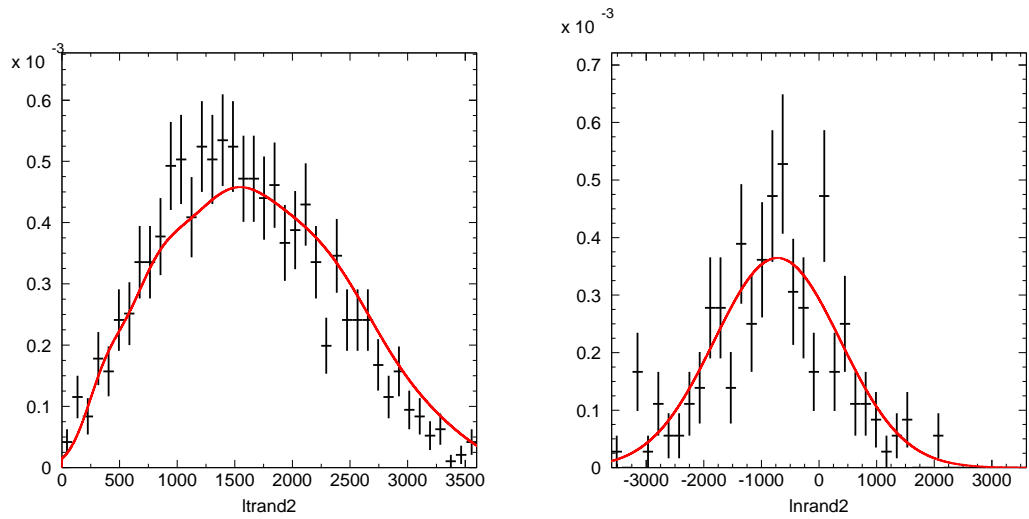
(a) SK-I/III L_{TRANS} random likelihood (red) vs SK-I/III random sample data > 15 MeV (black) for single through-going muons

(b) SK-I/III L_{LONG} random likelihood (red) vs SK-I/III random sample data > 15 MeV (black) for single through-going muons

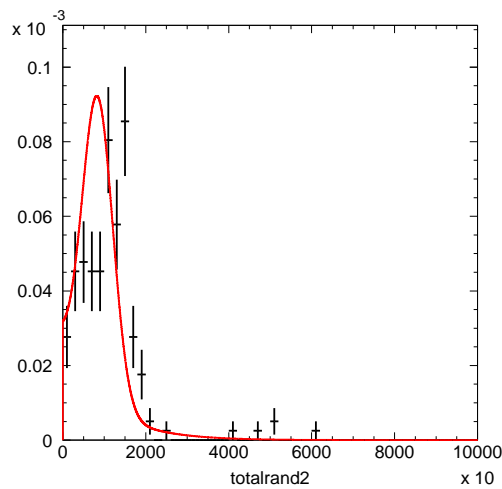


(c) SK-I/III Q_{PEAK} random likelihood (blue) vs SK-I/III random sample data > 15 MeV (black) for single through-going muons

Figure A.5: Single muon SK-I/III random likelihoods

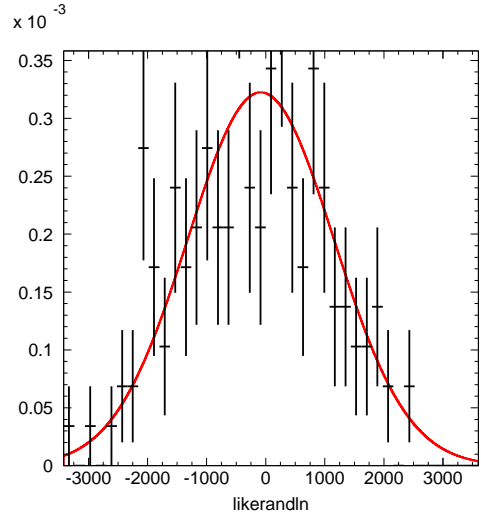
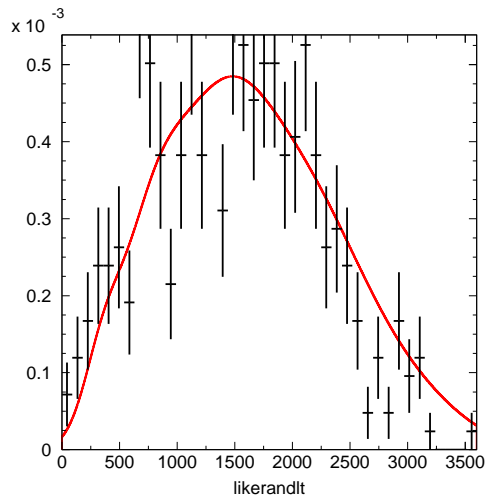


(a) SK-I/III L_{TRANS} random likelihood (red) vs SK-I/III random sample data > 15 MeV (black) for stopping muons
 (b) SK-I/III L_{LONG} random likelihood (red) vs SK-I/III random sample data > 15 MeV (black) for stopping muons



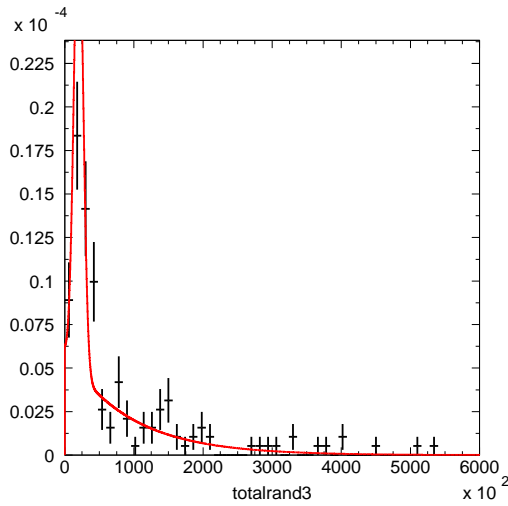
(c) SK-I/III Q_{PEAK} random likelihood (red) vs SK-I/III random sample data > 15 MeV (black) for stopping muons

Figure A.6: Stopping muon SK-I/III random likelihoods



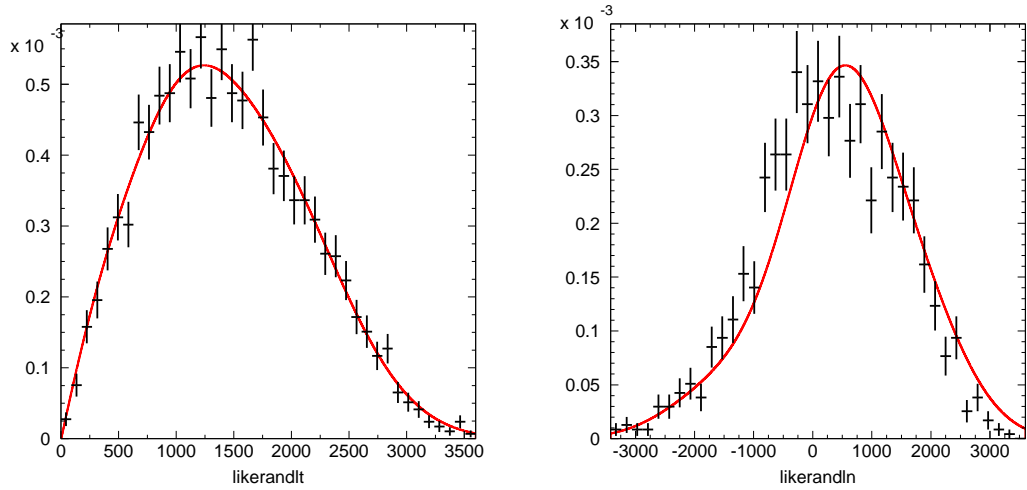
(a) SK-I/III L_{TRANS} random likelihood (red) vs SK-I/III random sample data > 15 MeV (black) for multiple muons (type 1)

(b) SK-I/III L_{LONG} random likelihood (red) vs SK-I/III random sample data > 15 MeV (black) for multiple muons (type 1)



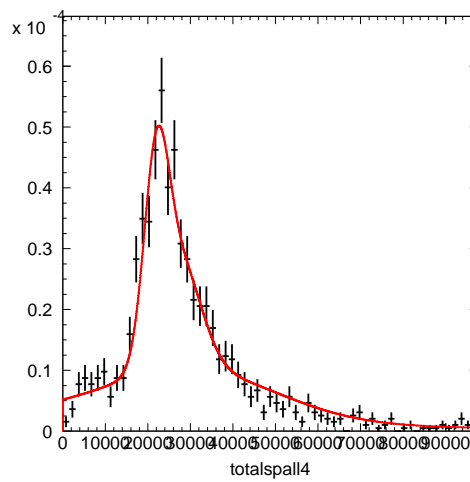
(c) SK-I/III Q_{PEAK} random likelihood (red) vs SK-I/III random sample data > 15 MeV (black) for multiple muons (type 1)

Figure A.7: Multiple muon (type 1) SK-I/III random likelihoods



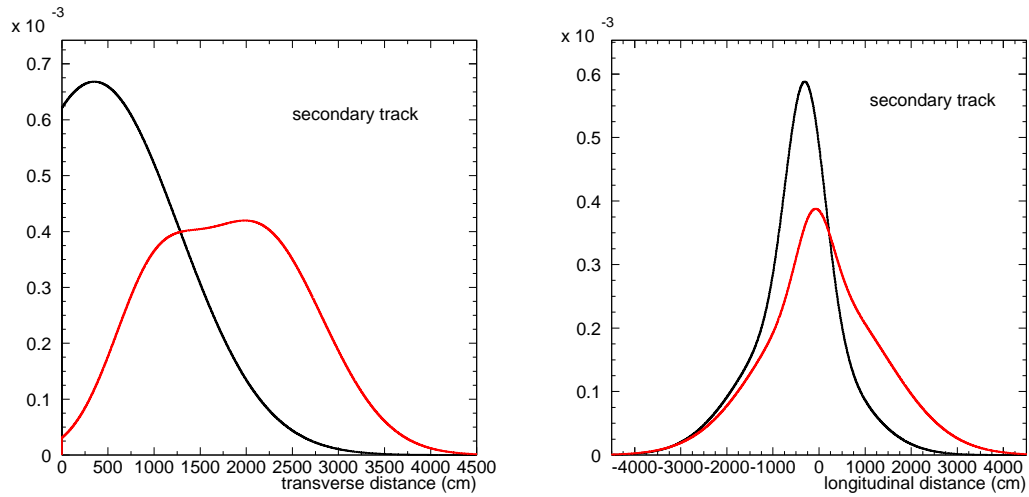
(a) SK-I/III L_{TRANS} random likelihood (red) vs SK-I/III random sample data > 15 MeV (black) for multiple muons (type 2)

(b) SK-I/III L_{LONG} random likelihood (red) vs SK-I/III random sample data > 15 MeV (black) for multiple muons (type 2)

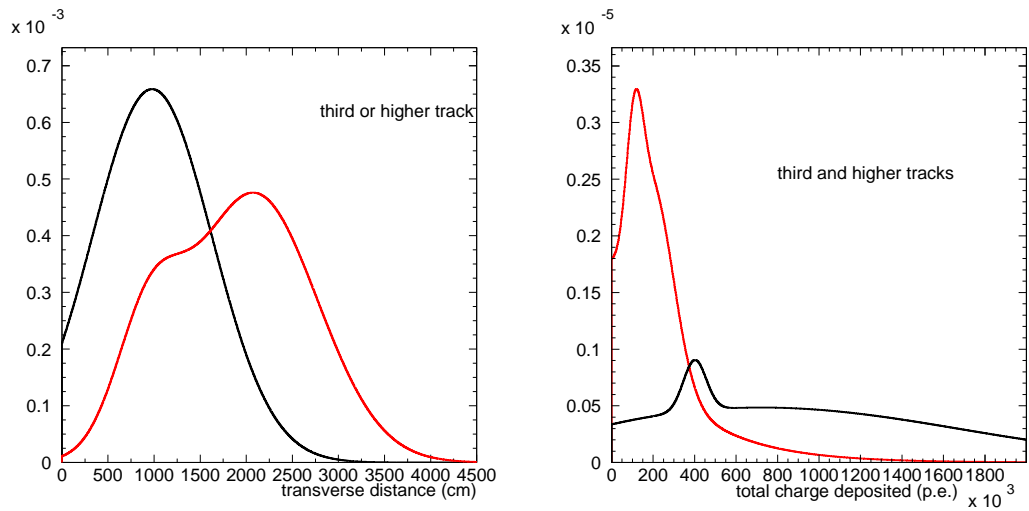


(c) SK-I/III Q_{PEAK} random likelihood (red) vs SK-I/III random sample data > 15 MeV (black) for multiple muons (type 2)

Figure A.8: Multiple muon (type 2) SK-I/III random likelihoods



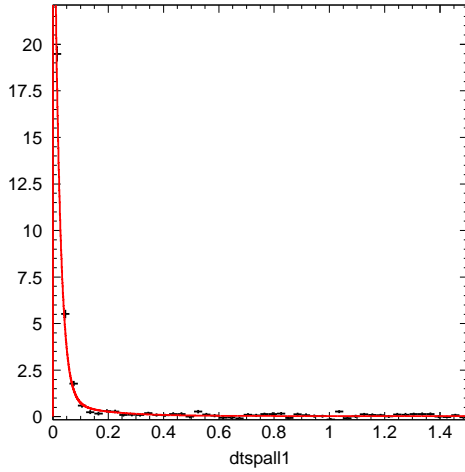
(a) SK-I/III L_{TRANS} random likelihood (red) vs SK-I/III spallation likelihood (black) for secondary tracks. (b) SK-I/III L_{LONG} random likelihood (red) vs SK-I/III spallation likelihood (black) for secondary muon tracks.)



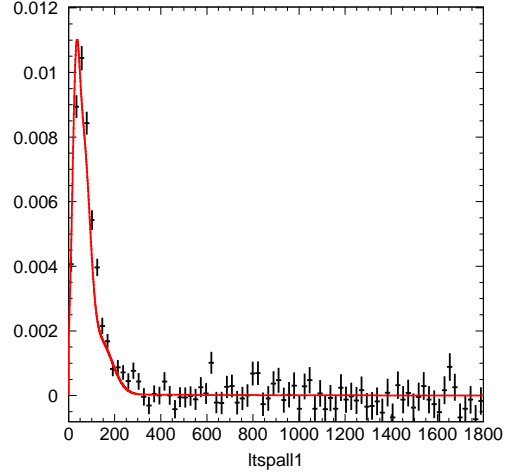
(c) SK-I/III L_{TRANS} random likelihood (red) vs SK-I/III spallation likelihood (black) for third and higher order tracks. (d) SK-I/III Q_μ random likelihood (red) vs SK-I/III likelihood (black) for third and higher order tracks.

Figure A.9: Multiple track SK-I/III likelihoods. In all cases black shows the spallation likelihood, and red the random sample.

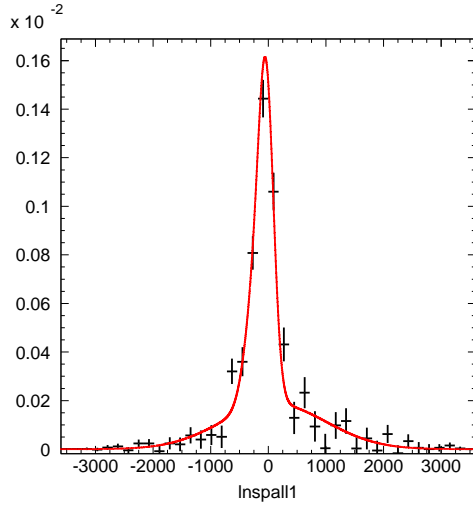
A.2 SK-II likelihoods



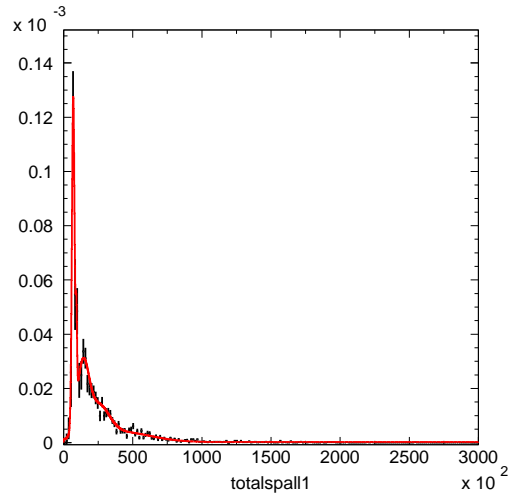
(a) SK-II dt spallation likelihood (red) vs SK-II spallation data > 15 MeV (black) for single through-going muons



(b) SK-II L_{TRANS} spallation likelihood (red) vs SK-II spallation data > 15 MeV (black) for single through-going muons

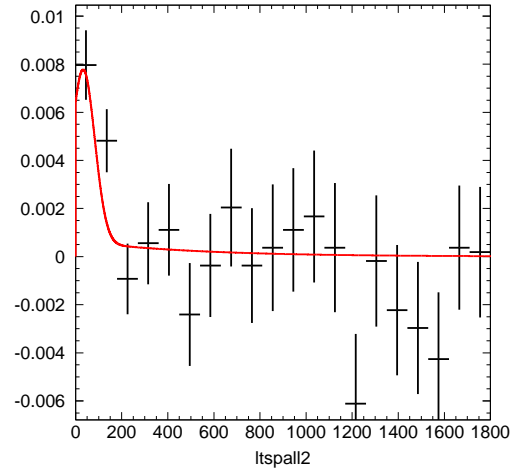
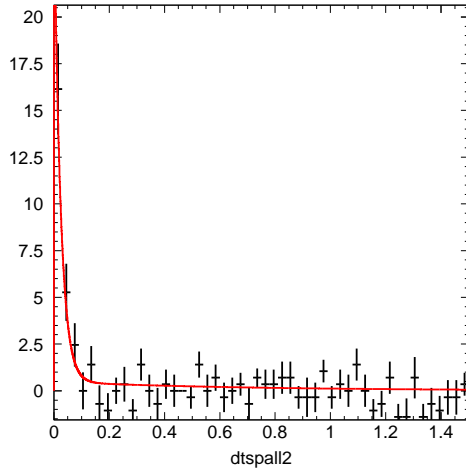


(c) SK-II L_{LONG} spallation likelihood (red) vs SK-II spallation data > 15 MeV (black) for single through-going muons



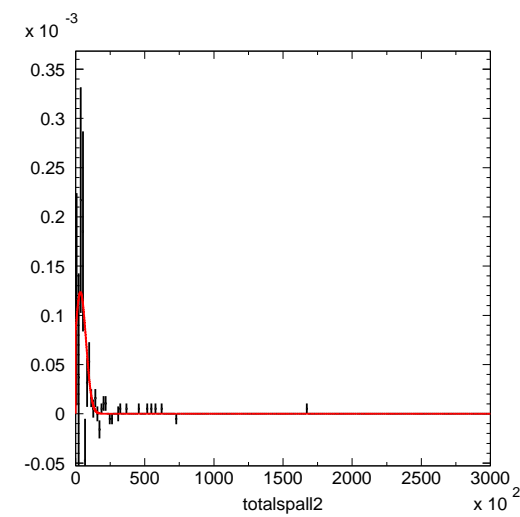
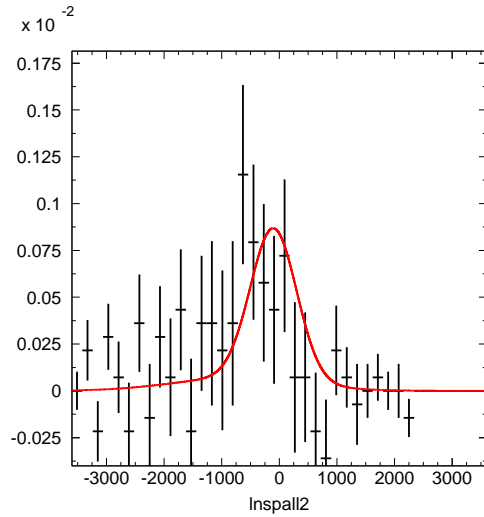
(d) SK-II Q_{PEAK} spallation likelihood (blue) vs SK-II spallation data > 15 MeV (black) for single through-going muons

Figure A.10: Single muon SK-II spallation likelihoods



(a) SK-II dt spallation likelihood (red) vs SK-II spallation data > 15 MeV (black) for stopping muons

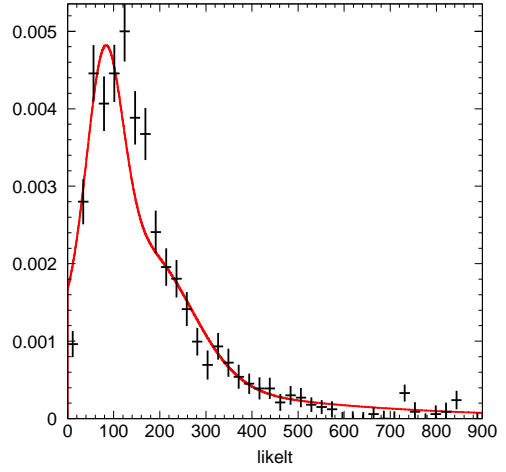
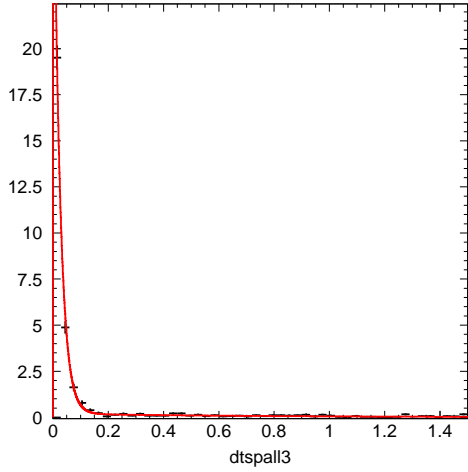
(b) SK-II L_{TRANS} spallation likelihood (red) vs SK-II spallation data > 15 MeV (black) for stopping muons



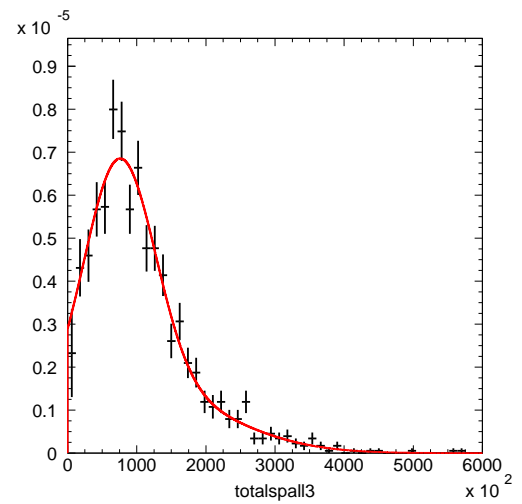
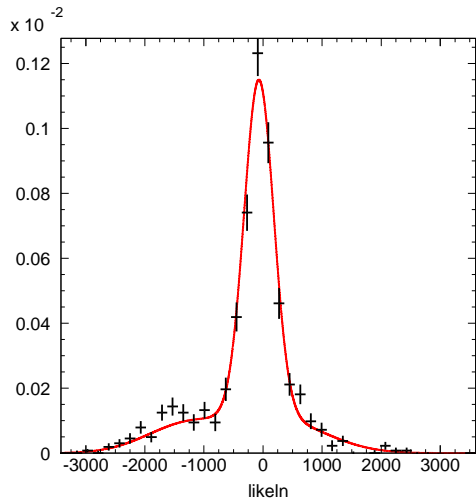
(c) SK-II L_{LONG} spallation likelihood (red) vs SK-II spallation data > 15 MeV (black) for stopping muons

(d) SK-II Q_{PEAK} spallation likelihood (red) vs SK-II spallation data > 15 MeV (black) for stopping muons

Figure A.11: Stopping muon SK-II spallation likelihoods

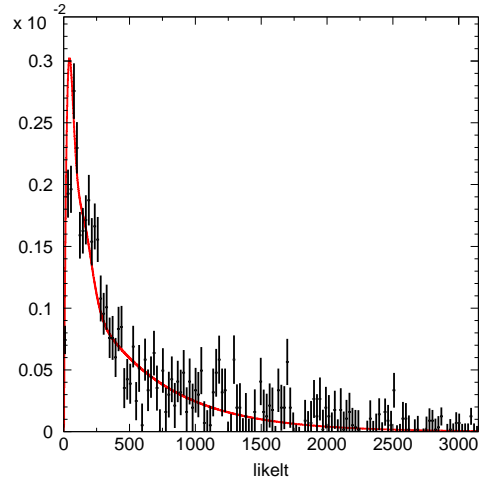
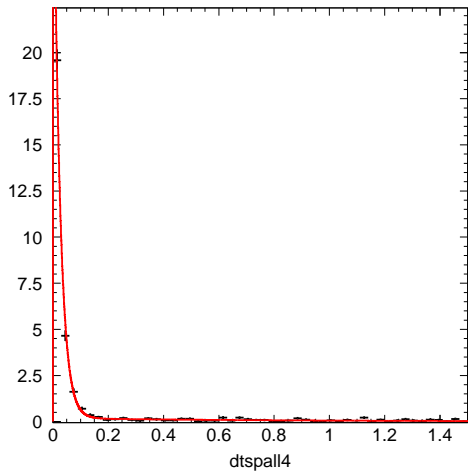


(a) SK-II dt spallation likelihood (red) vs SK-II spallation data > 15 MeV (black) for multiple muons (type 1) (b) SK-II L_{TRANS} spallation likelihood (red) vs SK-II spallation data > 15 MeV (black) for multiple muons (type 1)

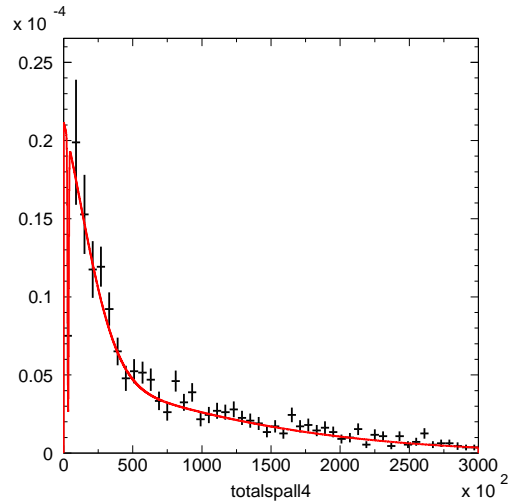
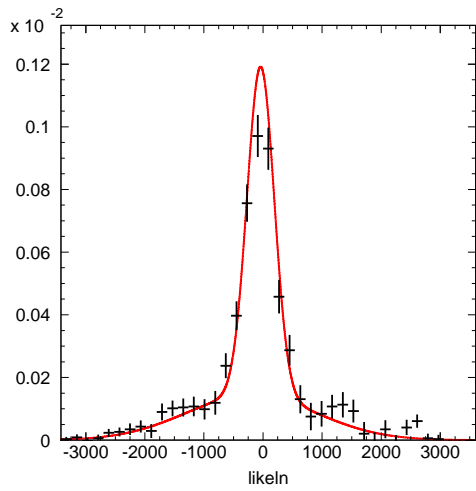


(c) SK-II L_{LONG} spallation likelihood (red) vs SK-II spallation data > 15 MeV (black) for multiple muons (type 1) (d) SK-II Q_{PEAK} spallation likelihood (red) vs SK-II spallation data > 15 MeV (black) for multiple muons (type 1)

Figure A.12: Multiple muon (type 1) SK-II spallation likelihoods

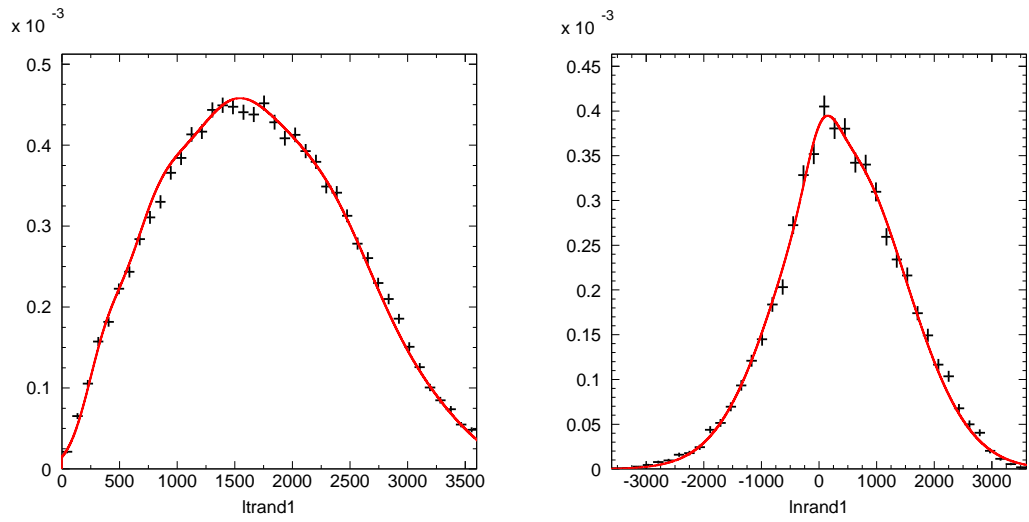


(a) SK-II dt spallation likelihood (red) vs SK-II spallation data > 15 MeV (black) for multiple muons (type 2) (b) SK-II L_{TRANS} spallation likelihood (red) vs SK-II spallation data > 15 MeV (black) for multiple muons (type 2)

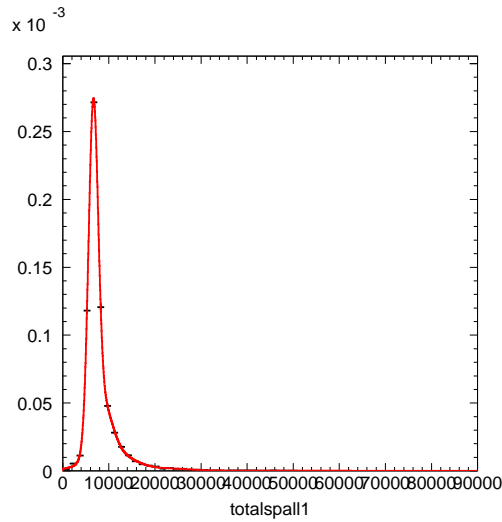


(c) SK-II L_{LONG} spallation likelihood (red) vs SK-II spallation data > 15 MeV (black) for multiple muons (type 2) (d) SK-II Q_{PEAK} spallation likelihood (red) vs SK-II spallation data > 15 MeV (black) for multiple muons (type 2)

Figure A.13: Multiple muon (type 2) SK-II spallation likelihoods

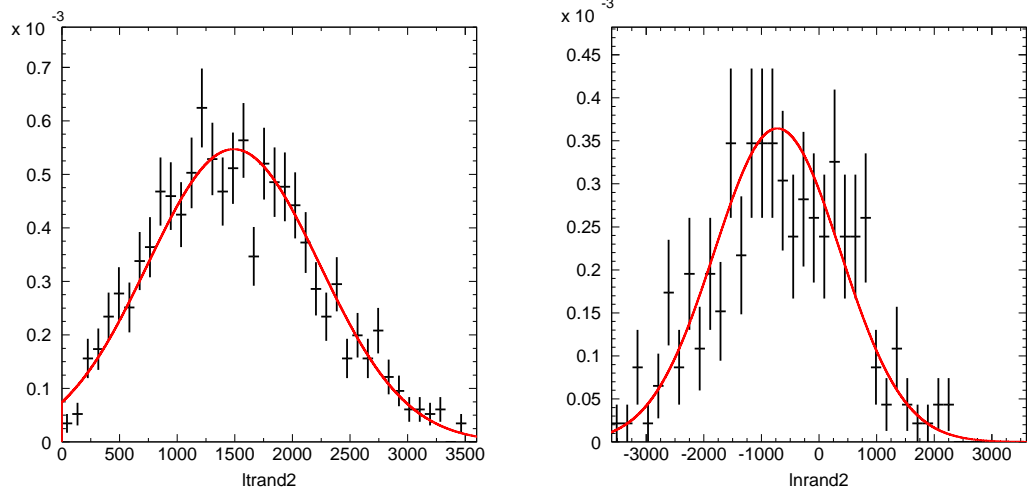


(a) SK-II L_{TRANS} random likelihood (red) vs SK-II random sample data > 15 MeV (black) for single through-going muons
 (b) SK-II L_{LONG} random likelihood (red) vs SK-II random sample data > 15 MeV (black) for single through-going muons

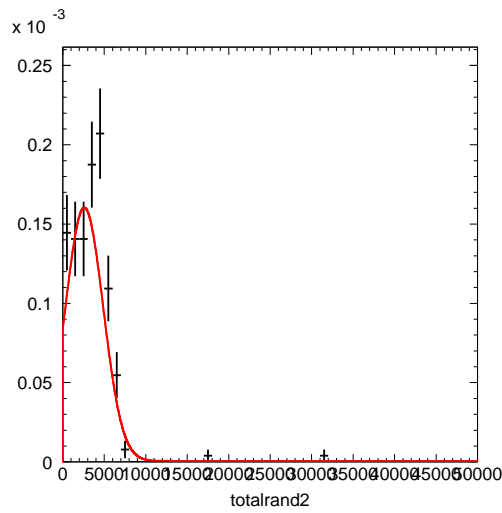


(c) SK-II Q_{PEAK} random likelihood (blue) vs SK-II random sample data > 15 MeV (black) for single through-going muons

Figure A.14: Single muon SK-II random likelihoods

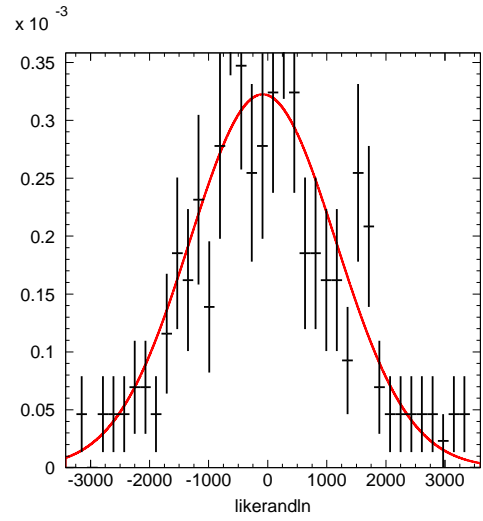
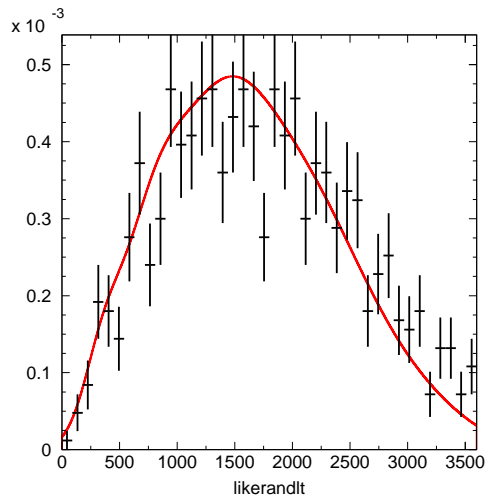


(a) SK-II L_{TRANS} random likelihood (red) vs SK-II random sample data > 15 MeV (black) for stopping muons
 (b) SK-II L_{LONG} random likelihood (red) vs SK-II random sample data > 15 MeV (black) for stopping muons

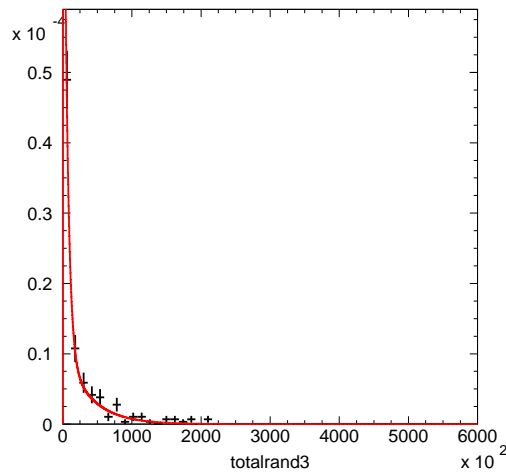


(c) SK-II Q_{PEAK} random likelihood (red) vs SK-II random sample data > 15 MeV (black) for stopping muons

Figure A.15: Stopping muon SK-II random likelihoods

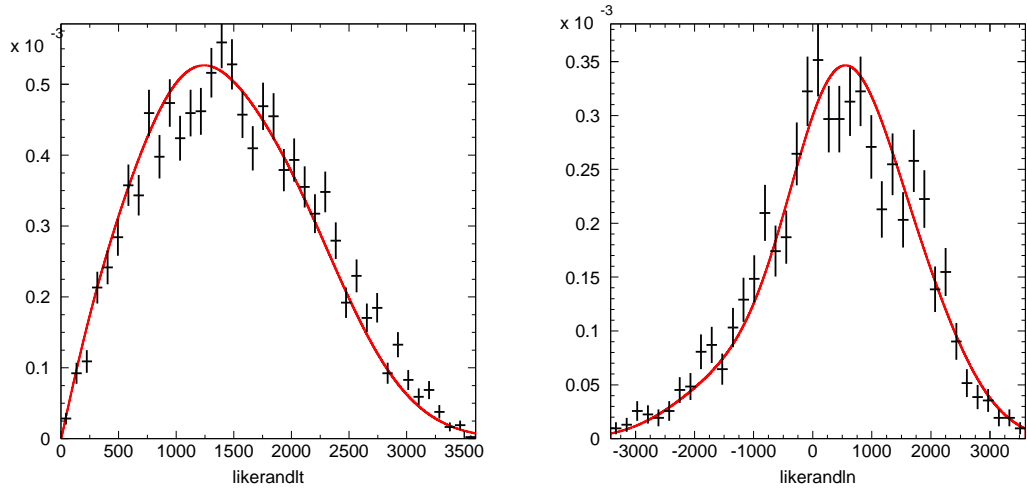


(a) SK-II L_{TRANS} random likelihood (red) vs SK-II random sample data > 15 MeV (black) for multiple muons (type 1) (b) SK-II L_{LONG} random likelihood (red) vs SK-II random sample data > 15 MeV (black) for multiple muons (type 1)

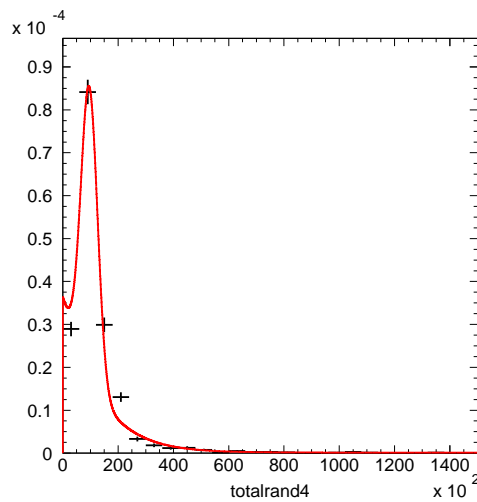


(c) SK-II Q_{PEAK} random likelihood (red) vs SK-II random sample data > 15 MeV (black) for multiple muons (type 1)

Figure A.16: Multiple muon (type 1) SK-II random likelihoods

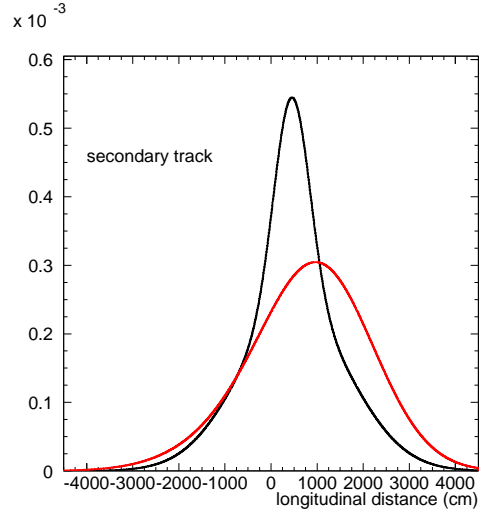
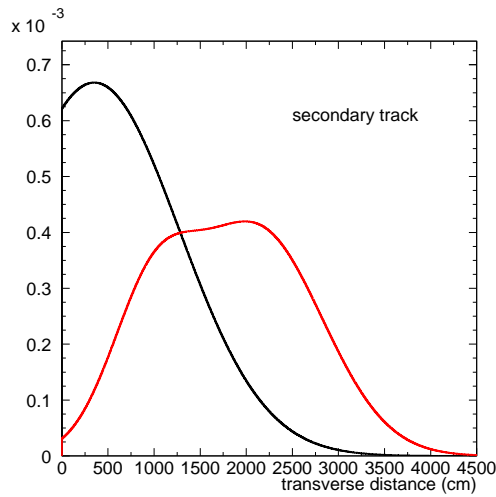


(a) SK-II L_{TRANS} random likelihood (red) vs SK-II random sample data > 15 MeV (black) for multiple muons (type 2) (b) SK-II L_{LONG} random likelihood (red) vs SK-II random sample data > 15 MeV (black) for multiple muons (type 2)

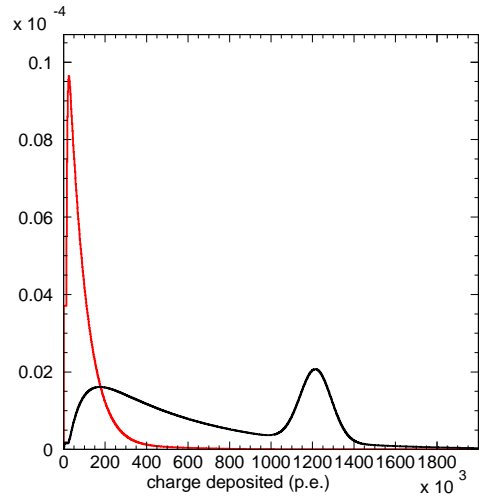
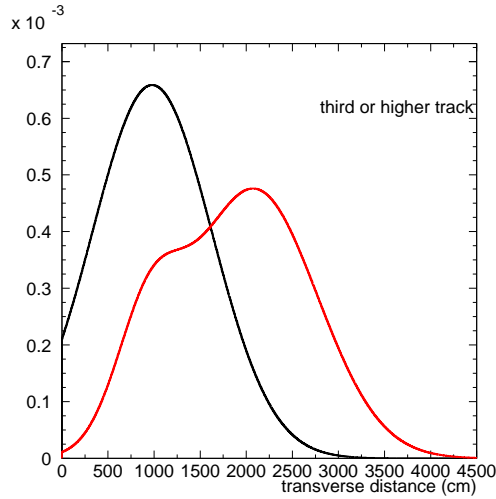


(c) SK-II Q_{PEAK} random likelihood (red) vs SK-II random sample data > 15 MeV (black) for multiple muons (type 2)

Figure A.17: Multiple muon (type 2) SK-II random likelihoods



(a) SK-II L_{TRANS} random likelihood (red) vs SK-II spallation likelihood (black) for secondary tracks. (b) SK-II L_{LONG} random likelihood (red) vs SK-II spallation likelihood (black) for secondary muon tracks.)



(c) SK-II L_{TRANS} random likelihood (red) vs SK-II spallation likelihood (black) for third and higher order tracks. (d) SK-II Q_{μ} random likelihood (red) vs SK-II spallation likelihood (black) for third and higher order tracks.

Figure A.18: Multiple track SK-II likelihoods. In all cases black shows the spallation likelihood, and red the random sample.

A.3 Spallation: Algorithm

The full spallation cut is multi-branched and algorithmically complicated. This section is an attempt to describe it in a complete fashion. The description will be of the SK-I/III combined cut, with SK-II information in parenthesis when appropriate.

The muons are divided into four categories by Muboy: Type 1 muons are simply single muons that travel through the detector ('singles'). Type 2 muons are single muons that stop in the detector ('stoppers'). Type 3 muons are those which Muboy believes to be multiple muon bundles, but for which it can not fit more than a single muon track. Type 4 muons are multiple muons for which Muboy can find and fit more than one track. Type 5 muons are 'corner clippers', which are of very low track length and deposit very little light in the detector. Finally, Type 0 muons are those which Muboy fails to fit at all ('misfits').

The spallation cut utilizes a number of variables. The first four comprise the likelihoods: dt (time difference from relic candidate to muon in seconds); L_{TRANS} (transverse distance from reconstructed muon track to relic candidate vertex in cm); L_{LONG} (reconstructed distance between where relic candidate falls 'along' the muon track and where spallation is predicted by a peak in the muon dE/dx profile in cm); and Q_{PEAK} (the sum of the nine dE/dx bins surrounding the dE/dx peak in p.e.; nine bins is 4.5 m). Also utilized is the total muon charge deposited in the detector in p.e. (Q_μ), the number of empty dE/dx bins between the first and last bin ($emptyfrac$), which is an indication of dE/dx profile quality, and the goodnesses of the muon fits: $Good_{Muboy}$ and $Good_{BFF}$ for the Muboy and BFF fitters respectively. Finally, for muon bundles, the number of reconstructed tracks is considered (N_{TRACKS}).

Spallation likelihood values are mostly determined from the PDFs of the four spallation variables for the appropriate muon type (PDF_{S1} for dt , PDF_{S2} for L_{TRANS} , PDF_{S3} for L_{LONG} , and PDF_{S4} for Q_{PEAK}), as well as the four random sample PDFs for the same variables (PDF_{R1} through PDF_{R4}). The PDFs (shown in Appendix A.1

(A.2)) can be combined in more than one way. The standard (Type A) likelihood is simply as follows: $L_{SPALL} = Ln(\prod_{i=1}^4 \frac{PDF_{S_i}}{PDF_{R_i}})$, the natural logarithm of the product of the ratios of spallation PDF to random sample PDF for the four variables. Unless otherwise stated, this spallation likelihood is used.

In some rarer cases, other likelihood formulations are used. When the dE/dx information is found to be untrustworthy, the variables from the dE/dx profile are not used, and the likelihood becomes simply: $L_{SPALL}^2 = Ln(\frac{PDF_{S1}}{PDF_{R1}} \times \frac{PDF_{S2}}{PDF_{R2}})$. Multiple muons also have special likelihoods. Finally, in the case of three or more muon tracks, each track beyond the second is considered without utilizing dE/dx information. However, for these cases Q_μ is utilized as a third variable, and the likelihood becomes: $L_{SPALL}^3 = Ln(\frac{PDF_{S1}}{PDF_{R1}} \times \frac{PDF_{S2}}{PDF_{R2}}) \times \frac{PDF_{SQ\mu}}{PDF_{RQ\mu}}$.

Lastly, the cut is different for relic candidate energy 16-18 MeV (17.5-20 MeV SK-II), which will be denoted as < 18 MeV, and for events 18-24 MeV (20-26 MeV SK-II), which will be denoted > 18 MeV.

Before the spallation likelihood is even considered, there are a number of precuts. First, the muon sample is checked for ‘ringing’. This is an electronics effect where after a high charge muon, many phantom muons will appear shortly following in time due to pulse reflections and electronics saturation. Any muons following a muon with $Q_\mu > 90,000$ p.e. and within 20 μs are eliminated from the muon sample.

Next a detector veto is instituted after the muons that deposit the most light in the detector, as muons in the upper tail end of the Q_μ distribution are far more likely to cause spallation than other muons and are comparatively rare. This veto is for 4 seconds after muons with $Q_\mu > 1,000,000$ and 8 seconds after muons with $Q_\mu > 2,000,000$.

Additionally, a cut is instituted that is a combination of Q_μ , dt, and N_{TRACKS} , which includes all muon types, which have $N_{TRACKS} = 1$. This cut is motivated by a combination of how not only do muons with high Q_μ tend to make more spallation,

but muons with many tracks or poor $Good_{Muboy}$ have less trustworthy tracks. An incorrectly fit muon track is more likely to cause improper correlations and allow a spallation event to slip through, which we wish to avoid. This cut looks for any events for which the following condition is met: $(N_{TRACKS} \times 0.1 + 0.1) < Good_{Muboy}$. If this condition is met, then any relic candidates with the following correlations are eliminated: 1) $Q_\mu > 400,000$ and $dt < 0.2$; 2) $Q_\mu > 600,000$ and $dt < 1$; or 3) $Q_\mu > 750,000$ and $dt < 5$.

A further special consideration is given to muons with $N_{TRACKS} = 10$, as 10 is the highest number of tracks Muboy will attempt to fit, and so this is actually a pile up of $N_{TRACKS} = 10$ or higher. Furthermore these muons have the least trustworthy muon tracks, and are the most likely to create spallation. They are also quite rare. For such muons, a full detector veto of 1 second is implemented.

For all muons an initial likelihood is calculated for the first (and usually only) track. This is the four variable standard likelihood described above unless $emptyfrac > 0.3$ or the peak of the dE/dx profile is found to occur at a point farther from the entry position than the muon track length. In these cases there is something wrong with the dE/dx profile, and the information is not trusted, so the two variable likelihood L_{SPALL}^2 is used instead.

For all muon types, for events $E < 18$ MeV, all events with $dt < 0.01$ and $L_{TRANS} < 500$ were rejected.

From here the cut branches depending on muon type and relic candidate energy.

For Muboy **misfits** (Type 6 muons), a simple detector veto was implemented, for 1.5 seconds < 18 MeV and 1 second > 18 MeV.

Corner clippers (Type 5 muons) were not found to cause any spallation.

Stoppers (Type 2 muons) are cut as follows: for $E < 18$ MeV, if $L_{SPALL} > 0.5$ or $dt < 0.02$ the event is rejected. For $E > 18$ MeV, if $L_{SPALL} > 3$ or $dt < 0.01$ the event is rejected.

The bulk of the muons are **singles** (Type 1). All correlations to singles with $Good_{Muboy} > 0.4$ and the following properties are rejected: for $E < 18$ MeV, if $L_{SPALL} > 3$ and $L_{TRANS} < 600$, or if $L_{TRANS} < 150$ and $dt < 7$. For $E > 18$ MeV, if $L_{SPALL} > 4.2$, or if $L_{TRANS} < 100$ and $dt < 7$, or if $L_{TRANS} < 300$ and $dt < 0.1$.

For singles with $Good_{Muboy} < 0.4$ the track isn't trusted. Just in case the Muboy information is good, all events (any relic candidate energy) with $L_{SPALL} > 3$ are rejected. However, the BFF muon fit is also checked. The distance variables L_{TRANS} and L_{LONG} are recalculated using the BFF fit information, and a new likelihood obtained. If this new $L_{SPALL} > 3$, the event is rejected. $Good_{BFF}$ is also checked; if it is < 0.3 , the BFF fit isn't trusted either, and all events that have survived to this point with $dt < 2$ are rejected.

For **multiple muons with only one fit track**, the following events are rejected: for $E < 18$ MeV, if $L_{SPALL} > -1.5$ or $dt < 0.01$; for $E > 18$ MeV, if $L_{SPALL} > -0.5$ or $dt < 0.001$.

Lastly, for **multiple muons with many fit tracks**, each track is considered as a separate muon. The primary track uses the standard PDFs such as shown in Fig. A.4 (A.13). The secondary track is separately tuned and uses the distance PDFs shown in Fig. A.9 (A.18). For tracks three and above, the special likelihood L_{SPALL}^3 is used, which is also separately tuned and uses Q_μ instead of the dE/dx variables. These PDFs are also shown in Fig. A.9 (A.18). All these likelihoods use the same dt PDF.

The cut values are as follows: first, any event with $dt < 0.1$ is rejected. For the primary track the event is rejected if: $dt < 1$ and $L_{TRANS} < 400$ (all energies); or if $L_{SPALL} > 2$ for $E > 18$ MeV, or $L_{SPALL} > 0.9$ for $E < 18$ MeV. For the secondary track, the event is cut if $L_{SPALL} > 2$ for $E > 18$ MeV, or if $L_{SPALL} > 0.5$ for $E < 18$ MeV. For the third and higher tracks, the event is cut if $L_{SPALL}^3 > 2$ for $E > 18$ MeV, or if $L_{SPALL}^3 > 1$ for $E < 18$ MeV.

B Appendix B - spectral PDFs

B.1 SRN PDFs

Shown here are the PDFs used to represent the SRN spectrum for various models in the signal region. Included in the plots are spallation and solar inefficiencies, which gives rise to the sawtooth shape below 24 MeV. The low and high Cherenkov angle PDFs are not shown as they are entirely negligible (although I fit and used PDFs from the MC for the sidebands as well). The neutrino temperature formulation is separated from the other five models for convenience.

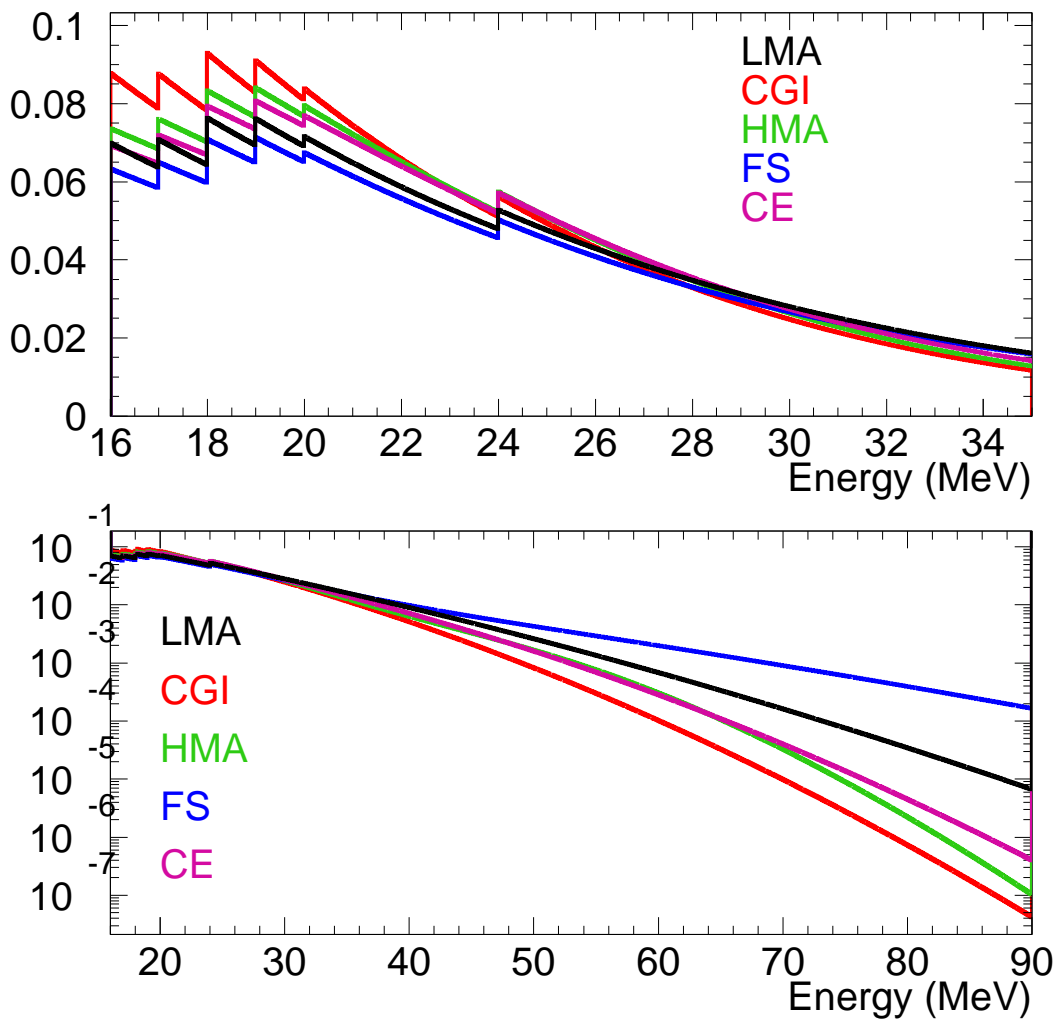


Figure B.19: SK-I SRN PDFs for five models in the signal region. Solar and spallation inefficiencies are applied. The PDF is normalized to 1 between 16 and 90 MeV, minus a tiny amount that falls into the sidebands ($\sim 0.5\%$).

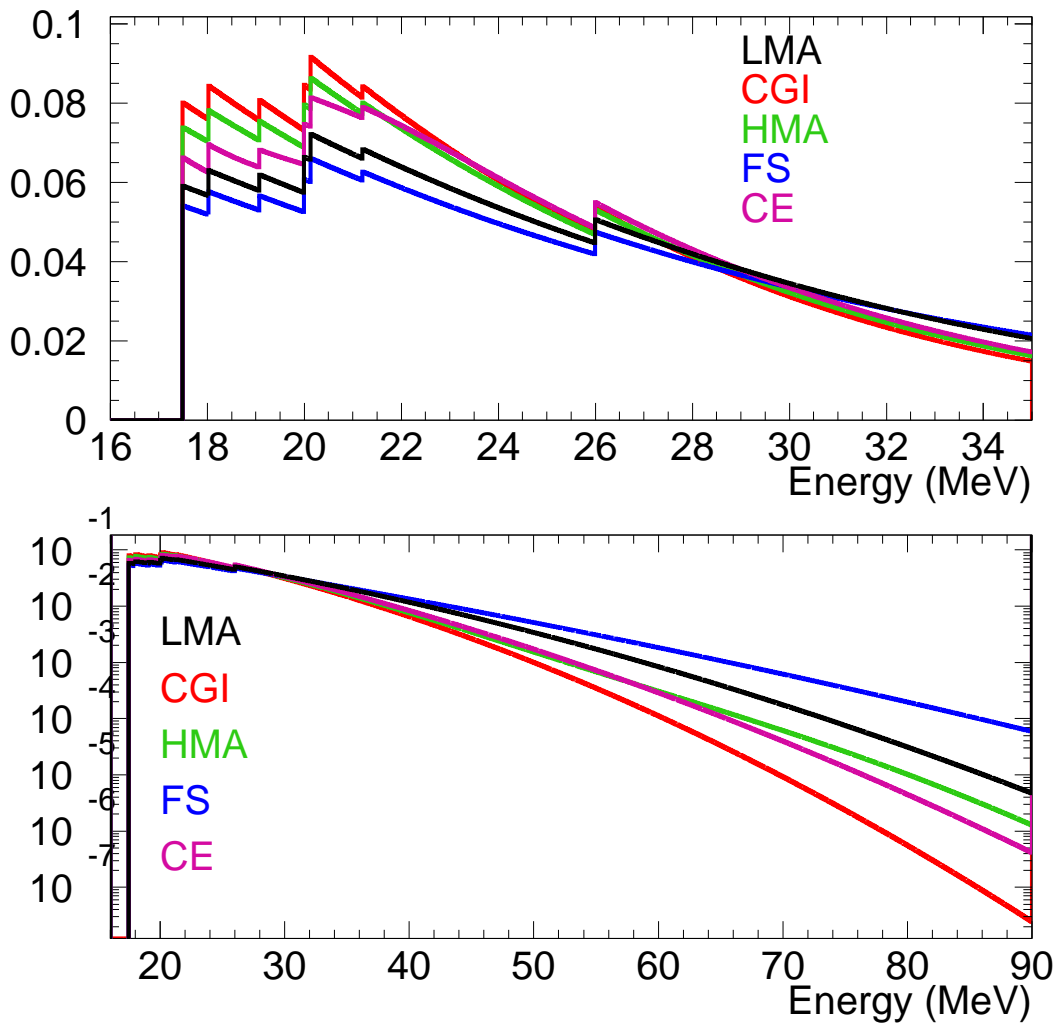


Figure B.20: SK-II SRN PDFs for five models in the signal region. Solar and spallation inefficiencies are applied. The PDF is normalized to 1 between 16 and 90 MeV, minus a tiny amount that falls into the sidebands ($\sim 1\%$).

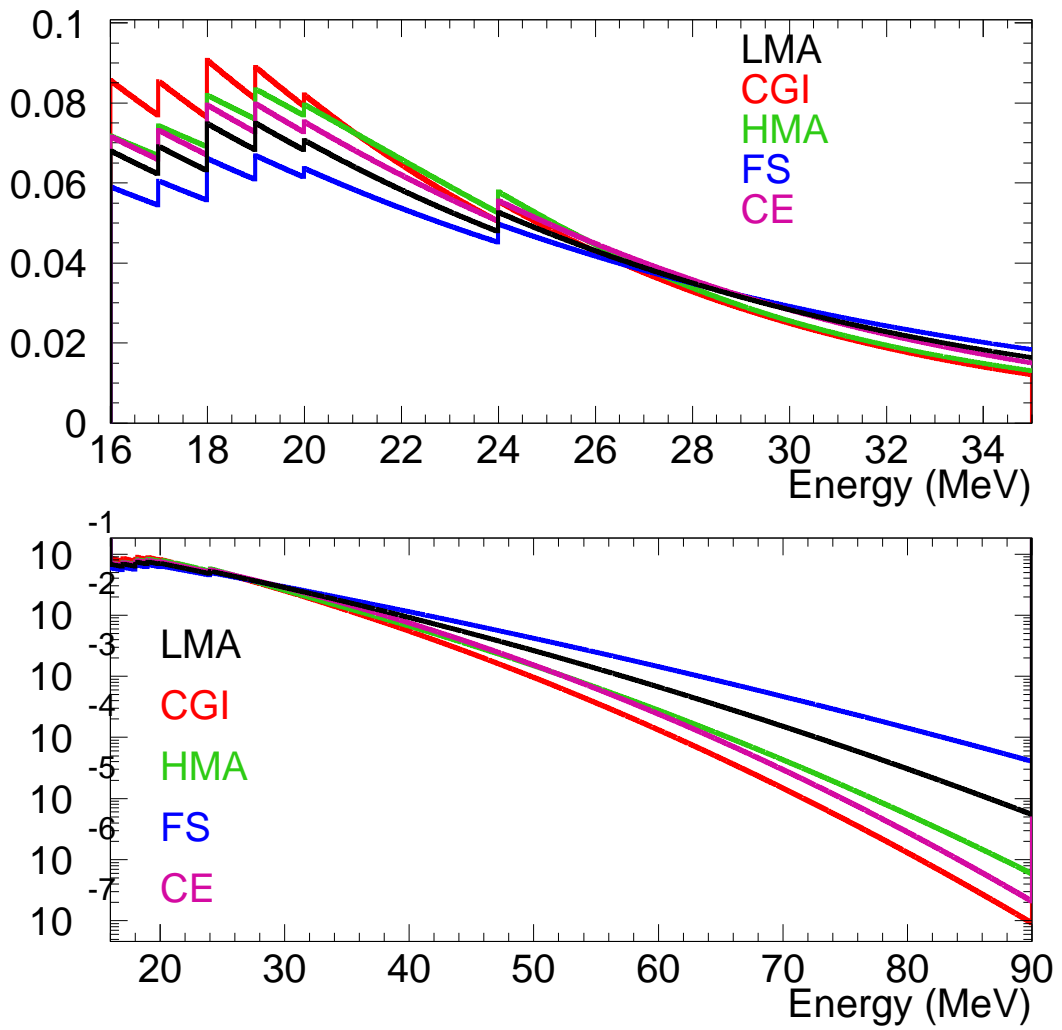


Figure B.21: SK-III SRN PDFs for five models in the signal region. Solar and spallation inefficiencies are applied. The PDF is normalized to 1 between 16 and 90 MeV, minus a tiny amount that falls into the sidebands ($\sim 0.5\%$).

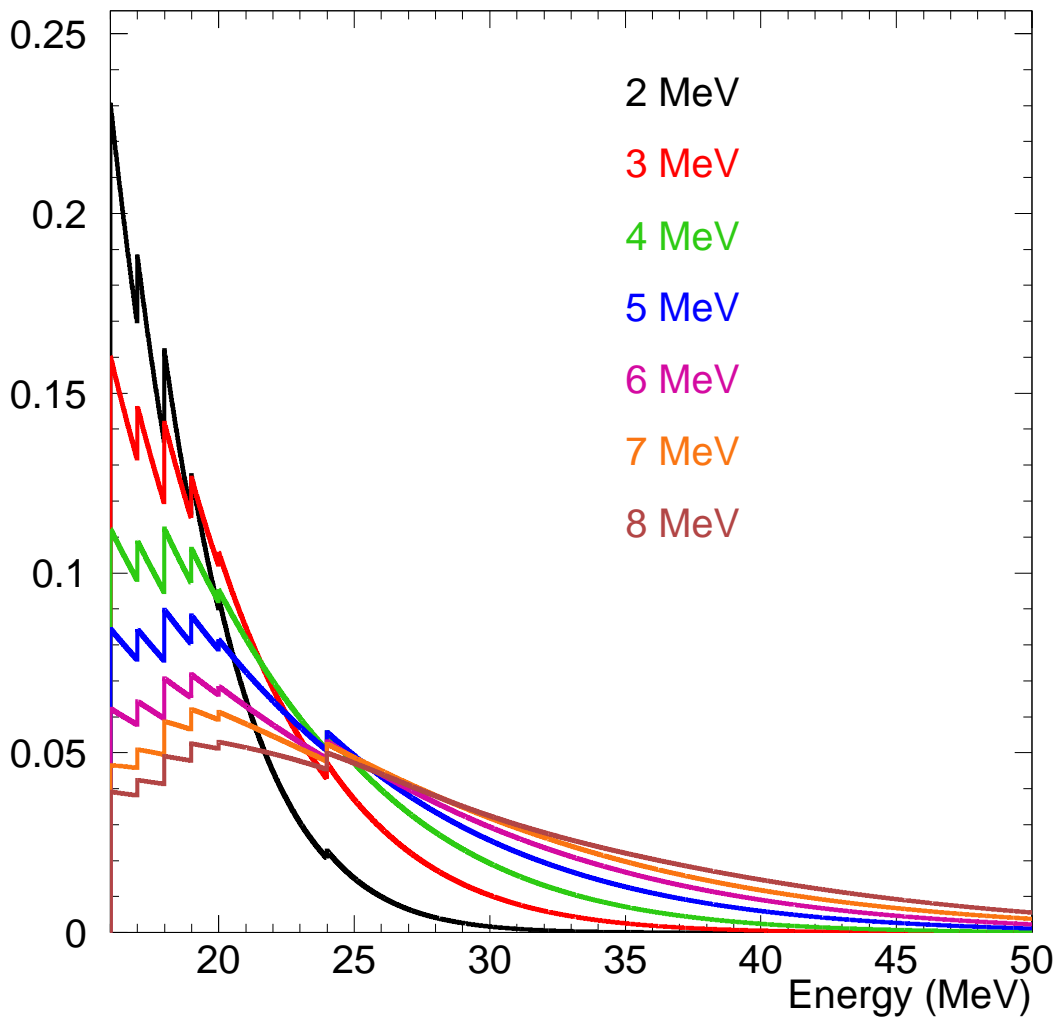


Figure B.22: SK-I SRN PDFs for various neutrino temperatures in the signal region. Solar and spallation inefficiencies are applied. The PDF is normalized to 1 between 16 and 90 MeV, minus a tiny amount that falls into the sidebands ($\sim 0.5\%$).

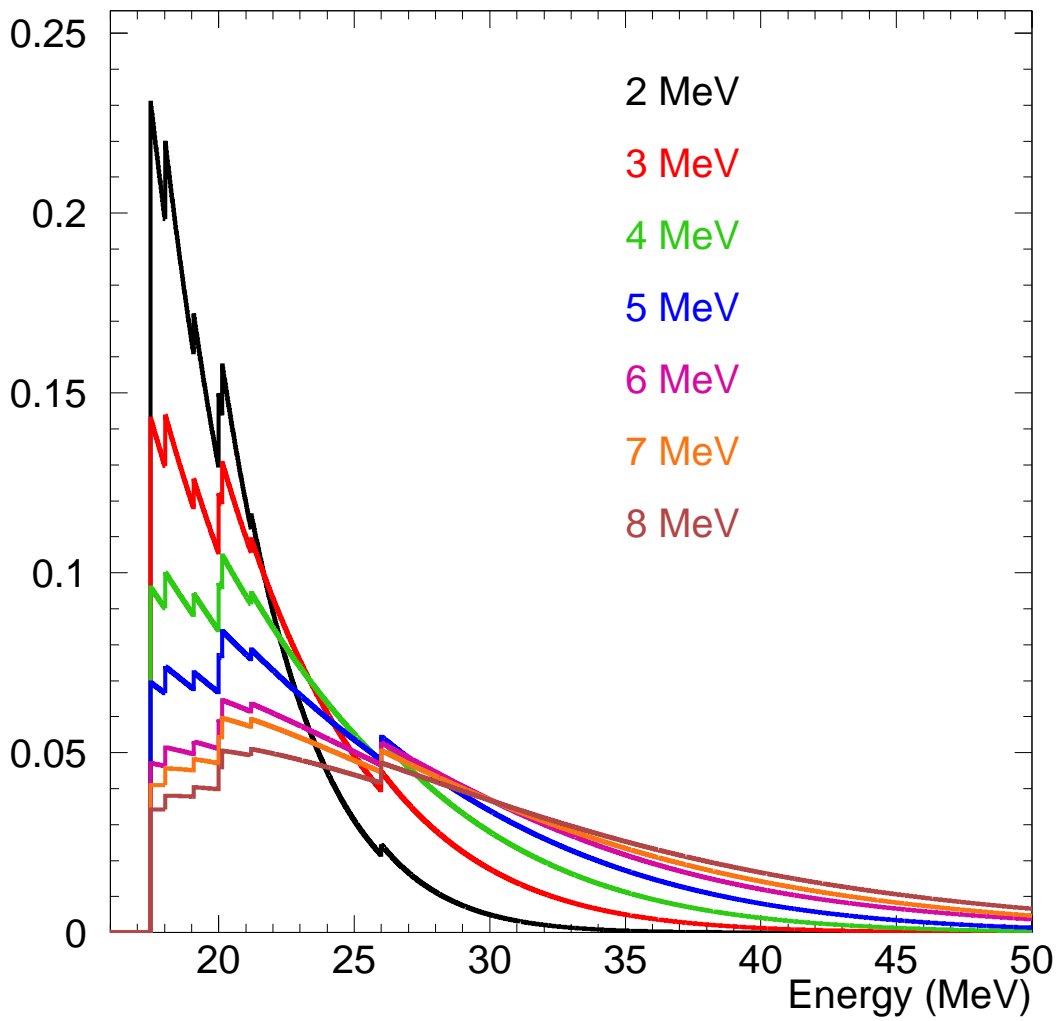


Figure B.23: SK-II SRN PDFs for various neutrino temperatures in the signal region. Solar and spallation inefficiencies are applied. The PDF is normalized to 1 between 16 and 90 MeV, minus a tiny amount that falls into the sidebands ($\sim 1\%$).

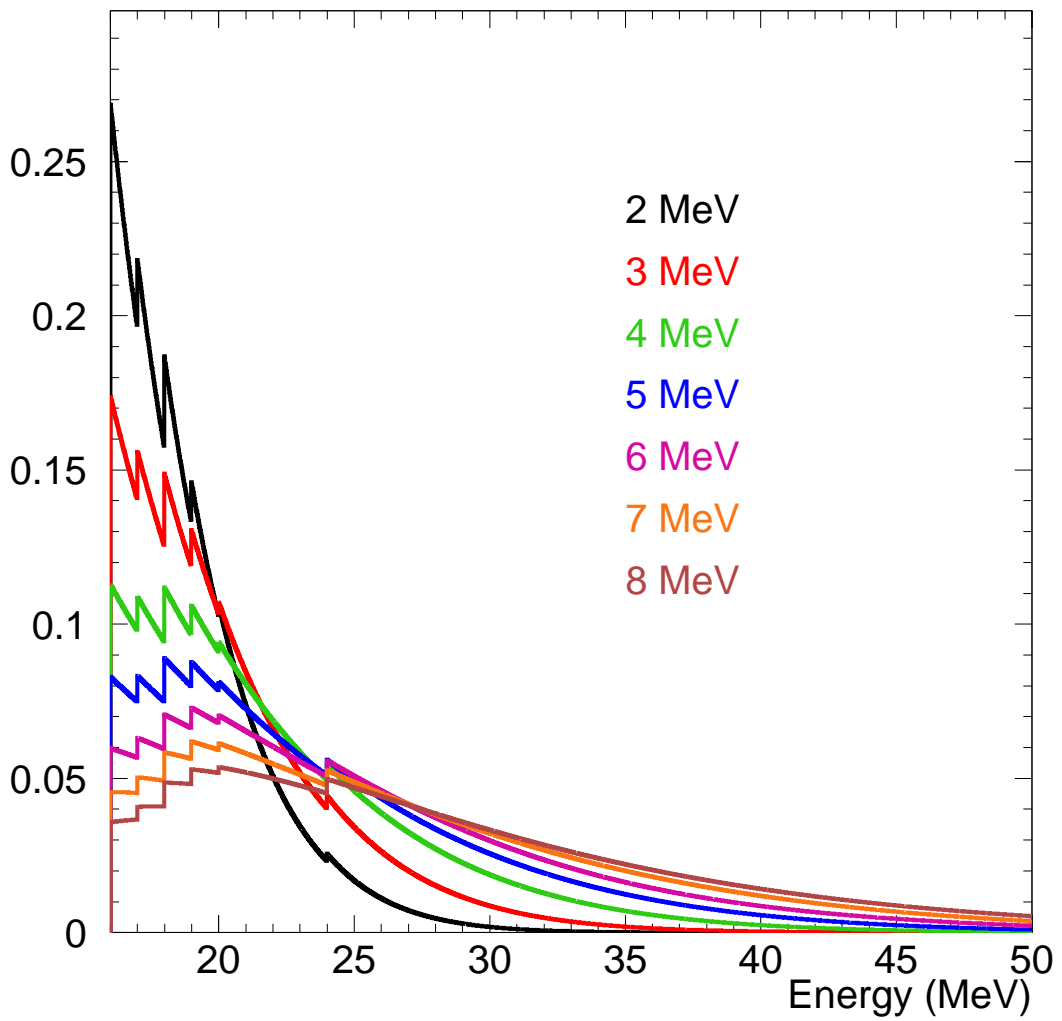


Figure B.24: SK-III SRN PDFs for various neutrino temperatures in the signal region. Solar and spallation inefficiencies are applied. The PDF is normalized to 1 between 16 and 90 MeV, minus a tiny amount that falls into the sidebands ($\sim 0.5\%$).

B.2 SK-I remaining background fits

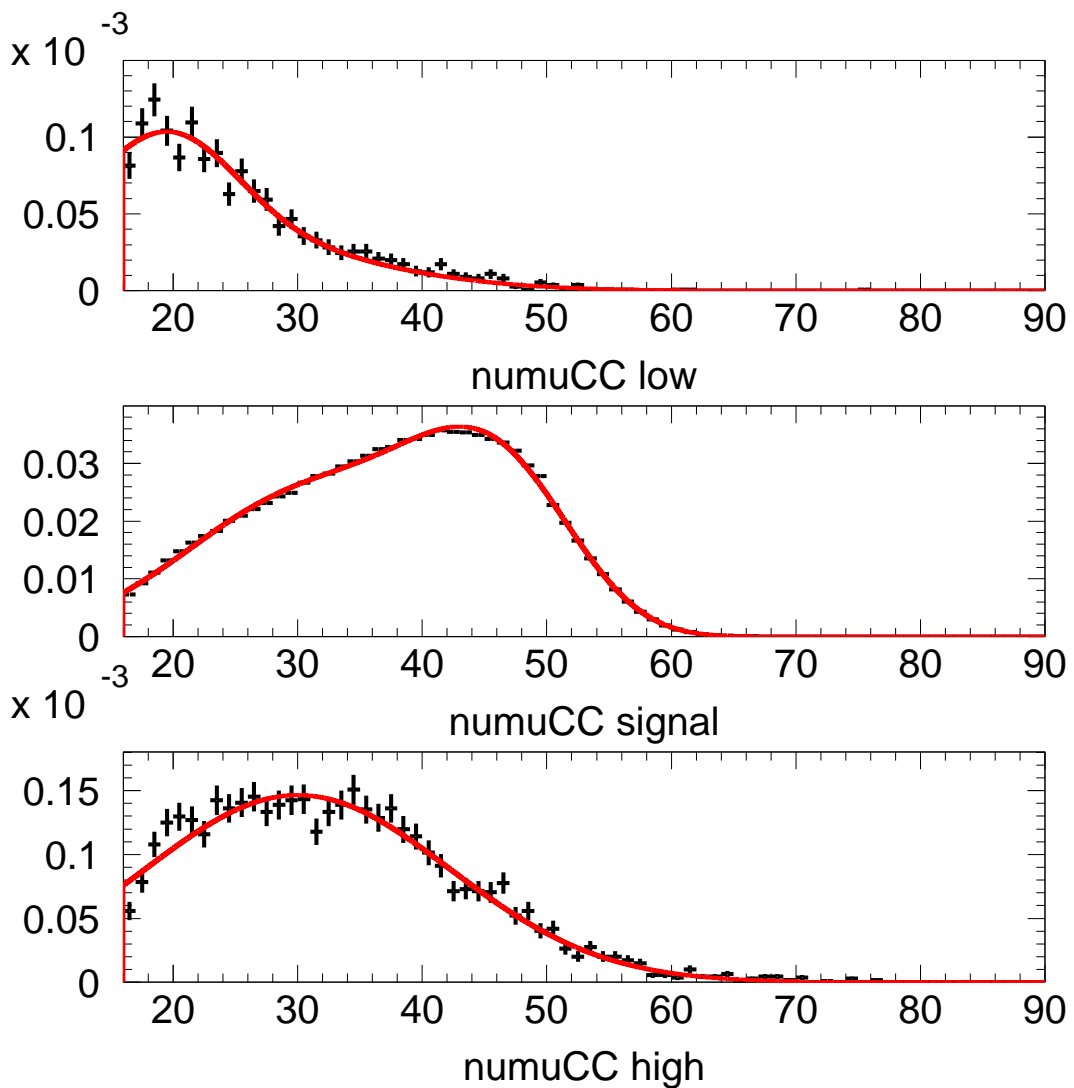


Figure B.25: PDF for ν_μ CC is shown compared to the decay electron data it is fit from for SK-I. Spallation inefficiency is not shown here, and is manually added to the PDFs later. The data is scaled to the PDF, which is normalized to one when integrated over energy for all three Cherenkov angles combined, after spallation cut inefficiency is added.

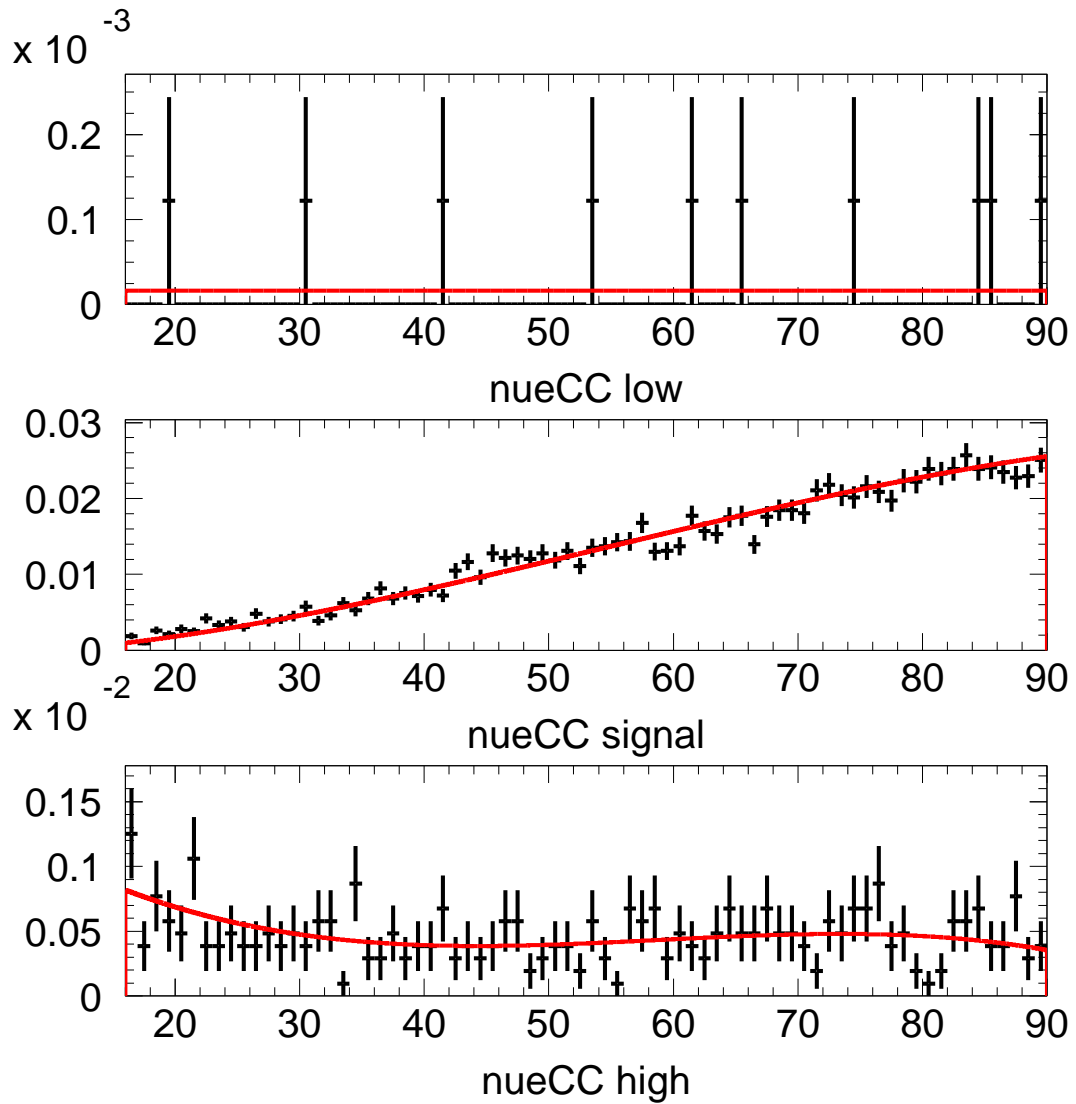


Figure B.26: PDF for ν_e CC is shown compared to the MC it is fit from for SK-I. Spallation and solar cut inefficiencies are not shown here, and are manually added to the PDFs later. The data is scaled to the PDF, which is normalized to one when integrated over energy for all three Cherenkov angles combined, after spallation and solar cut inefficiencies are added.

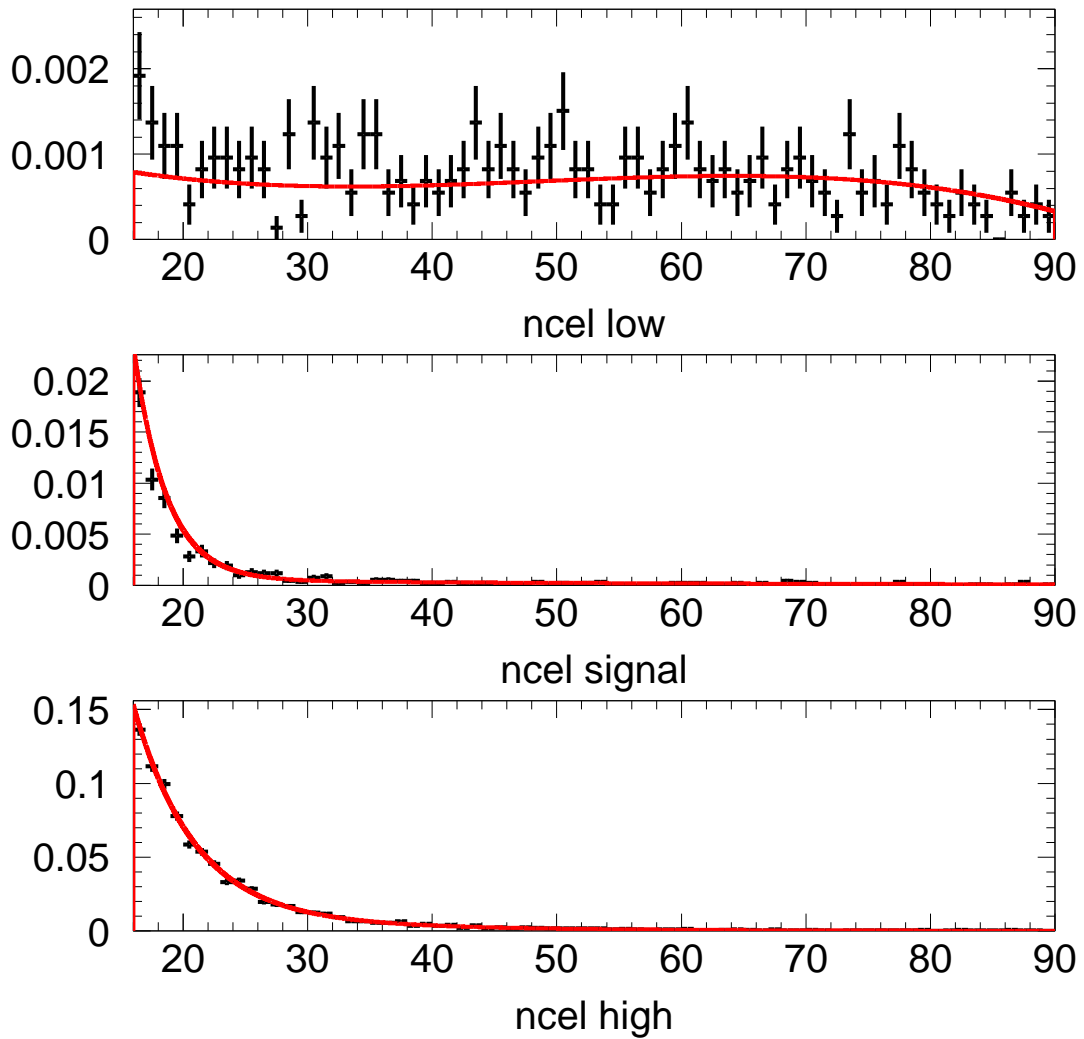


Figure B.27: PDF for NC elastic is shown compared to the MC it is fit from for SK-I. Spallation and solar cut inefficiencies are not shown here, and are manually added to the PDFs later. The data is scaled to the PDF, which is normalized to one when integrated over energy for all three Cherenkov angles combined, after spallation and solar cut inefficiencies are added.

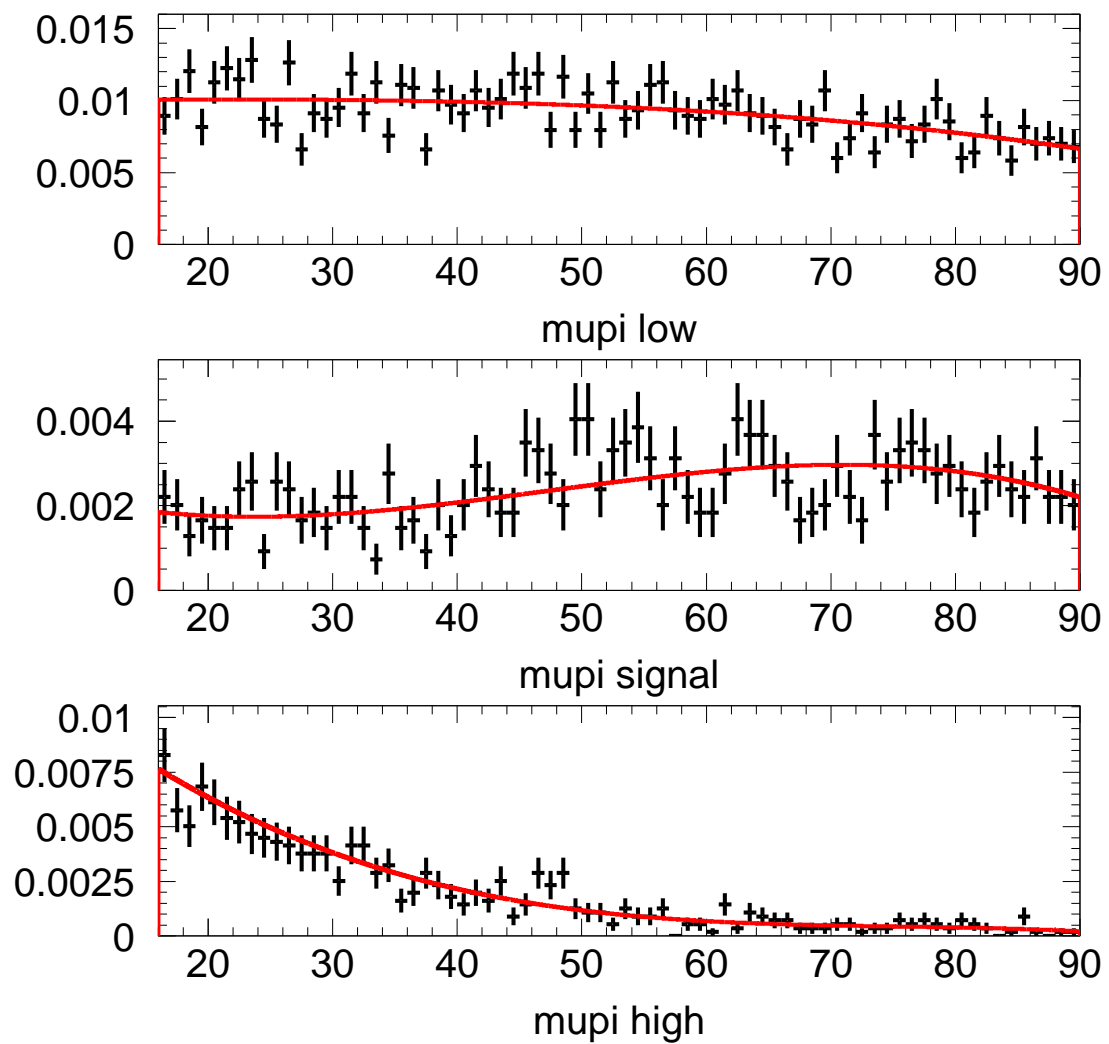


Figure B.28: PDF for μ/π is shown compared to the MC it is fit from for SK-I. Spallation and solar cut inefficiencies are not shown here, and are manually added to the PDFs later. The data is scaled to the PDF, which is normalized to one when integrated over energy for all three Cherenkov angles combined, after spallation and solar cut inefficiencies are added.

B.3 SK-II remaining background fits

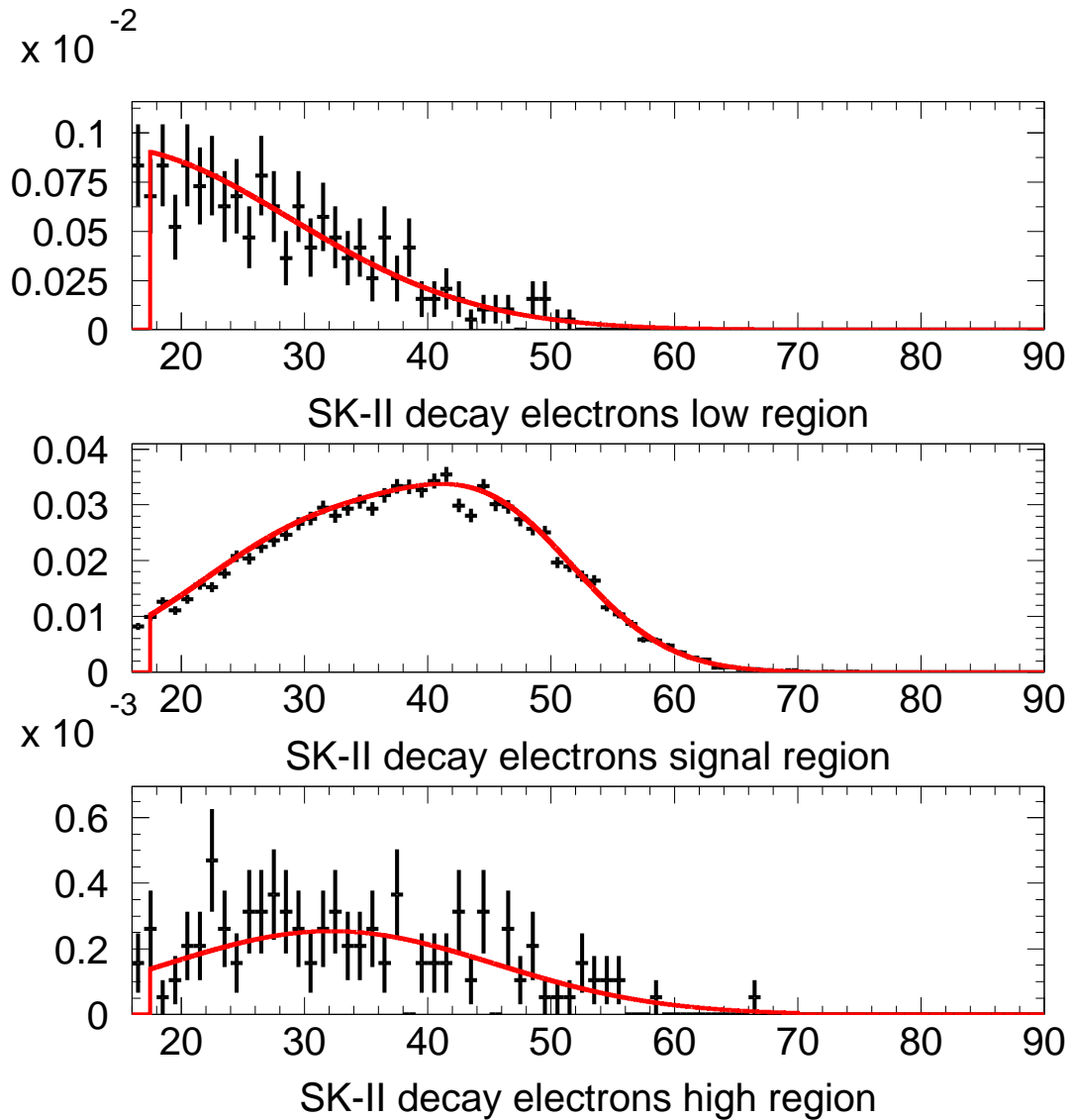


Figure B.29: PDF for ν_μ CC is shown compared to the decay electron data it is fit from for SK-II. Spallation and solar cut inefficiencies are not shown here, and are manually added to the PDFs later. The data is scaled to the PDF, which is normalized to one when integrated over energy for all three Cherenkov angles combined, after spallation and solar cut inefficiencies are added.

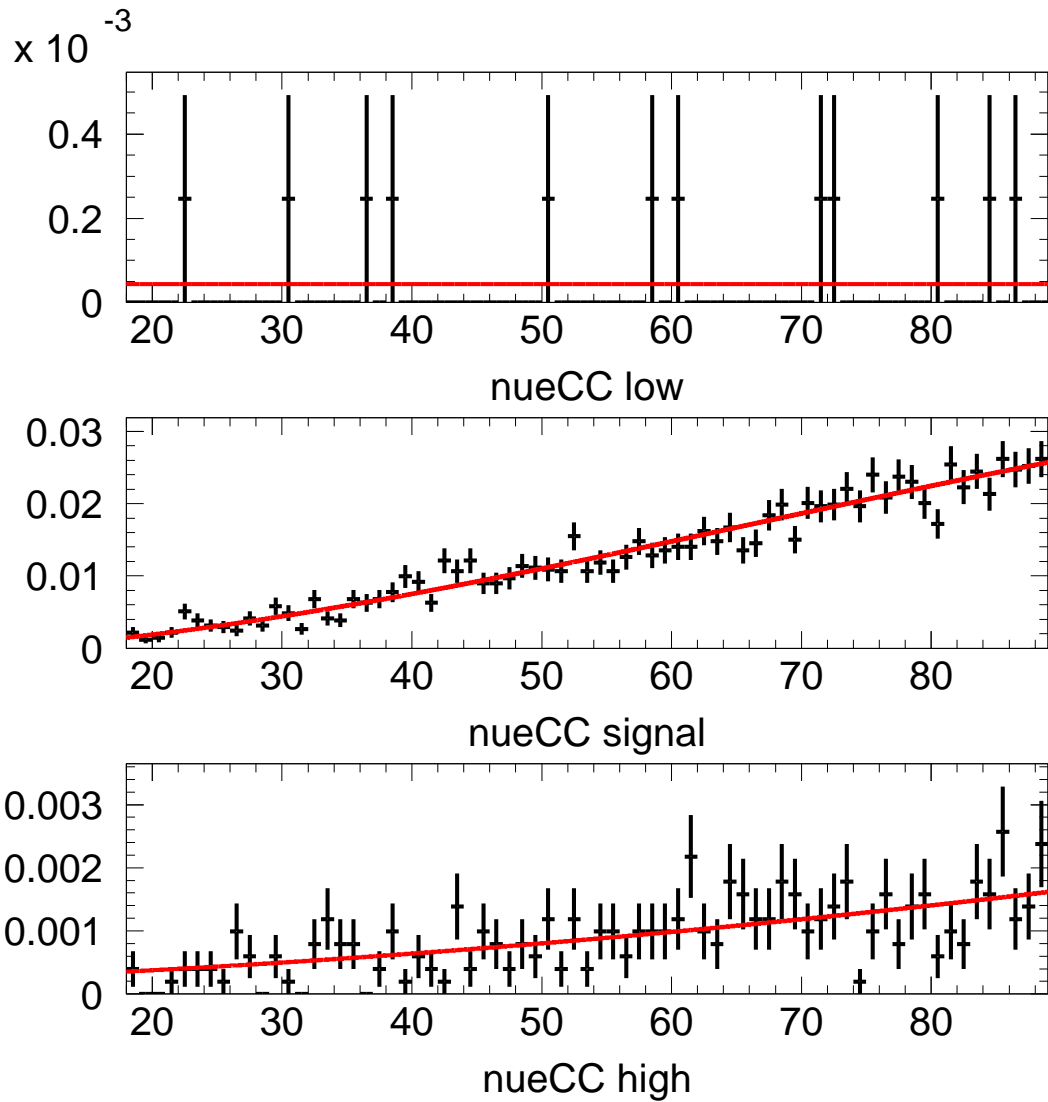


Figure B.30: PDF for ν_e CC is shown compared to the MC it is fit from for SK-II. Spallation and solar cut inefficiencies are not shown here, and are manually added to the PDFs later. The data is scaled to the PDF, which is normalized to one when integrated over energy for all three Cherenkov angles combined, after spallation and solar cut inefficiencies are added.

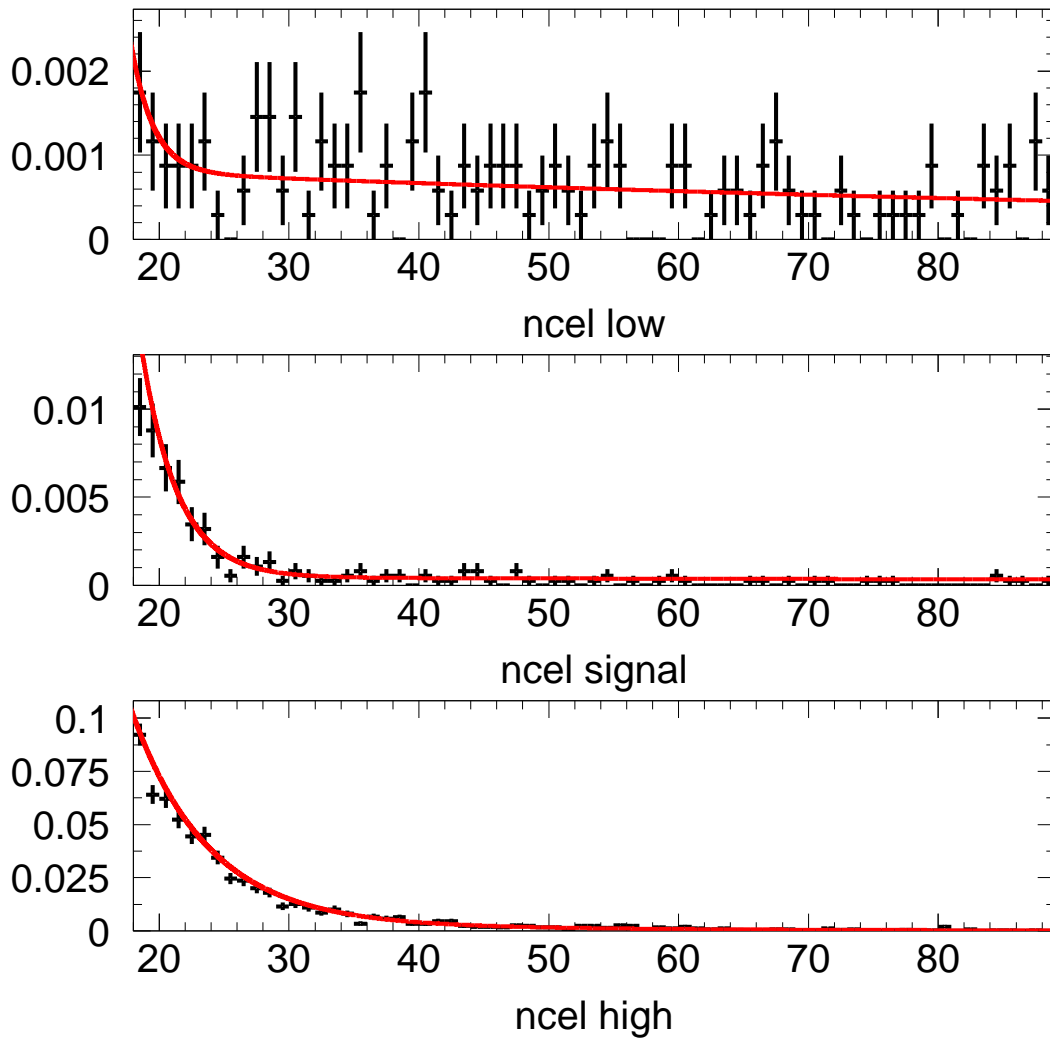


Figure B.31: PDF for NC elastic is shown compared to the MC it is fit from for SK-II. Spallation and solar cut inefficiencies are not shown here, and are manually added to the PDFs later. The data is scaled to the PDF, which is normalized to one when integrated over energy for all three Cherenkov angles combined, after spallation and solar cut inefficiencies are added.

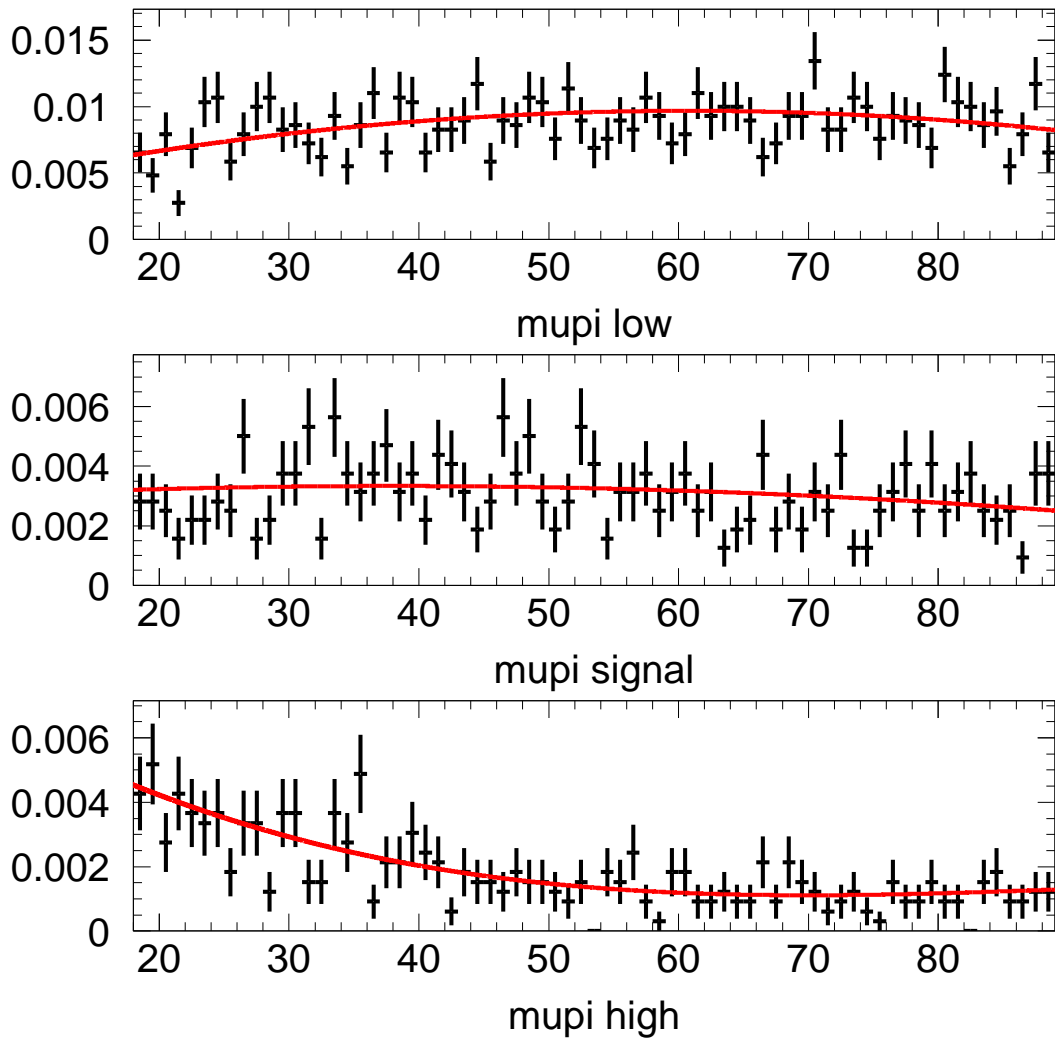


Figure B.32: PDF for μ/π is shown compared to the MC it is fit from for SK-II. Spallation and solar cut inefficiencies are not shown here, and are manually added to the PDFs later. The data is scaled to the PDF, which is normalized to one when integrated over energy for all three Cherenkov angles combined, after spallation and solar cut inefficiencies are added.

B.4 SK-III remaining background fits

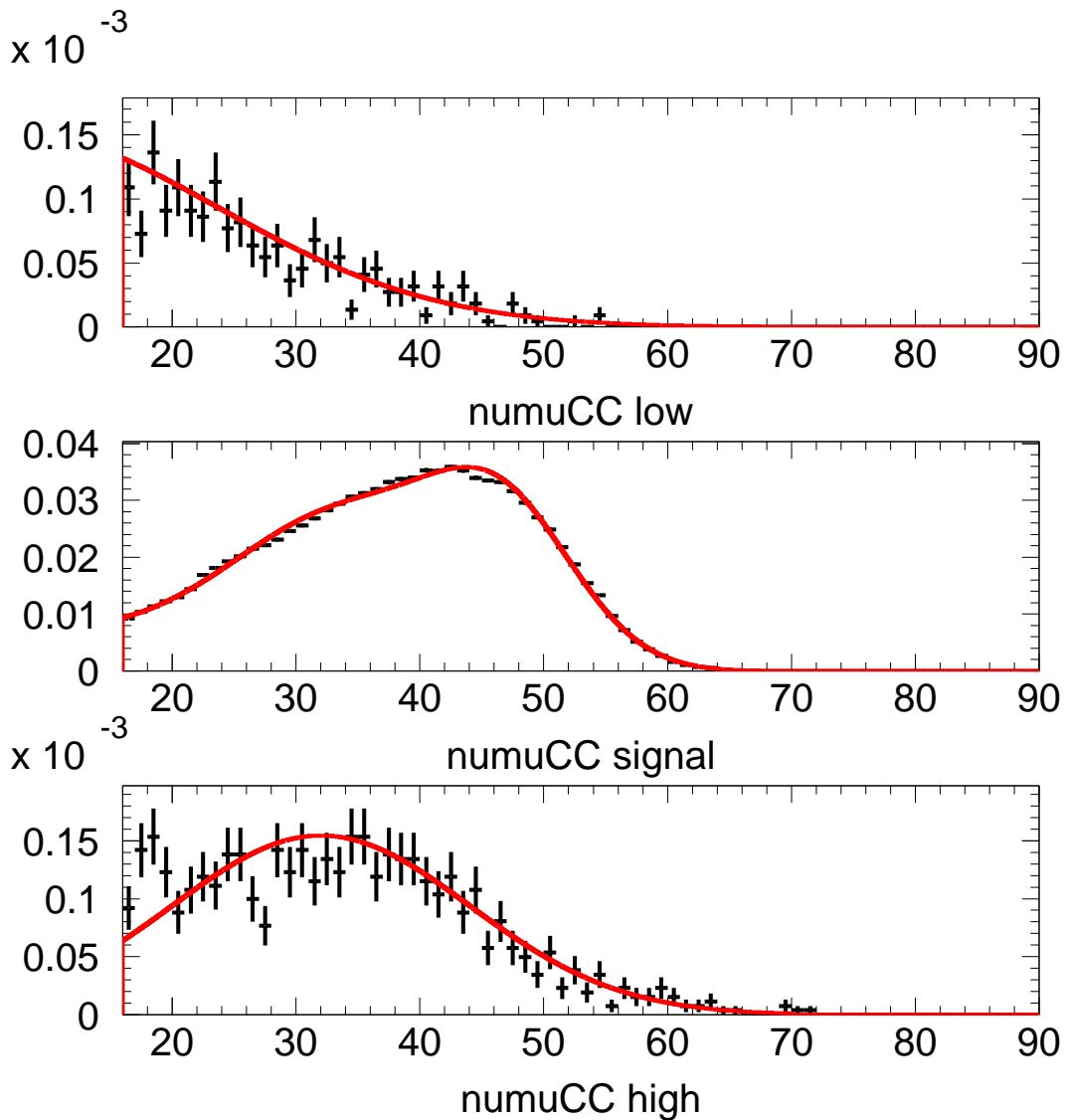


Figure B.33: PDF for ν_μ CC is shown compared to the decay electron data it is fit from for SK-III. Spallation and solar cut inefficiencies are not shown here, and are manually added to the PDFs later. The data is scaled to the PDF, which is normalized to one when integrated over energy for all three Cherenkov angles combined, after spallation and solar cut inefficiencies are added.

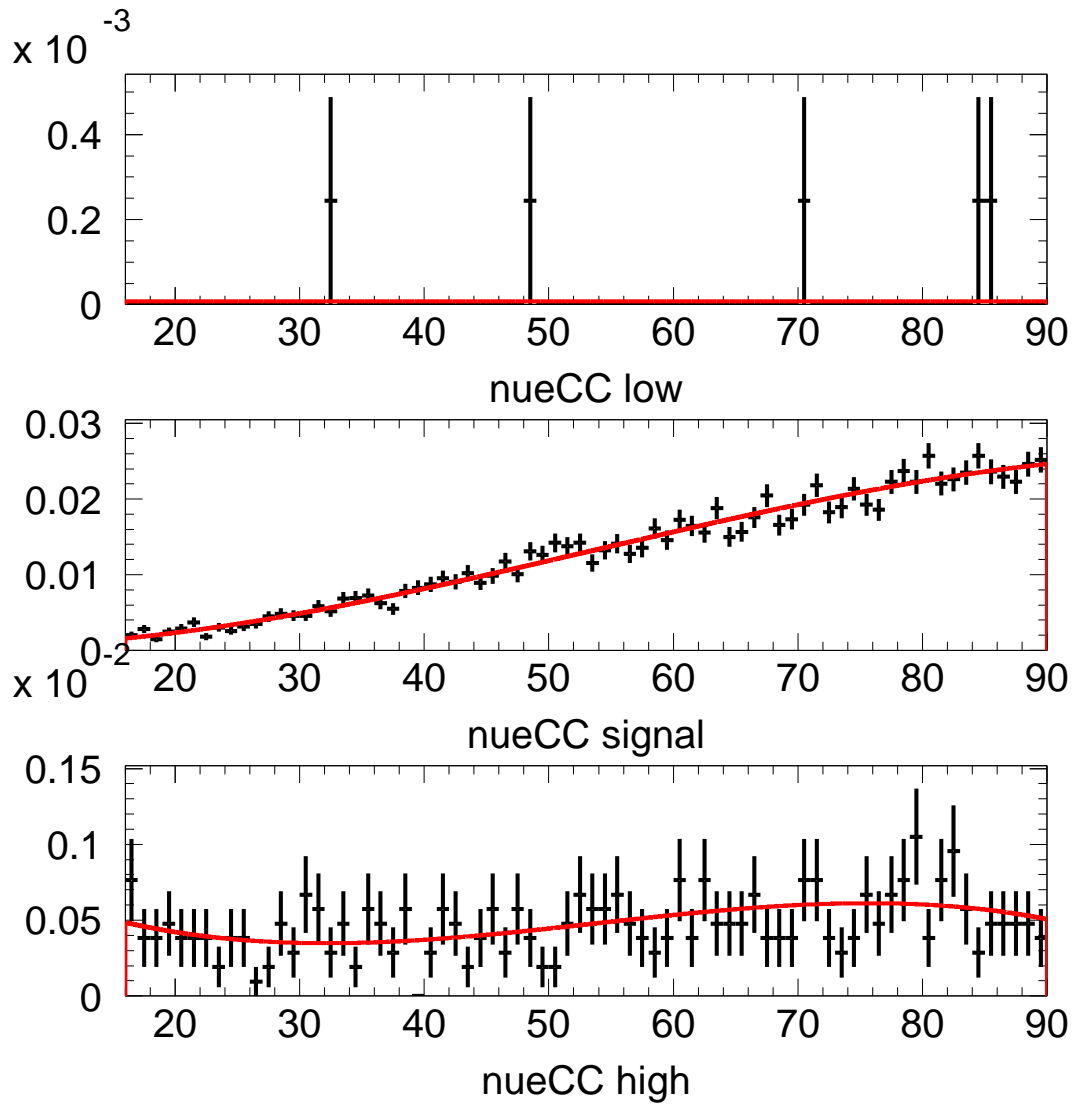


Figure B.34: PDF for ν_e CC is shown compared to the MC it is fit from for SK-III. Spallation and solar cut inefficiencies are not shown here, and are manually added to the PDFs later. The data is scaled to the PDF, which is normalized to one when integrated over energy for all three Cherenkov angles combined, after spallation and solar cut inefficiencies are added.

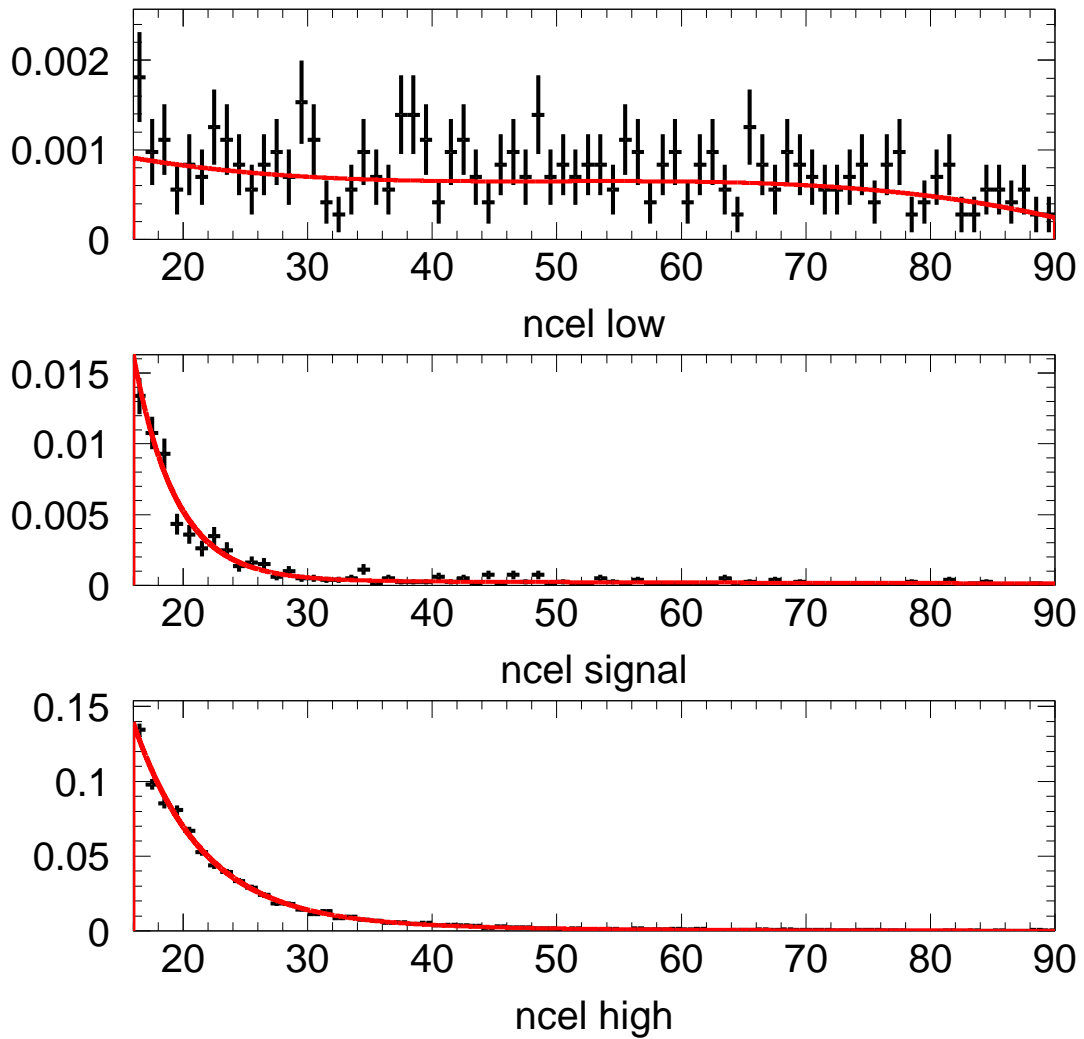


Figure B.35: PDF for NC elastic is shown compared to the MC it is fit from for SK-III. Spallation and solar cut inefficiencies are not shown here, and are manually added to the PDFs later. The data is scaled to the PDF, which is normalized to one when integrated over energy for all three Cherenkov angles combined, after spallation and solar cut inefficiencies are added.

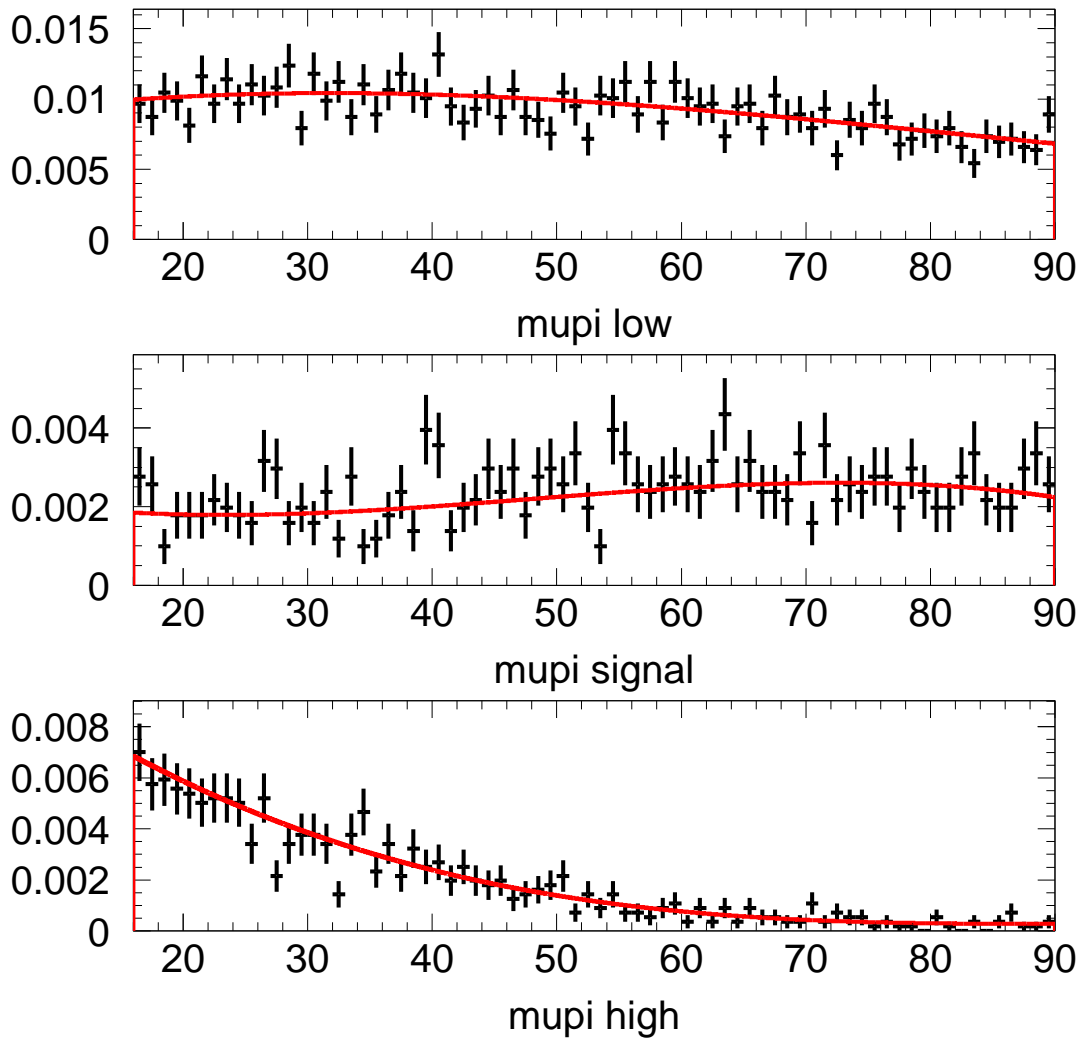


Figure B.36: PDF for μ/π is shown compared to the MC it is fit from for SK-III. Spallation and solar cut inefficiencies are not shown here, and are manually added to the PDFs later. The data is scaled to the PDF, which is normalized to one when integrated over energy for all three Cherenkov angles combined, after spallation and solar cut inefficiencies are added.

C Appendix C - NC

In order to study and understand the remaining atmospheric neutrino backgrounds in the final sample, SK MC was used. 500 years of MC was generated for each SK experiment phase (SK-I, SK-II, SK-III). As described in Chapter 5, the MC is based on GEANT 3 and NEUT. Unfortunately, extensive verification of the MC < 100 MeV, especially for the NC modes, had not been previously done, and a few things were found to be outdated or in error.

The MC allows each event to be tracked according to NEUT mode, which records the underlying physics. Also, each particle and momentum created by NEUT is recorded and tracked.

Two main errors were found in the NC particle production. First involved the production of 15.1 MeV gamma rays during nuclear de-excitation (of a residual ^{15}N or ^{15}O remaining after an atmospheric ν interaction in the oxygen nucleus). The branching ratio for this mode in NEUT was set to 1.3%; however it should be less than 0.007% ([55]). This caused immensely many more de-excitation gammas to occur than should have. A 15.1 MeV gamma can cause an event that reconstructs above 16 MeV (due to energy resolution) and enters our final sample at the most important low energy region. Thus, all 15.1 MeV gamma events were removed from the MC sample.

The second error discovered involved events due to pion absorption in the oxygen, leading to an excited ^{14}N state, along with two protons (from a π^+) or two neutrons (π^-). The excited ^{14}N will release de-excitation gammas. In the NEUT code, the energy of de-excitation photons was randomly generated from 5-20 MeV. However, in truth, the creation of photons of greater than 7.6 MeV is highly suppressed. The result of a SK investigation was that the chance of any pion absorption events making it into our final sample was very small, and that the events we found in our MC should not be there. Thus, they were removed as well.

The spectrum of all NC events in 500 years of SK-I MC is shown in Fig. C.37, along with the spectra of the 15.1 MeV gamma events and the pion absorption events. From this point forwards, all discussion of the NC will have these erroneously created events removed.

The NC events that remain after removing the incorrect events (1725 events in 500 years MC) can be further subdivided into the following categories:

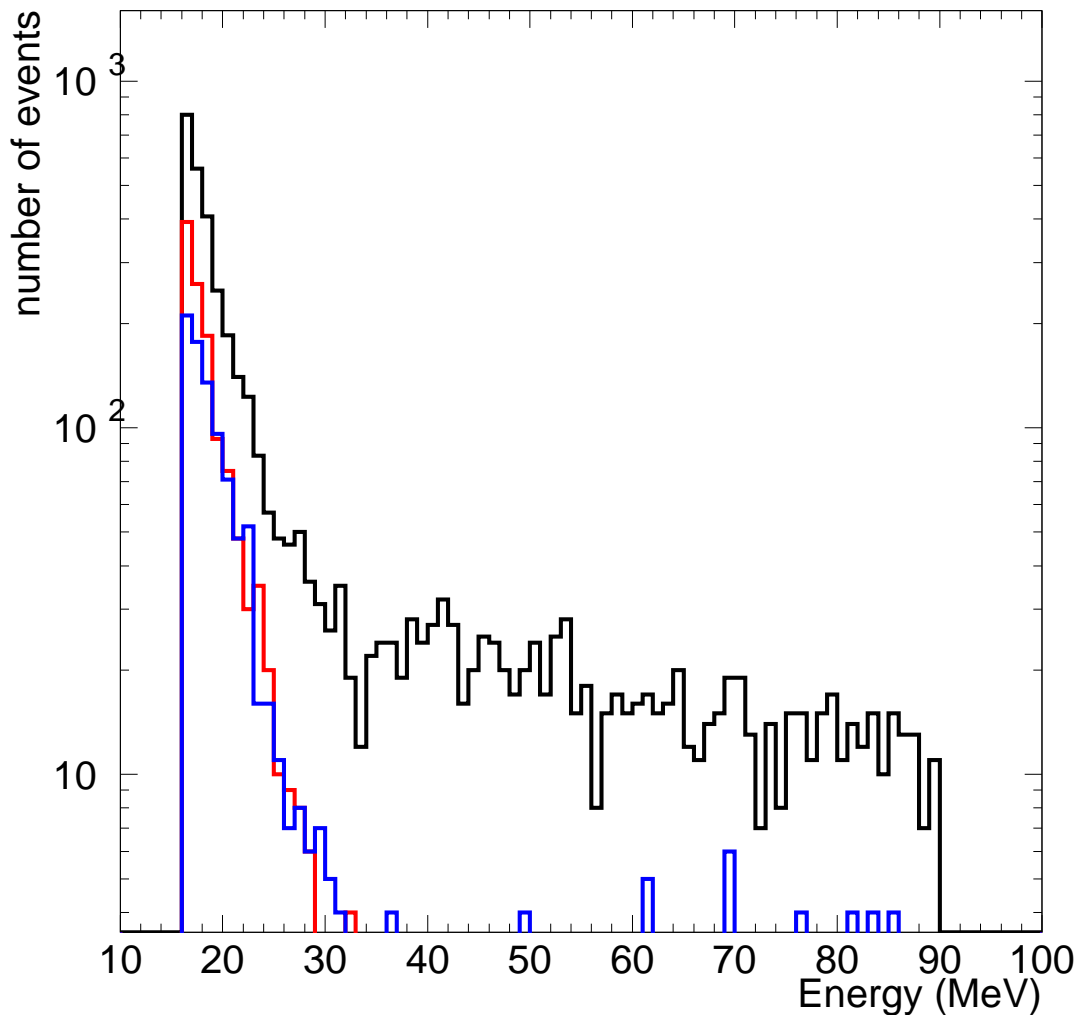


Figure C.37: Spectrum of NC events for 500 years SK-I MC. Shown is all NC (black); 15.1 MeV gamma events (red); and pion absorption events (blue).

- 1) single pion events (969)
- 2) NC elastic scattering (on nucleon) (647 events)
- 3) multiple pion production (85 events)
- 4) single η production (15 events)
- 5) deep inelastic scattering (9 events)

Modes 4) and 5) are so rare as to be negligible. Fig. C.38 shows the spectrum of all the events left after removing 15.1 MeV gamma events and pion absorption events, as well as the spectra of the first three backgrounds.

The multiple pion production mode is not only of very little importance (a factor of 10 smaller than the NC elastic mode) but has a similar spectrum to the NC elastic, meaning any of this signal will be absorbed into the NC elastic mode during the fit to the final data, which allows each background a free-floating normalization.

The single pion channel can be further subdivided (Fig. C.39):

- 1) events resulting in a π^- (such as $\nu + n \rightarrow \nu + p + \pi^-$) or a π^+ (such as $\nu + p \rightarrow \nu + n + \pi^+$), but only if the π^+ is > 200 MeV.
- 2) $\pi^+ < 200$ MeV events. These are singled out as they basically follow a Michel spectrum, which is different than other single pion events.
- 3) π^0 events
- 4) $\nu + O(16) \rightarrow \nu + O(16) + \pi^0$

From the spectra, it can be seen that the last mode is tiny and can be neglected. Furthermore, the second mode mostly follows the Michel spectrum, and is highly similar to the spectrum of decay electrons from sub-Cherenkov muons. This once again means it will be accounted for by that channel in the free floating fit, and can be ignored. It can also be shown that the third mode (π^0 events) can be well described by a linear combination of the four backgrounds we use; this means it will not uniquely contribute to the free floating fit and is safe to ignore.

Clearly the largest and most important background is due to the first channel.

After all considerations, this leaves the first of the single pion channels and the NC elastic channels as the ones necessary to model and consider for the analysis. The single pion channel considered is combined with remnant events from low energy muons from muon neutrino interactions that slip into the final sample, as described in chapter 5.2.

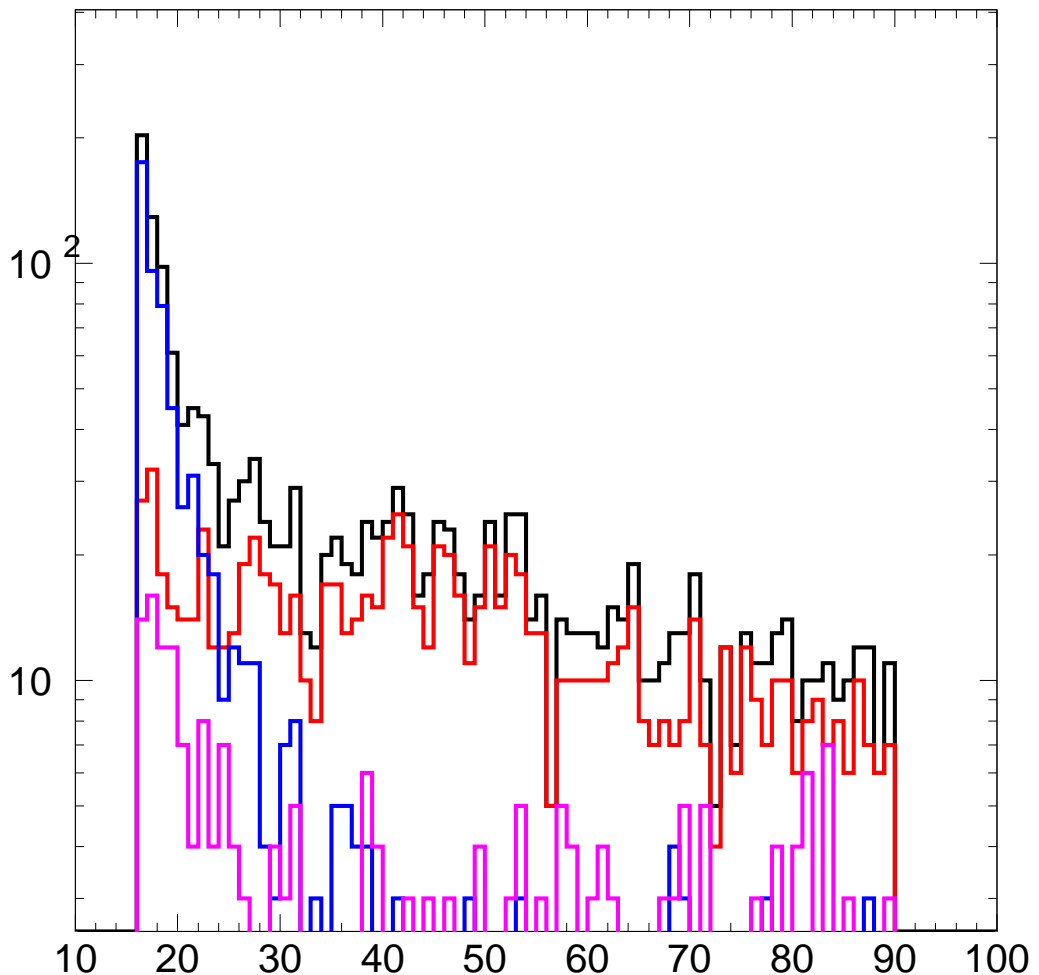


Figure C.38: Spectrum of NC events for 500 years SK-I MC, with 15.1 MeV gammas and pion absorption events removed. Shown is all NC (black); single pion events (red); NC elastic (blue); and multiple pion production (purple).

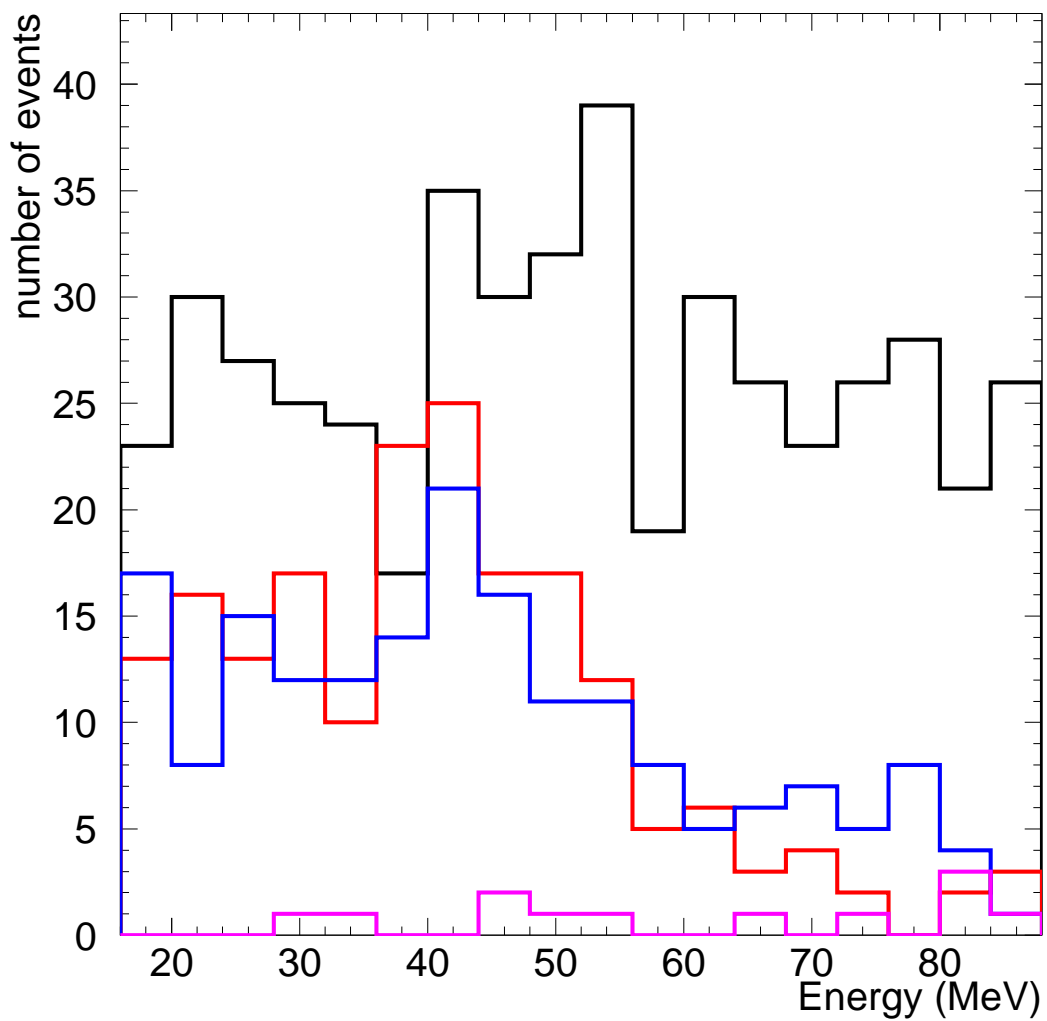


Figure C.39: Spectrum of single pion NC events for 500 years SK-I MC, with 15.1 MeV gammas and pion absorption events removed. Shown is single π^- events of all energies and events with π^+ 's > 200 MeV (black); single π^+ 's < 200 MeV (red); π^0 events (blue); and events from a more complicated interaction with oxygen (purple).

D Appendix D - Expanded fit results

Table D.2: Complete raw fit results for SK-I. Best fits for all five channels given in number of events seen in final sample, in all three Cherenkov regions combined. The signal efficiency for each model is given (as evaluated in the signal region, as the amount of SRN signal in the sidebands is negligible). As the SK-I best fit is less than 0 SRN events, the backgrounds are the same for all models. In the final sample, there were 245 events in the signal region, 47 events in the low angle region, and 51 events in the high angle region. The SK-I livetime is 1497 days.

Model	SRN	90% CL ($\text{ev, cm}^{-2}\text{s}^{-1}$)	ν_μ CC	ν_e CC	NC	μ/π	ϵ
LMA	0	<15, <2.5	146.6	86.8	47.0	62.6	0.798
Gas Infall	0	<12.6, <2.3	146.6	86.8	47.0	62.6	0.791
Heavy Metal	0	<13.4, <2.3	146.6	86.8	47.0	62.6	0.791
Failed SN	0	<16.2, <2.5	146.6	86.8	47.0	62.6	8.0
Chemical	0	<13.8, <2.4	146.6	86.8	47.0	62.6	0.788
6 MeV	0	<15.5, <2.6	146.6	86.8	47.0	62.6	0.797

Table D.3: Complete raw best fit results for SK-II. Best fits for all five channels given in number of events seen in final sample, in all three Cherenkov regions combined. The signal efficiency for each model is given (as evaluated in the signal region, as the amount of SRN signal in the sidebands is negligible). In the SK-II final data sample, there were 129 events in the signal region, 29 in the low angle region, and 26 events in the high angle region. The SK-II livetime is 794 days.

Model	SRN	90% CL ($\text{ev, cm}^{-2}\text{s}^{-1}$)	ν_μ CC	ν_e CC	NC	μ/π	ϵ
LMA	4.7	<17.6, <7.7	72.4	44.9	19.9	42.1	0.567
Gas Infall	4.4	<14.7, <7.5	72.7	45.0	19.7	42.1	0.533
Heavy Metal	4.5	<15.4, <7.3	72.6	45.0	19.7	42.1	0.545
Failed SN	5.3	<19.6, <8.0	71.8	44.9	19.9	42.1	0.585
Chemical	4.4	<15.7, <7.2	72.6	45.0	19.8	42.1	0.552
6 MeV	4.3	<18.1, <7.0	72.7	44.9	20.0	42.1	0.635

Table D.4: Complete raw best fit results for SK-III. Best fits for all five channels given in number of events seen in final sample, in all three Cherenkov regions combined. The signal efficiency for each model is given (as evaluated in the signal region, as the amount of SRN signal in the sidebands is negligible). In the SK-III final data sample, there were 105 events in the signal region, 17 in the low angle region, and 15 events in the high angle region. The SK-III livetime is 562 days.

Model	SRN	90% CL (ev, $cm^{-2}s^{-1}$)	ν_μ CC	ν_e CC	NC	μ/π	ϵ
LMA	8.3 $^{+6.6}_{-5.5}$	<18, <8.1	48.6	44.9	10.8	24.4	0.780
Gas Infall	7.4 $^{+5.7}_{-4.8}$	<15.9, <7.9	49.5	45.0	10.7	24.4	0.766
Heavy Metal	7.7 $^{+5.9}_{-5.0}$	<16.5, <7.8	49.2	44.9	10.7	24.5	0.774
Failed SN	9.1 $^{+7.3}_{-6.2}$	<19.9, <8.5	47.8	44.9	10.8	24.4	0.783
Chemical	7.9 $^{+6.1}_{-5.2}$	<17, <7.9	48.9	45.0	10.8	24.4	0.776
6 MeV	8.2 $^{+6.5}_{-5.6}$	<17.9, <8.2	48.6	45.0	10.8	24.4	0.771